TECHNISCHE
UNIVERSITÄT
DARMSTADT

Physik

Fully Exclusive Measurements of Quasi-Free Single-Nucleon Knockout Reactions in Inverse Kinematics

Vom Fachbereich Physik
der Technischen Universität Darmstadt
zur Erlangung des Grades
eines Doktors der Naturwissenschaften
(Dr. rer. nat.)

genehmigte Dissertation von

Dipl.-Phys. Valerii Panin
aus Alchevsk (Ukraine)

Darmstadt 2012

D17

Referent: Prof. Dr. Thomas Aumann
Korreferent: Prof. Dr. Joachim Enders

Tag der Einreichung: 15.05.2012
Tag der mündlichen Prüfung: 06.06.2012

Abstract

This thesis will present a novel experimental method for investigating proton-induced single-nucleon knockout reactions at relativistic energies. For the first time this type of reactions is studied in complete and inverse kinematics, using a ^{12}C beam at an energy of 400 MeV/u impinged on a plastic CH_2 target, where the reactions on hydrogen take place. It is shown that the reaction mechanism is dominated by quasi-free proton-nucleon scattering process of a type $(p, 2p)$ or (p, pn) within the nucleus, that is reflected in a strong spatial correlation between the two outgoing nucleons. The reactions are foreseen as an ideal way to explore single-particle and cluster structure of nuclei and will become an important part of the physics program at the future R^{3}B (Reactions with Relativistic Radioactive Beams) experiment at FAIR, which will be based on kinematically complete measurements of the reactions with neutron-proton asymmetric nuclei. The benchmark experiment, which is discussed in this work, was performed at a prototype LAND-R^{3}B setup at GSI, Germany. The total cross section of 30.5±2.3 mb has been measured for the ^{12}C$(p, 2p)^{11}$B reaction in inverse kinematics, and the cross section of 18.1±2 mb has been extracted for the removal of a proton from the p-shell in ^{12}C. Employing the in-flight γ-ray spectroscopy, the following exclusive $(p, 2p)$ cross sections are determined for individual low-lying p-hole states in the residual ^{11}B nucleus: 12.7±1.5 mb for the ground state, 3.1±0.4 mb for the first excited state 2.125 MeV $(1/2^-)$ and 2.2±0.3 mb for the excited state 5.02 MeV $(3/2^-)$. The excitation energy of deep-hole particle-unstable states is reconstructed via invariant-mass measurements of mainly two-body decays of the ^{11}B residue. A broad peak at around 15 MeV in the excitation spectrum of ^{11}B is observed and interpreted as a proton knockout from strongly bound s-shell in ^{12}C. The internal momentum distribution of protons, which are removed from the p-shell in ^{12}C, is measured redundantly using two methods: the detection of residual ^{11}B fragments and the angular and energy measurements of scattered proton pairs. The momentum width of 105 MeV/c is extracted using both methods. A similar value of 106 MeV/c is obtained for the internal momentum width of p-state neutrons probed through the ^{12}C$(p, pn)^{11}$C reaction. The momentum width of 132 MeV/c is determined for deeply bound s-shell protons via the measurements of scattered protons. Detailed simulations of the experimental response have been developed as a part of the analysis.

Zusammenfassung

Die vorliegende Arbeit präsentiert eine neue experimentelle Methode zur Untersuchung von Proton-induzierten Ein-Nukleon-Knockout-Reaktionen bei relativistischen Energien. Diese Art von Reaktionen wurde zum ersten Mal in vollständiger und inverser Kinematik untersucht. Ein ^{12}C-Strahl mit einer Energie von 400 MeV/u wurde auf ein CH_2 Target gelenkt, in welchem die ^{12}C Ionen mit dem Wasserstoff reagieren. Es wird gezeigt, dass der Reaktionsmechanismus durch quasi-freie Proton-Nukleon-Streuung des Typs $(p, 2p)$ oder (p, pn) innerhalb des Kerns dominiert wird. Dieses spiegelt sich in einer starken räumlichen Korrelation zwischen den beiden Nukleonen im Ausgangskanal wieder. Diese Reaktionen werden als idealer Weg angesehen um Ein-Teilchen- und Cluster-Strukturen von Kernen zu untersuchen. Sie werden ein wichtiger Teil des Physik-Programms des R^{3}B (Reactions with Relativistic Radioactive Beams) Experimentes an FAIR sein, welches kinematisch vollständige Messungen mit Neutron-Proton-asymmetrischen Kernen ermöglichen wird. Das in dieser Arbeit vorgetellte Benchmark-Experiment wurde an einem Prototyp LAND-R^{3}B-Setup an der GSI (Deutschland) durchgeführt. Ein Gesamt-Wirkungsquerschnitt von 30.5±2.3 mb wurde für die ^{12}C$(p, 2p)^{11}$B Reaktion in inverser Kinematik bestimmt. Außerdem wurde ein Wirkungsquerschnitt von 18.1±2 mb für das Entfernen eines Protons aus der p-Schale in ^{12}C gemessen. Unter zuhilfenahme der 'In-Flight-γ-Spektroscopy' wurden folgende exklusive $(p, 2p)$-Wirkungsquerschnitte für einzelne niedrig liegende p-Loch-Zustände ermittelt: 12.7±1.5 mb für den Grundzustand von ^{11}B, 3.1±0.4 mb für den ersten angeregten Zustand 2.125 MeV $(1/2^-)$ und 2.2±0.3 mb für den angeregten Zustand 5.02 MeV $(3/2^-)$. Die Anregungsenergie von tiefen Loch-Zuständen (Teilchen-instabil) wurde über die gemessene invariante Masse rekonstruiert. Hierbei wurden hauptsächlich Zwei-Körper-Zerfälle der ^{11}B-Fragmente betrachtet. Ein breiter Peak bei etwa 15 MeV wurde im Anregungsspektrum von ^{11}B bestimmt, dieser wird als Ein-Protonen-Knockout aus dem stark gebundenen $l = 0$ Orbital in ^{12}C interpretiert. Die internen Impulsverteilungen von Protonen welche aus der p-Schale in ^{12}C entfernt werden, werden durch zwei Verfahren redundant gemessen: Erstens durch Erfassen der übrigbleibenden Fragmente (^{11}B) und zweitens durch Messung der Winkel und der Energie der gestreuten Protonen-Paare. Mit beiden Methoden wurde eine Impulsbreite von 105 MeV/c für Protonen im p-Zustand extrahiert. Ein sehr ähnlicher Wert von 106 MeV/c wurde für die Impulsbreite von Neutronen im p-Zustand via (p, pn)-Reaktionen erhalten. Über die Messung der gestreuten Protonen wurde eine Impulsbreite von 132 MeV/c für tief gebundene s-Schalen-Protonen extrahiert. Detaillierte Simulationen der experimentellen Antwortfunktion wurden als ein Teil der Analyse entwickelt.

Contents

Chapter 1

Introduction

For many decades quasi-free scattering (QFS) reactions with protons have been used as a powerful experimental tool to study single-particle properties in nuclei. Already in the pioneering experiments performed by Chamberlain & Serge [1] and Cladis, Hess & Moyer [2] the existence of such processes was demonstrated through observations of strongly correlated proton pairs emerging in the reactions of a type ${}^{A}Z(p,2p)^{A-1}(Z-1)$. This can be understood as a direct knockout of a proton from the nucleus ${}^{A}Z$ induced by an incident high-energy proton. The interpretation of the direct proton-proton scattering mechanism inside the nucleus was justified in many later experiments [3, 4, 5, 6]. Due to the choice of high incident energies (between 100 and 1000 MeV), the mean free path of a proton inside the nucleus becomes comparable with the nuclear radius and the interaction is strongly localized, since the de Broglie wavelength of the projectile is smaller than the average internucleon distance in the nucleus. In this energy regime one can neglect the influence of the spectator nucleons that makes the reaction mechanism relatively simple, and to a good approximation the process can be considered as quasi-free. The kinematical properties of the two scattered protons and of the residual ${}^{A-1}(Z-1)$ fragment carry valuable spectroscopic information about particular quantum state of the struck proton such as, for instance, its internal momentum and separation energy.

Similar knockout reactions can be observed in electron scattering experiments at high energies [7, 8]. In spite of usually higher accuracy of such measurements due to less distortion effects for electrons in the nuclear medium, there are also some disadvantages, namely the smallness of the electromagnetic cross section and an exceptional selectivity for the reactions with protons. This is unwanted feature when one intends to study single-particle states of neutrons, which are of a great interest in particular for investigation of the nuclear structure in exotic nuclei with a large neutron-proton asymmetry. In contrast to this, hadronic quasi-free scattering of a type (p,pn) is proven to be suitable for such purposes [9].

The nucleon-nucleon interactions in nuclei are amongst the most interesting and less investigated topics in Nuclear Physics [10, 11]. Modifications of nucleon and meson masses and sizes inside the nuclear medium have been speculated by many authors as well as the density dependence of the nucleon-nucleon interaction [12, 13]. The corresponding theoretical models include deconfinement of quarks, renormalization effects due to strong relativistic nuclear fields, and chiral symmetry restoration. The modifications of in-medium nucleon properties are reflected in the spin and isospin observables of QFS reactions with polarized proton beams, which have been extensively investigated by Noro *et al.* [14].

Correlations between nucleons inside nuclei is another interesting and poorly investigated

phenomenon, which can be probed via the QFS reactions. It has been recently studied in the Jefferson Lab experiment [15] with electron-induced proton-knockout reactions at the missing momentum value greater than the Fermi momentum $p_f \approx 275$ MeV/c. The reaction $^{12}\mathrm{C}(e, e'p)$ was measured in coincidence with an additionally ejected nucleon, which balanced almost entirely the missing momentum. A large fraction of these events was attributed to the reactions on proton-neutron pairs inside ^{12}C, which have a small center-of-mass momentum and a large relative momentum arising presumably from the short-range component of the nucleon-nucleon potential. A small percentage of the observed proton-proton pairs and, by inference, neutron-neutron pairs was interpreted as a clear fingerprint of the short-range tensor force.

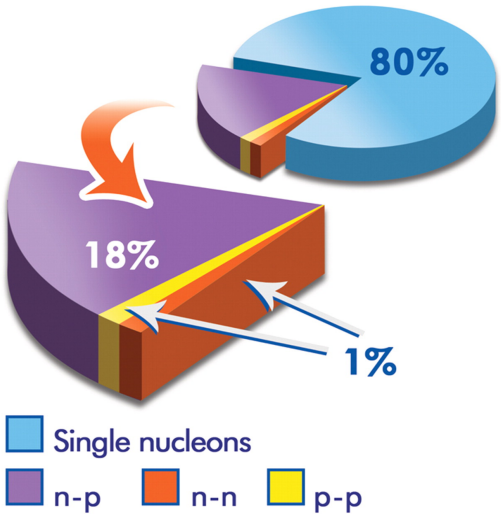

Figure 1.1: An artistic representation of the results obtained from the observations of $^{12}\mathrm{C}(e, e'pp)$ and $^{12}\mathrm{C}(e, e'pn)$ reactions (the picture is taken from [15]). It was concluded that about 20% of all nucleons in the ground state of ^{12}C exist in form of correlated pairs with a large relative momentum, from which 18% have proton-neutron configuration and only 2% are neutron-neutron and proton-proton pairs.

A principal way for isolating two-nucleon short range correlations through $(p, 2p + n)$ reactions has been also demonstrated by several authors [16, 17, 18]. Using proton beams with large momenta (up to 9 GeV/c), a high-momentum proton was knocked out from a nucleus and a directionally correlated high-momentum neutron was observed in triple coincidence with the two emerging protons.

Another in-medium effect, which can be studied through the QFS reactions, is related with the clusterization of the nuclei, *i.e.* aggregation of nucleons into clusters like α-particles. The experiments in which (p, pd) [19, 20] and $(p, p\alpha)$ [21] reactions were observed confirmed the domination of the QFS mechanism in such processes. It was later predicted for the nuclei close to the neutron drip-line that their ground states should possess a distinct cluster structure in response to the strong neutron excess. This effect can be attributed to the tendency to optimize the binding energy, which is best achieved via clusterization of the core in such nuclei.

It is clear that QFS reactions provide an extremely valuable source of information about internal nuclear structure and nuclear properties. However, experiments in which energetic proton beams are used have a limitation to the nuclei lying in the stability region. The

development of new accelerator techniques for the production of radioactive beams of exotic isotopes opens new frontiers for studying the modifications of nuclear properties in nuclei with a strong isospin asymmetry, where QFS reactions might become extremely helpful. In practice, however, it is very difficult to produce a stationary target made out of short-lived unstable isotopes, therefore the experiments in inverse kinematics are needed, *i.e* when the nucleus of interest is the projectile (radioactive beam) colliding with the target-like proton.

The present thesis is dedicated to the experimental study of proton-induced quasi-free scattering reactions measured in inverse and complete kinematics. This is also the first time when fully exclusive measurements of $^{12}\mathrm{C}(p,2p)^{11}\mathrm{B}$ and $^{12}\mathrm{C}(p,pn)^{11}\mathrm{C}$ reactions are attempted. The experiment is motivated by the feasibility study of the presented experimental technique, that will become a basis for the future QFS experiments at the $\mathrm{R^3B}$[1] setup [22] at FAIR [23].

1.1 Elementary Treatment of Quasi-Free Scattering

Generally speaking, there are two main aspects involved in a QFS reaction, which are treated relatively independently:

- The reaction mechanism, implying a specific reaction model and all necessary limitations and corrections of this model, *e.g.* validity of the impulse approximation, distortion effects due to absorption etc.
- The properties of the nuclear system involved into the process before and after the reaction.

The theoretical interpretation of the results obtained in the QFS experiment must consider both aspects. In this section only a qualitative description will be given and more detailed information can be found elsewhere [24, 25, 26].

In contrast to many nuclear reactions at low energies, which are known to proceed via the mechanism of compound intermediate state involving the entire nucleus, in direct QFS reactions the incident particle interacts with a small fraction of the nucleus. The time interval of the reaction must be shorter or comparable to the characteristic nuclear time ($\sim 10^{-22}$ s) in order to reason the applicability of the sudden approximation; in this approximation the nucleons inside the nucleus are assumed to be "frozen" during the reaction. This can serve also as an argument for the eikonal approximation, which treats projectiles' trajectories as well defined straight lines, that drastically simplifies theoretical calculations.

1.1.1 The Reaction Mechanism

Qualitatively the quasi-free scattering reaction of a type (p,pN), where N denotes a nucleon (alternatively a cluster) being knocked-out, can be determined as a direct process, in which an incident proton with energy E_0 and momentum $\vec{k_0}$ is scattered on a bound nucleon as if both particles are free, and the nucleon is subsequently ejected from the nucleus (see figure 1.2). In other words, when the incident proton energy is sufficiently high and no other violent interaction occurs between the spectator nucleons and the incoming and the two outgoing particles, the process is assumed to be "quasi-free".

[1] Reactions with Radioactive Relativistic Beams.

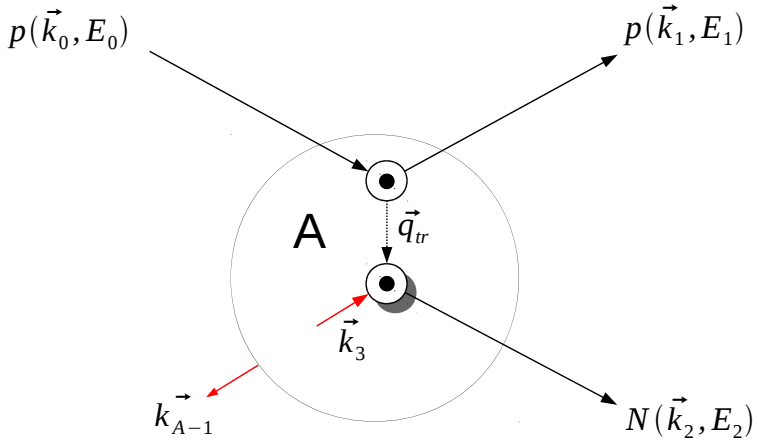

Figure 1.2: Schematic view of the quasi-free scattering reaction (p, pN) in the rest frame of the target nucleus A. The incoming proton knocks out a nucleon N (proton or neutron) from the nucleus, creating a hole in the residual (A-1) nucleus. Red arrows $\vec{k_3}$ and $\vec{k_{A-1}}$ indicate respectively the internal momentum of the knocked-out particle and the balancing recoil momentum of the (A-1) system.

The residual (A-1) nucleus contains a hole in the particular energy level, which was previously occupied by the knocked-out nucleon. If the hole is produced in the level lying below the Fermi surface, the residual nucleus obtains an additional excitation energy E^*_{A-1} corresponding to the energy of this single-particle state relative to the Fermi level. Applying the energy conservation principle, one can find the binding energy B_N of the state assuming the target nucleus to be at rest:

$$B_N = S_N + E^*_{A-1} = T_0 - (T_1 + T_2 + T_{A-1}). \tag{1.1}$$

In this formula $S_N = (M_A - M_{A-1} - m_N)c^2$ is the minimum energy needed to separate the least bound nucleon from the nucleus A, where M_A, M_{A-1} and m_N are the masses of the target, residual nucleus (A-1) and the removed nucleon N, respectively; T denotes kinetic energies of the incoming and the outgoing proton (subscripts 0 and 1), the outgoing nucleon (2) and the final state nucleus (A-1). One can immediately see, that there are two possibilities to determine the energy of the single-particle state. The first way, which is traditionally used in the experiments employing direct QFS kinematics, is based on the measurement of the kinetic energies of the projectile and the outgoing particles. These energies are usually much larger than the one characterizing the single-particle state. This fact imposes certain demands on the measurement precision in the corresponding detection systems. On the other hand, the excitation energy E^*_{A-1} can be used, which is, however, difficult to measure as it requires additional detection systems to be involved. Depending on the magnitude of E^*_{A-1}, the final (A-1) system will decay either via emission of γ-rays if $0 < E^*_{A-1} < S_{A-1}$ (where S_{A-1} is the particle separation threshold in the (A-1) nucleus) or via breakup if $E^*_{A-1} > S_{A-1}$. Unlike the former case, where coincident measurements of the γ-rays can be exploited, measuring the

breakup fragments is rather difficult. In any case, the binding energy spectrum is expected to show peaks at the energies corresponding to various nuclear shells from which the nucleon can be ejected. By the uncertainty principle, the width of such peaks is related to the lifetime of the corresponding hole-states.

Not only the binding energy is an important quantity, characterizing the individual state of a nucleon, but also its internal momentum inside the nucleus ($\vec{k_3}$ in the figure 1.2) which can be associated, for example, with a specific nuclear shell. Applying the momentum conservation law, one can write down:

$$\vec{k_{A-1}} = \vec{k_0} - \vec{k_1} - \vec{k_2} = -\vec{k_3}, \tag{1.2}$$

From Eq. 1.2 one can conclude, that the internal momentum of the nucleon is directly related to the recoil momentum of (A-1) taken with a negative sign. Again, there are two possibilities to determine the internal momentum: by measuring the momenta of all participants in the reaction or by detecting the recoil momentum of the spectator.

This idealized picture of the incoming proton interacting only with one nucleon needs several important modifications to take into account secondary interactions in the incoming and outgoing channels. Nevertheless, this simple model contains the essential physics of the quasi-free knockout, which motivates the use of these reactions for the investigation of the nuclear single-particle structure.

1.2 The Independent-Particle Model

Despite a large progress made in Nuclear Physics during the last century, the satisfactory nuclear theory based on some fundamental principles cannot be built yet. This is due to the fact that the nucleus is a complex quantum system composed of essentially two types of fermions (nucleons), protons and neutrons, the interactions between which are not well understood, and that the nucleons themselves, according to the Standard Model, are composite systems built up from strongly interacting quarks and gluons. The solution of this many-body problem is a challenge for the quantum chromodynamics, a theory of the fundamental strong interaction underlying the nuclear forces.

Many theoretical models have been developed to explain various nuclear properties. However, very often these models are based on conflicting assumptions. For instance, some of them consider the nucleus as a solid body or a liquid drop comprised of strongly interacting particles, while others as a gas of non-interacting particles. In general, nuclear models can be classified into three types regarding the assumed degrees of freedom: the collective models (*e.g.* liquid drop), the models of independent particles (*e.g.* shell model) and unified models connecting the features of the first two. There are also numerous microscopic theories for the nuclei (*e.g.* Hartree-Fock Theory, Relativistic Mean Field Theory *etc.*) which are based on a fundamental NN interaction and can build the properties of the nuclei in a self-consistent way.

The main subject of the present thesis is largely focused on the experimental probe of the single-nucleon properties in the nucleus. This is closely related to the class of models, which suggest predominantly independent motion of protons and neutrons inside some mean-field potential and which turn out to be extremely successful in interpreting a huge body of experimental data as well as in making reliable predictions for new observations.

At a first glance, the concept of the mean-field potential seems to be inapplicable to the system of strongly interacting particles, unlike in the case of the atomic electrons which move in a real central electric field created by the nucleus. However, the nuclear potential comes out to be a reasonable (albeit rather coarse) generalization of the complex forces acting between the nucleons and it can drastically simplify the many-body problem. In the simplest approach, the nuclear system can be described as a two-component Fermi-gas of weakly interacting protons and neutrons confined in a volume with a constant potential V_0 (i.e. in the rectangular potential well). The nucleons occupy all available energy levels up to the maximum Fermi-energy E_f. This naive model is very suitable for qualitative analysis of the nuclear systems. It can be used to obtain, for instance, an analytical density distribution of the single-particle levels in the potential well, as well as to calculate the maximum kinetic energy E_f and the momentum p_f of the nucleons at the Fermi surface [27]:

$$p_f = p_{f,p} = p_{f,n} = \frac{\hbar}{R_0}\left(\frac{9\pi}{8}\right)^{1/3} \approx 250 MeV/c, \tag{1.3}$$

$$E_f = \frac{p_f^2}{2M} \approx 33 MeV, \tag{1.4}$$

where $R_0 = 1.21\ fm$ is an empirical constant and M is a nucleon mass taken to be equal for neutrons and protons. Assuming nearly constant binding energy per one nucleon in all nuclei $B/A \approx 7 - 8$ MeV as the energy above the Fermi level E_f, one can estimate the average depth V_0 of the potential well:

$$V_0 = E_f + B/A \approx 40 MeV. \tag{1.5}$$

A more accurate description of the single-particle states can be obtained by solving the Schrödinger equation for the system of N nucleons in the potential of the Spherical Harmonic Oscillator (SHO): $V(r) = (1/2)M\omega^2 r^2$, where ω is the oscillator frequency and M is a nucleon mass. The resulting single-particle levels belong to specific oscillator shells which can be characterized by a set of quantum numbers such as the orbital angular momentum, parity etc. Although the SHO potential doesn't describe correctly the nuclear mean field, it is sometimes also convenient for the qualitative estimates, *e.g.* to calculate the energy gap between two neighboring oscillating shells [27]:

$$\hbar\omega \approx 40 A^{-\frac{1}{3}} MeV. \tag{1.6}$$

Due to the short-range nature of the nuclear forces, the shape of the mean field potential has nearly the same radial dependence as the density of the nuclear medium, which in a first approximation can have a rectangular shape (like in the Fermi-gas model) or the form of SHO potential, and can be improved later by the Woods-Saxon potential, which takes into account the effect of the nuclear surface.

A crucial step in the development of the nuclear shell model was made by Maria Goeppert-Mayer and J. Hans D. Jensen [28, 29], who added a strong spin-orbit interaction $V_{ls} = U(r)\mathbf{ls}$ to the spherically symmetric mean-field potential $V(r)$. In general form the resulting shell potential $V_s(r)$ can be written as follows:

$$V_s(r) = V(r) + V_{ls}. \tag{1.7}$$

The addition of the spin-orbit interaction results in the energy splitting of the states with different projections of the nucleon spin on the orbital momentum **l**: $\mathbf{j} = \mathbf{l} \pm 1/2$, which were previously degenerated in the spin-independent potential. This leads to a natural occurrence of the population numbers in the main shells (see figure 1.3). Further improvements of the shell potential take into account deformation of the nuclear shape and various residual interactions which result in the population of the states lying above the Fermi level.

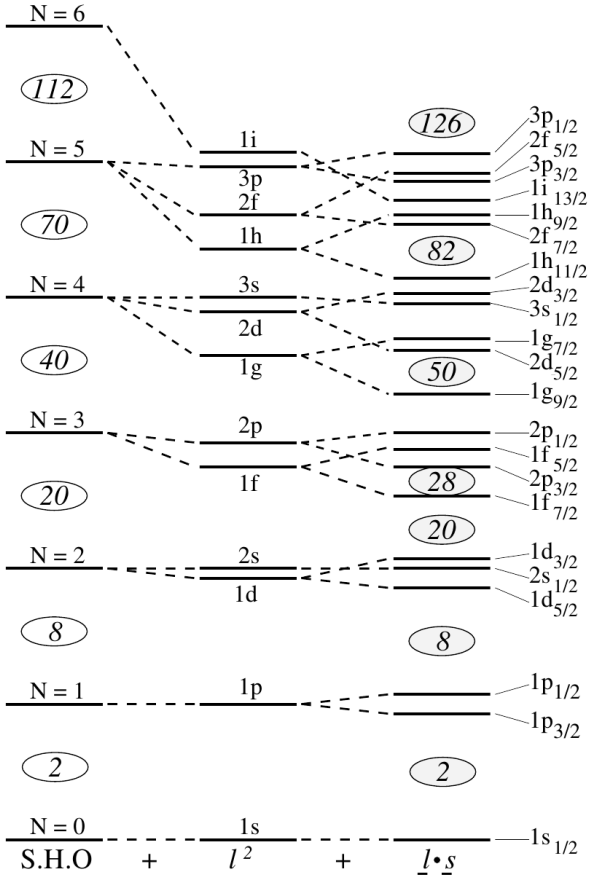

Figure 1.3: Schematic illustration of the nuclear shell model. Energy levels of the Spherical Harmonic Oscillator are shown on the left-hand side with N indicating the oscillating shell (i.e. the number of oscillating quanta), and the numbers inside ellipses denote the maximum amount of nucleons which populate all underlying states. The right level scheme represents the shell potential with an additional spin-orbit interaction. The degeneracy of the states with different spin-orbital projections is canceled out, which leads to the rearrangement of the single-particle states and the occurrence of "magic" numbers. The picture is taken from [30].

The major evidence of the correctness of the shell model is the existence of the so called "magic" even numbers of neutrons and protons (N or Z = 2, 8, 20, 28, 50, 82 and N = 126) which correspond to the closures of the main shells. The nuclei with a "magic" N or Z are associated with a peculiar rigidity relative to weak excitations and to the separation of a nucleon. Among other direct experimental evidences of the nuclear shell structure are polarization effects observed in collisions of nucleons with nuclei, the energy spectra of low-lying excited states in magic nuclei, the internal momentum distributions of nucleons measured

with electron- and proton-induced quasi-free scattering reactions, etc.

Modifications of the nuclear shell structure far away from stability is an intriguing subject in the modern Nuclear Physics. This involves nuclei with a large neutron and proton excess, for which the experimental information is rather poor and a drastic change of the single-particle and shell structure is expected. These changes result in a variety of new quantum phenomena, among which are the nuclear halo [31], quenching of magic numbers [32], new collective excitation modes [33] etc.

The reactions of quasi-free scattering are known to have an outstanding sensitivity to the nuclear shell properties. However, up to now most of the experiments have been performed with stable nuclei. A very thorough overview of the results obtained by different authors was made by Jacob&Maris and is summarized in figure 1.4.

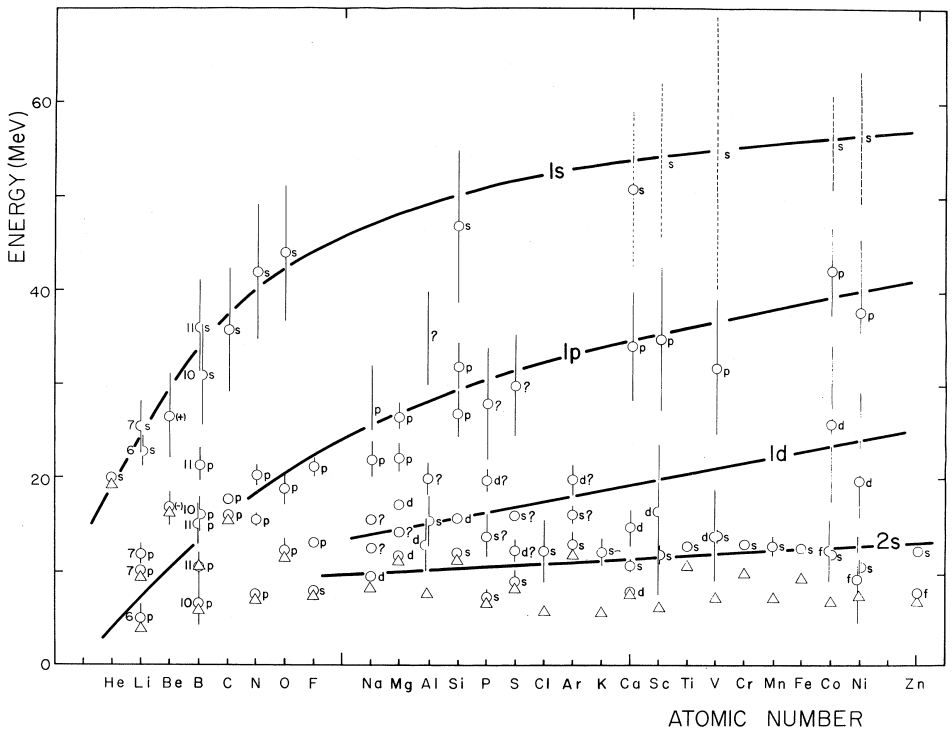

Figure 1.4: Separation energies, widths (vertical lines) and angular momentum assignments of the hole states produced in $(p, 2p)$ and $(e, e'p)$ QFS reactions as functions of the atomic number. The position of a maximum is indicated by a circle, uncertain levels are dotted; the triangles indicate the separation energies of the least bound protons, the full lines are meant to guide the eye. The figure is taken from reference [25].

1.3 Problems Involved in Quasi-Free Scattering

Let's consider the reaction of a single-nucleon removal from an initial nucleus with A nucleons and spin I forming a given final state with (A-1) nucleons and a spin I_f. The overlap function between the initial- and the final-state many-body wave functions carries the angular momentum $|I - I_f| \leq j \leq I + I_f$ and is a function of a single spatial variable. The overlap

function is then given by [34]:

$$\langle \vec{r}, \Psi_f^{A-1} | \Psi_i^A \rangle = \sum_j c_j^{if} \Psi_j(\vec{r}), \tag{1.8}$$

in terms of an expansion in single-particle states Ψ_j, where details of the angular momentum coupling are not shown. At this point one can introduce the so called spectroscopic factor which is a suitable quantity to link experimental data to theoretical calculations by different microscopic nuclear models. If Ψ_j is normalized to unity, the spectroscopic factor is determined as $S_j^{if} = |c_j^{if}|^2$. In this definition the sum rule for spectroscopic factors to all final states of the specific orbital can be interpreted as the average occupancy number of that orbital. Therefore, S_j is unity for a nucleon removal from a pure single-particle state and $(2j+1)$ for the removal from filled j subshell. If isospins T_i and T_f of the initial and final states are specified, then the spectroscopic factor is represented by C^2S, with C^2 the square of the isospin coupling coefficient.

The theoretical cross-section for populating a given final state of the residue by removing a nucleon with given single-particle quantum numbers (nlj) can be written as:

$$\sigma_{th}(I_f) = \sum_j C^2 S(I_f, nlj) \sigma_{sp}(nlj), \tag{1.9}$$

where $\sigma_{sp}(nlj)$ is a single-particle cross section computed with normalized nucleon-residue wave function Ψ_j of given n.

It has been found in many experiments ([35] and links there) exploring different types of one-nucleon knockout reactions on stable nuclei, that the spectroscopic strengths of the single-particle states are quenched by about 40% with respect to theoretical shell-model calculations (figure 1.5). The quenching factor is often interpreted as the occupancy percentage of the valence single-particle states relative to the prediction of the shell model. These results are also verified by $(e, e'p)$ experiments. Further investigations of the knockout reactions on nuclei with large proton-neutron asymmetry (left and right side of figure 1.5) have revealed a systematic change in the reduction factor which is strongly correlated with the nucleon separation energy linked to the nuclear symmetry energy [36]. However, the quenching factors for these nuclei are still arguable. The main argument against this is that the knockout reactions with light nuclei suffer from a strong surface selectivity, which minimizes the probability of the interaction with strongly bound states located deeper in the nuclear interior. On the other hand, quasi-free scattering reactions are proven to be sufficiently sensitive to the deeply bound shells, and it would be therefore interesting to verify the quenching effect in the neutron-proton asymmetric nuclei via QFS measurements.

The mechanism of the proton quasi-free scattering is much more simplified compared to the aforementioned knockout reactions, where the ambiguity due to the stripping and diffractive reaction mechanisms has to be considered. For the proton-induced knockout reactions the process is essentially determined by the proton-nucleon interaction. However, there are certain difficulties involved into this consideration. The first is how to describe correctly the proton-nucleon cross section inside the nucleus at certain energy regime. Usually, it is taken from the scattering experiments with free nucleons that is also well described theoretically, although the interaction properties may change in the nuclear medium and some sort of effective interaction has to be considered. In addition to this, one has to take into account that the knocked-out nucleon initially is not at rest since it participates in the internal motion of

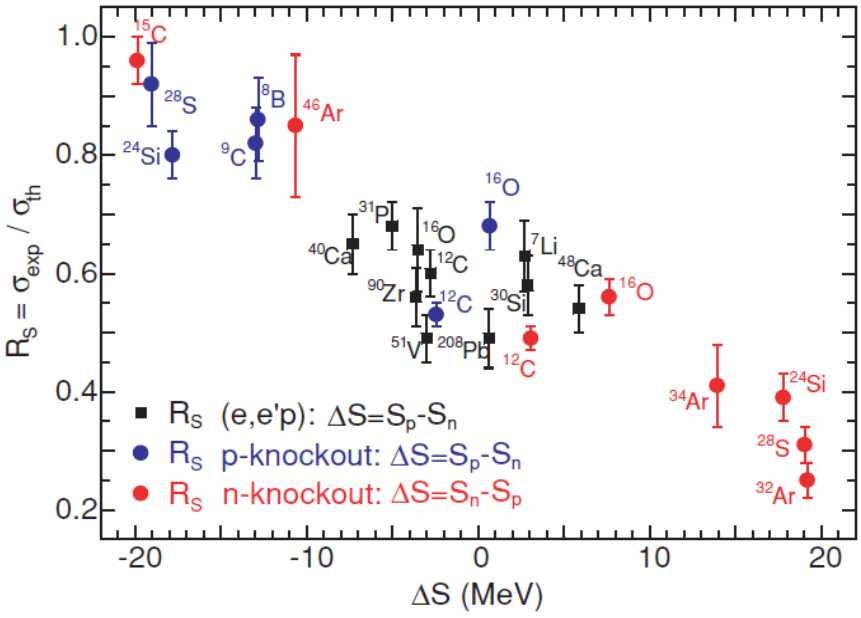

Figure 1.5: Reduction (quenching) factor of the measured nucleon removal cross sections σ_{exp} relative to the theoretical values σ_{th} as a function of the difference in separation energies of the two nucleon species. Combined data from various types of the experiments are used (different colors). The picture is taken from [35].

the nucleus. Secondly, the absorption effects in the nuclear medium cannot be fully neglected as they may distort the wave functions of both incoming and outgoing particles. This can be taken into account in the Distorted Wave Impulse Approximation (DWIA) approach by selecting an appropriate form of the imaginary part of the complex optical potential. The differential cross-section estimated within the DWIA can be then written in a general form as follows:

$$\frac{d^3\sigma}{d\Omega_1 d\Omega_2 dE_1} = C^2 S F_{kin} \frac{d\sigma}{d\Omega_{pN}} G(\vec{k_3}), \tag{1.10}$$

where $d\Omega_1$ and $d\Omega_2$ denote elements of a solid angle for the first and second scattered particle, C^2S is a spectroscopic factor, F_{kin} is a kinematical factor, $d\sigma/d\Omega_{pN}$ is the cross section of free proton-nucleon scattering and $G(\vec{k_3})$ is the distorted momentum distribution of the nucleon. The last term takes into account the internal angular momentum of the removed proton and re-scattering of the proton while escaping the nucleus.

1.3.1 Properties of Hole States

The knockout of nucleons from deeply bound nuclear shells may lead to quasi-stationary hole states. Such states have been confirmed in nuclei up to A≈40 and their separation energies and total widths (Γ) have been measured. For heavier nuclei the experimental data is insufficient due to stronger distortions effects reducing the reaction yields for these states. There are two main issues usually discussed in this respect. The first is how to describe and to identify the reactions and how to account for the secondary processes interfering with the

measurements. The second question is usually related to the interpretation of the inner shell peaks in the binding energy spectra obtained via QFS reactions. Until now the structure and the fragmentation mechanism of the deep-hole states is not well known even in light nuclei. The necessary information must be obtained not only from the measurements of the scattered particles but also from the direct observation of the final state residue and its decay properties. In a recent work by Yosoi *et al.* [37] an attempt has been made to study the fine structure and the fragmentation mechanism of the s-hole states observed in light nuclei by measuring the decay fragments emerging from the target after a $(p, 2p)$ reaction. The authors have shown that the decay mechanism of such states can be qualitatively understood via microscopic SU(3)-cluster model, and the observed fine structure can be reasonably explained by the shell model calculation.

It is also interesting to compare the theoretical spectroscopic factors for the inner shells with the experimental values. This would require specific experimental and analysis techniques as well as an appropriate reaction theory, which would correctly account for the secondary processes.

1.3.2 Experimental Issues

In a typical QFS experiment the scattered particles are detected simultaneously at certain angles relative to the incident beam and at energies E_1 and E_2, which are defined respectively by the acceptance solid angles $d\Omega_1$ and $d\Omega_2$ and the energy widths of the channels dE_1 and dE_2 in the measuring device. The geometry, in which the reaction is observed, is therefore determined by the configuration of the experimental setup. Up to now, most of the QFS experiments have been performed in a coplanar geometry, where directions of an incident and two outgoing particles are measured in one plane. From the similarity of the process with the pure elastic scattering one intuitively expects a maximum yield for such coplanar reactions, although, in principle, the reactions take place in three-dimensional geometry which is not necessarily coplanar. In such experiments, the outgoing particles are measured using magnetic spectrometers, range telescopes or thick scintillating crystals situated at specific angles and adjusted according to different expectations for the particles' energies. Usually, a set of measurements is undertaken in which the measured angles or energies are varied sequentially. Thus, the coplanar experiments can be classified into the following types [24]:

- Symmetric experiments, in which the scattered particles are chosen to have equal energy and equal angles with respect to the incident beam. Such kinematics can drastically simplify the theoretical calculations.
- Energy sharing experiments, in which the energies of the outgoing particles are varied but their angles are kept fixed. In contrast to the first case, such experiments provide larger statistics as more events can be identified.
- Experiments without any restrictions on the outgoing energies and angles.

The information, which one can gain in the noncoplanar experiment, is related to the absorption in the nucleus that may considerably reduce the cross sections when measured in the coplanar geometry. It has been pointed out by Berggren&Tyren [26], that the reduction for individual process is strongly dependent on where in the nucleus the reaction takes place, and that the absorption leads to enhanced localization of the reaction closer to polar caps of

the nucleus (in coplanar case), *i.e.* there must be a considerable amount of angular localization due to absorption. Therefore, in favorable cases, one may expect to find a diffraction pattern in the cross section, when the geometry is varied from the coplanar to the noncoplanar situation. However, this may be the case only for medium and heavy nuclei, where the polar caps are better spatially separated, and for the light nuclei no such strong effect is expected.

In most QFS experiments the internal momentum of the knocked out proton is calculated from the measured momenta of the incident and the two outgoing particles (see formula 1.2), while the recoil momentum of the spectator nucleus is not measured directly. Similarly, the separation energy of the knocked-out nucleon is reconstructed by measuring the missing energy of the scattered particles.

In the present work a somewhat different experimental approach is explored to determine the internal momenta and separation energies. It is based on the complete kinematical measurements of the QFS reaction and the reconstruction of the residual excitation energy by means of the γ-spectroscopy and invariant-mass measurements. In the inverse reaction geometry it is also possible to measure directly the recoil momentum of the reaction residue, as well as to use for this purpose redundant measurements of the scattered particles. The LAND-R^{3}B setup at GSI provides a unique opportunity for such redundant measurements. Moreover, the setup has minimum restrictions on the outgoing angles, which allows for a complete study of QFS reactions, not limited to the coplanar case. A large solid angle acceptance for the outgoing particles (almost full 2π-hemisphere in the beam direction) results in a larger reaction yield, which is especially important for the experiments with expensive exotic beams. Thus, the four-momenta of all particles before and after the reaction can be measured, and a complete set of observables can be obtained, which is sufficient for the invariant-mass analysis of the reaction products.

1.4 ^{12}C Nucleus as a Test Case

^{12}C is an ideal candidate for testing the presented experimental technique, since plenty of experimental results has been accumulated for this nucleus from QFS experiments in direct kinematics with incident protons and electrons as well as from transfer and knockout experiments. Its single-particle structure is also well established, and many theoretical calculations are available. Nevertheless, there are still some open questions even for such well investigated nucleus such as, for instance, the structure and properties of deep-lying hole states or the internal correlations between nucleons.

In the idealistic shell-model picture the ground state of ^{12}C has $(1s_{1/2})^2(1p_{3/2})^4$ shell-configuration for protons and neutrons. The QFS knockout of a single proton leads to population of a state in ^{11}B with a hole either in the valence (loosely bound) p-shell or in the inner (deeply bound) s-shell. Since the ^{12}C is a relatively light nucleus and the experimental energy of 400 AMeV is sufficiently high, the distortion effects caused by the spectator nucleons are expected to be small. Here, only two of the most recent experiments with carbon isotopes will be highlighted to give the reader an idea about the method and the difference between direct and inverse kinematics measurements.

- **Reaction ^{12}C$(p,2p)^{11}$B in direct kinematics**

The reaction ^{12}C$(p,2p)^{11}$B was studied in direct kinematics, using a proton beam with an energy of 392 MeV [37]. High-precision energy measurements of the outgoing proton

pairs were achieved with the aid of a dual magnetic spectrometer system situated behind the carbon target. The settings of the spectrometers were optimized for a knockout from the deeply bound $1s_{1/2}$ shell, *i.e* when the recoil momentum is zero, at which situation the reaction yield for the s-shell is maximum. In addition to this, the target was surrounded by a number of detectors to measure decay products of highly excited states of the residual ^{11}B.

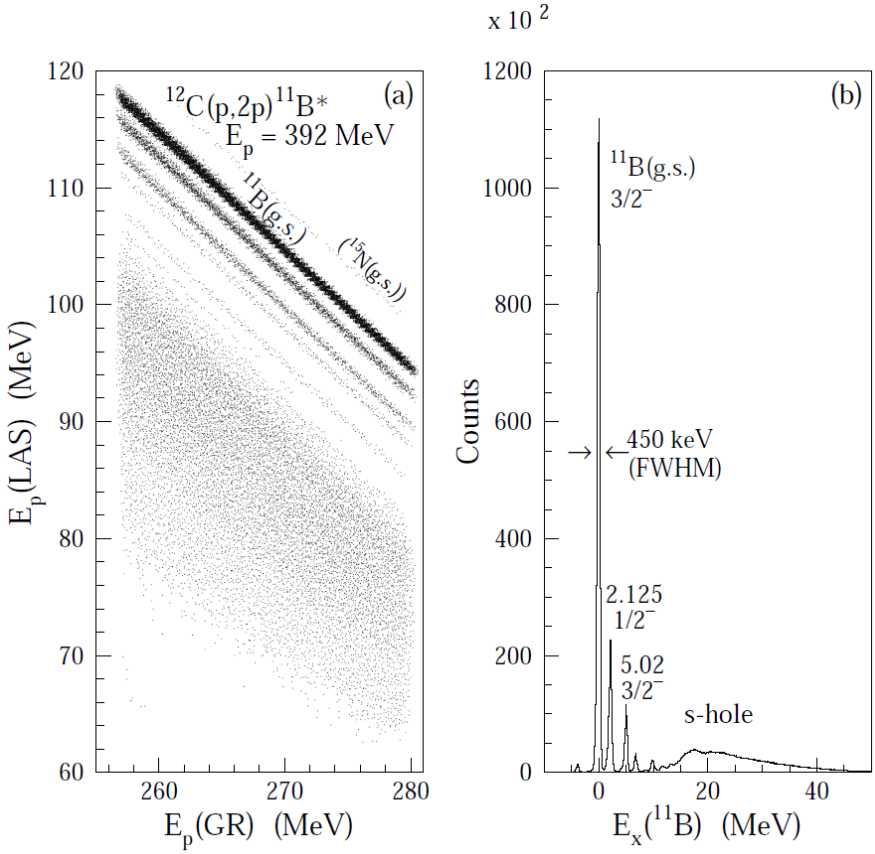

Figure 1.6: The reaction $^{12}C(p, 2p)^{11}B$ was measured in direct kinematics. The figure on the left side represents the energy correlation of the two outgoing protons. The contributions from strongly and loosely bound single-particle states can be observed as broad and narrow bands, respectively. On the right figure is the corresponding excitation energy spectrum of the residual ^{11}B reconstructed from the energy measurements of the two protons. The s- and p-hole states in ^{11}B can be recognized in the spectrum. The figure is taken from [38].

In figure 1.6 (left) the correlated patterns in proton energies represent different single-particle states. The corresponding excitation spectrum of ^{11}B is shown in the same figure (right). The contribution from valence p-shell protons can be seen as narrow peaks of low-lying discrete states below 10 MeV (also narrow bands in the energy correlation graph). A broad bump at around 20 MeV stems from the s-shell knockout. Due to an extraordinary short life-time of the s-hole state its peak is much broader compared to the p-shell states. Some fine structure of that peak is observed and explained by the authors as an effect of the fragmentation of the s-hole state with respect to different decay channels. Also in the energy correlation plot the s-state appears as the wide band at lower energies.

- **The reaction ^{12}C$(p,2p)^{11}$B in inverse kinematics**

Recently, an attempt to study $(p,2p)$ reactions in inverse kinematics was undertaken for carbon isotope beams of $^{9-16}$C at 250 AMeV impinged on a solid-hydrogen target [39]. Energies of the outgoing protons were measured by two proton telescopes set at $\pm 39^{\circ}$ with respect to the beam. The forward moving boron isotopes $^{A-1}$B produced in the reactions were measured by a magnetic spectrometer after the target. The resulting proton separation energy distributions, deduced from the measurements in the two telescopes, are shown in figure 1.7. As seen, the separation energy spectrum for ^{12}C is consistent with the excitation spectrum of ^{11}B obtained in the direct kinematics measurement, although the experimental resolution $\sigma(S_p) \sim 1.3$ MeV is much worse mainly due to the limited angular resolution of the telescopes. Nevertheless, from these spectra it is possible to disentangle the knock-out from $1p$ and $1s$ shells by setting appropriate energy gates (in this experiment - the proton-emission thresholds).

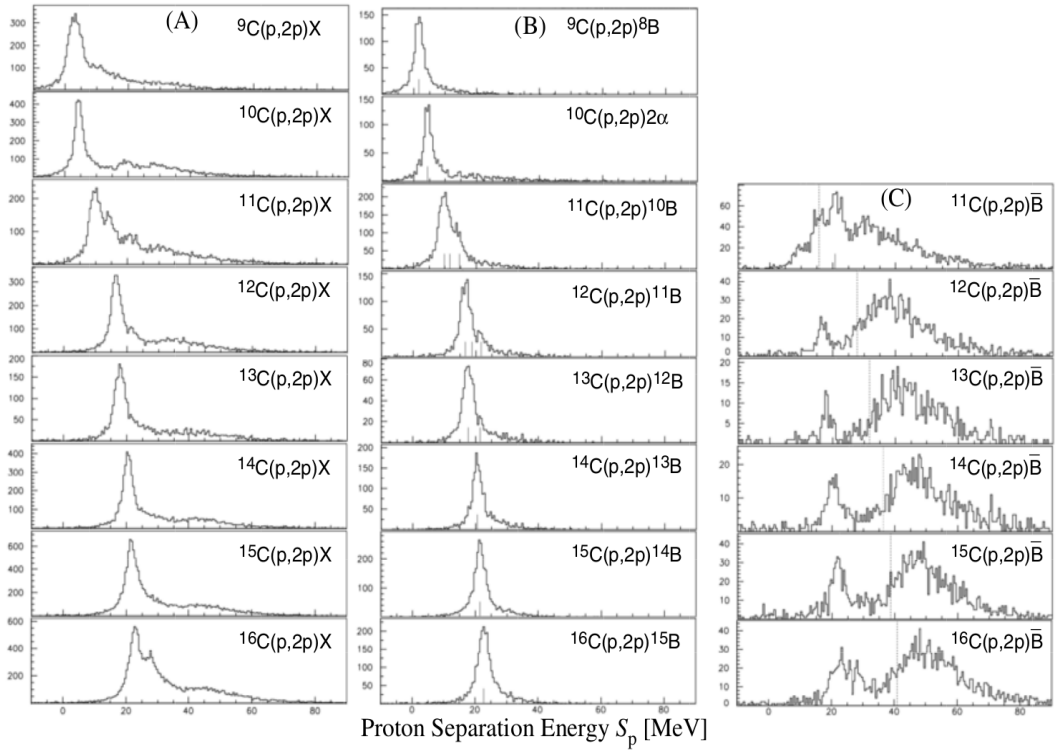

Figure 1.7: Proton separation energy spectra measured in $(p,2p)$ reactions with carbon isotopes. Column (A) shows the total spectra, (B) - when boron isotopes are observed in the final state (p-hole states), (C) - when no outgoing boron isotopes are detected (s-hole states). The most pronounced peaks at low energies are mainly contributed by knockout to the ground state. The figure is taken from [39].

The measured momentum distributions of protons occupying s- and p-orbitals are shown in figure 1.8. Due to the weak binding of valence protons in the proton-rich side and stronger on the neutron-rich side, the corresponding momentum widths of the p-hole states increase with the isotope's mass as well as the ones of the s-hole states.

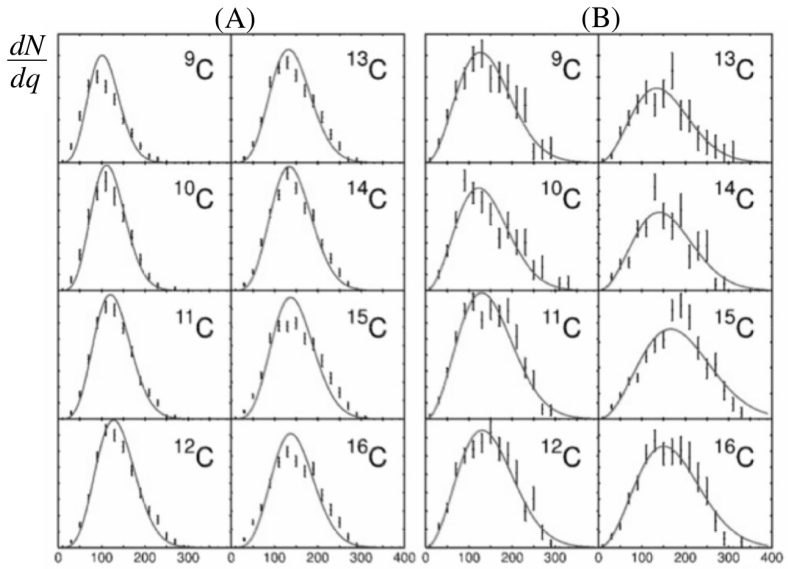

Figure 1.8: Proton momentum distributions in different carbon isotopes. (A) and (B) correspond to the knockout from the p- and s-shell, respectively. The figure is taken from [39].

1.5 The R^{3}B Setup at FAIR

An essential part of the physics program at the future R^{3}B setup at FAIR will be dedicated to quasi-free proton scattering experiments in inverse kinematics. The main goal of this program is to explore the single-particle and cluster structure of neutron- and proton-rich exotic nuclei. It will be achieved via complete kinematics measurements of the reactions with secondary beams of isotopes produced via in-flight fragmentation of primary beams with high intensities ($\approx 3 \times 10^{11}$ ions/s) and high energies (≈ 2 AGeV for ^{237}U beam).

As a part of a larger experimental project known as NuStAR (Nuclear Structure, Astrophysics and Reactions) the R^{3}B experiments will also focus on other topics involving short-lived radioactive beams far from stability (see table 1.1). This will include direct studies of the nuclei that are involved in the processes of energy production and element synthesis in stellar environments, in particular the r-process. Besides that, the new setup will enable investigations of the collective excitation modes, low-lying resonances, halo and skin structures in the nuclei with a large isospin asymmetry etc.

The prototype design of the R^{3}B-setup is shown in figure 1.9. Incoming radioactive-ion beams (RIB) will interact with a liquid-hydrogen target surrounded by the silicon tracking system and a large calorimeter for measuring outgoing pairs of particles from the reactions such as $(p, 2p)$, (p, pn), (p, pd) etc. and also for the γ-ray spectroscopy. A crucial part of the future setup will be a high-resolution magnetic spectrometer, which will provide measurements of the outgoing reaction fragments in either large-acceptance mode or high-resolution mode (see figure 1.9) with relative momentum resolution of about 10^{-4}. The tracking systems after the magnet will identify and measure all forward-moving fragments, which would allow for full kinematics measurements and invariant-mass reconstruction of the reaction products.

The existing LAND-R^{3}B setup at GSI in Darmstadt serves as a prototype for the future R^{3}B facility. The experimental and analysis techniques which are developed for the present setup will become a basis for the future R^{3}B experiments. The present work aims at testing

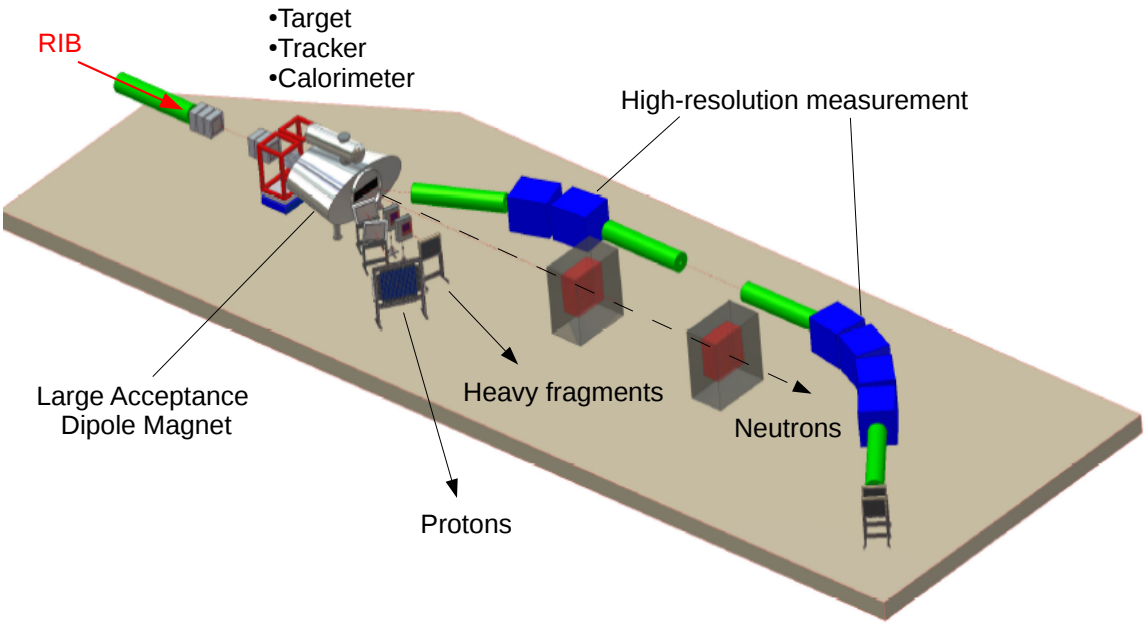

Figure 1.9: A prototype design of the R^3B setup at FAIR

Reaction type	*Physics goals*
Total-absorption measurements	Nuclear matter radii, halo and skin structures
Elastic p scattering	Nuclear matter densities, halo and skin structures
Knockout	Shell structure, valence-nucleon wave function, many-particle decay channels unbound states, nuclear resonances beyond the drip lines
Quasi-free scattering	Single-particle spectral functions, shell-occupation probabilities, nucleon-nucleon correlations, cluster structures
Heavy-ion induced electromagnetic excitation	Low-lying transition strength, single-particle structure, astrophysical S factor, soft coherent modes, low-lying resonances in the continuum, giant dipole (quadrupole) strength
Charge-exchange reactions	Gamow-Teller strength, soft excitation modes, spin-dipole resonance, neutron skin thickness
Fission	Shell structure, dynamical properties
Spallation	Reaction mechanism, astrophysics, applications: nuclear-waste transmutation, neutron spallation sources
Projectile fragmentation and multifragmentation	Equation-of-state, thermal instabilities, structural phenomena in excited nuclei, γ-spectroscopy of exotic nuclei

Table 1.1: Physics program of the R^3B project at FAIR

and verifying the feasibility of the proposed experimental approach to measure QFS reactions of the type $(p, 2p)$ and (p, pn) in inverse kinematics. The benchmark experiment was performed in 2007 and the results are presented in this thesis.

Chapter 2

Experimental Apparatus

2.1 Beam Production at GSI

A bird-eye view on the heavy-ion beam facility at GSI Helmholtzzentrum für Schwerionenforschung in Darmstadt (Germany) [40] is shown in figure 2.1.

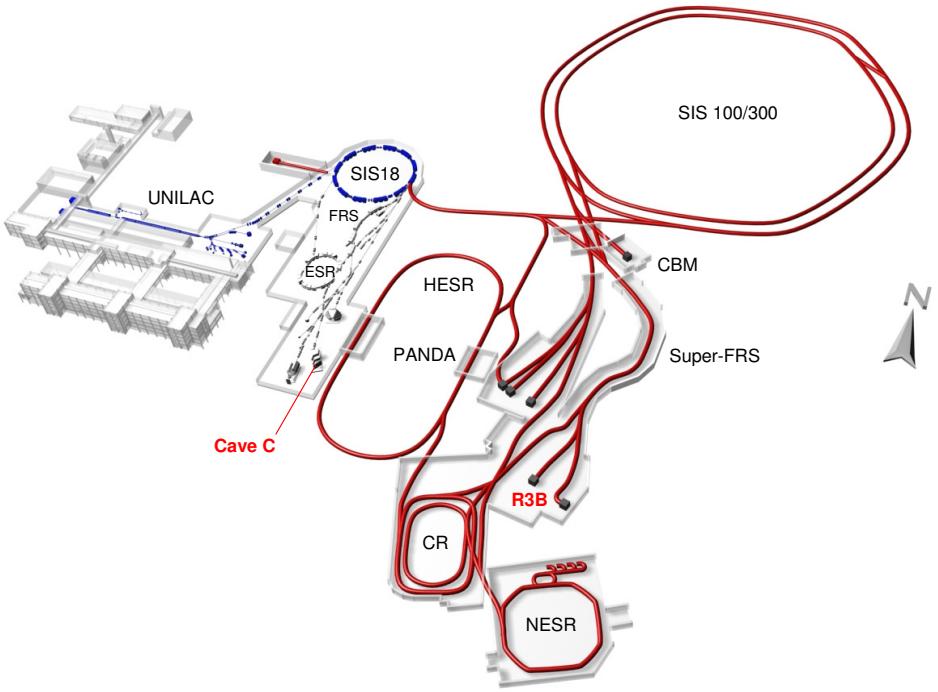

Figure 2.1: Layout of the current heavy-ion beam facility (left, blue color) at GSI is shown together with the future FAIR facility (right, red color). The existing LAND-R^{3}B setup in Cave C is designed as a prototype for the planned R^{3}B laboratory, which is also indicated in the figure.

On the first acceleration stage a low-energy beam of stable isotopes is extracted from the primary ion-source and injected into UNIversal Linear Accelerator (UNILAC), where it is accelerated up to maximum energy of 11.4 AMeV. The ejected beam from the UNILAC is

transported for further acceleration to SIS 18[1], a heavy-ion synchrotron, which is capable of producing stable-ion beams in a wide range of atomic masses with the maximum energy up to 1 GeV/u and 4.5 GeV/u for ^{238}U and protons, respectively. The resulting beam from the synchrotron can be used for different purposes. For example, it can be impinged on a light nuclear target, like beryllium, to obtain secondary beams of radioactive isotopes, which are typically utilized in the experiments involving the Experimental Storage Ring (ESR) or the FRagment Separator (FRS). In the present experiment a primary ^{12}C beam with an energy of 400 AMeV and an intensity about 10^5 nuclei per second was transported directly to the experimental setup in Cave C.

2.2 The LAND-R^{3}B Setup

A schematic layout of the full kinematics setup in Cave C is shown in figure 2.2. The presented configuration has been chosen to be similar to the prototype design of the future R^{3}B setup at FAIR (see figure 1.9). At the entrance of the experimental hall the incoming ^{12}C beam traversed position sensitive silicon detectors PSP1 and PSP2[2]. The detectors were intended for tracking the incoming beam, however, in the present experiment they could not be used due to insufficient energy loss of the carbon ions to produce proper signals. Both PSPs will be excluded from the following consideration, and only a slight decrease of the beam energy in these detectors will be taken into account for the analysis. The lack of tracking information for the incoming beam can be partially compensated by position measurements in the silicon microstrip detectors located downstream after the target, as explained in section 4.4.1. In addition to the tracking detectors, the beamline before the target was equipped with a beam collimator ROLU[3] and a thin scintillating detector POS[4], which was aimed at time-of-flight measurements.

A hydrogen target (CH_2) was located inside the Crystal Ball calorimeter, which measured γ-rays and protons emerging in QFS reactions. To obtain angular information about reaction products, the target area was additionally equipped with an array of six double-sided Silicon MicroStrip Detectors (SSDs). The forward moving fragments were deflected in the ALADIN[5] magnet and were further measured in the corresponding detection systems. The neutrons were detected by a Large Area Neutron Detector (LAND), the heavy fragments were tracked via two scintillating fiber detectors GFIs[6] and a small time-of-flight wall NTF[7]. Similar to the fragments, the kinematically focused protons, stemming from decay of excited reaction fragments, were measured behind the magnet via two Proton Drift Chambers (PDC) and a large Time-of-Flight Wall (TFW). The following sections contain more detailed information about each detection system.

2.2.1 The POS Detector

The POS is used as a starting reference for the time-of-flight measurements and as a trigger for the incoming beam. It is situated at a distance of about 2 m before the target, between

[1] SchwerIonen-Synchrotron.
[2] Position Sensitive silicon Pin diode.
[3] From German names of the movable scintillators in the collimator "Rechts", "Oben" "Links", and "Unten".
[4] Position detector.
[5] A LArge DIpole MagNet.
[6] Gross Fiber Detector.
[7] New Time-of-Flight wall.

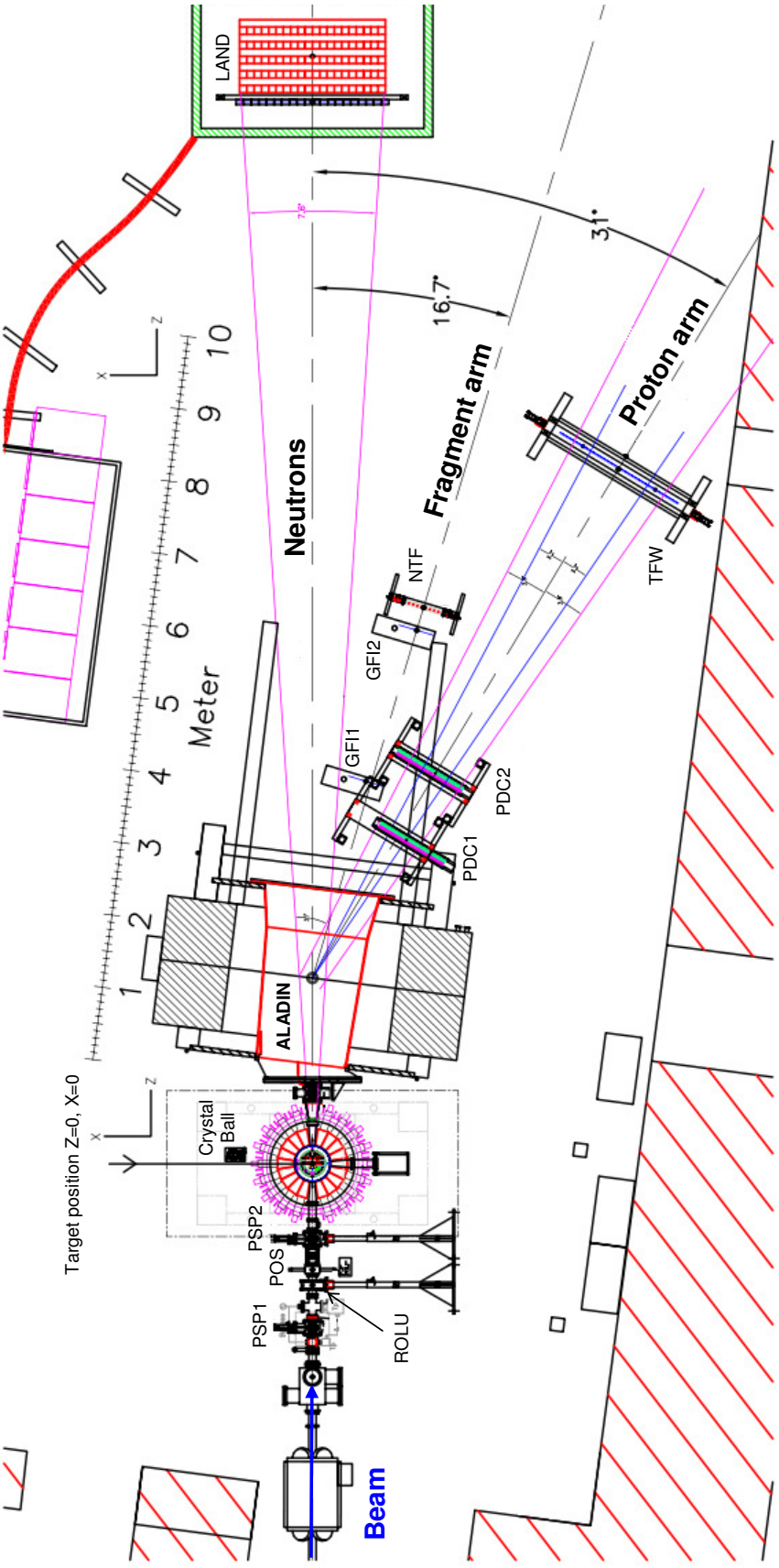

Figure 2.2: The LAND-R^{3}B setup in Cave C. At the entrance of the experimental hall the incoming beam is monitored via POS and collimated via ROLU onto the reaction target. The target and silicon trackers (not shown) are situated inside the Crystal Ball detector, which measures protons and γ-rays emerging from the target. The outgoing forward-focused reaction fragments are measured in the corresponding tracking systems after the ALADIN magnet.

PSP1 and PSP2. A principal design of the detector is shown in figure 2.3.

The active area of POS is represented by a 5×5 cm^2 plastic scintillator with a thickness of about 200μm. When a charged particle hits the scintillator, it produces light, which is registered by four photomultiplier tubes (PMTs) attached to every side of the scintillator. An integrated charge and arrival time of a signal in every PMT are recorded and used to determine energy loss, time and position of a particle hit in the scintillator.

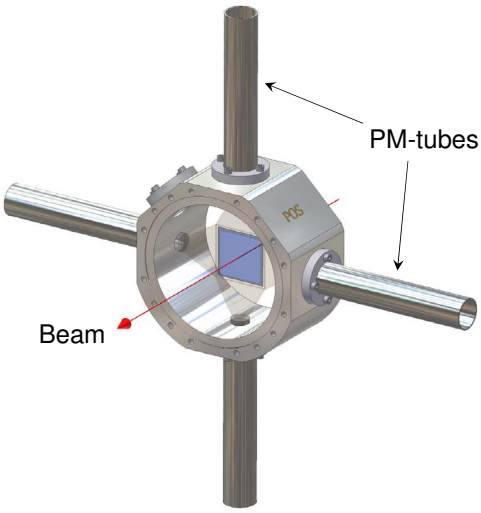

Figure 2.3: The plastic-scintillator detector POS provides time measurements and a trigger for the incoming beam. A light signal created by the penetrating ion in the scintillator (blue) is read out by four PM-tubes.

2.2.2 Double-Sided Silicon Microtrip Detectors

The type of reactions intended for the present study imposes a set of requirements on the design of tracking detectors located in the vicinity of the target. Firstly, due to a strong kinematical focusing of the reaction fragments in the forward direction, the trackers are expected to be highly granular, in order to obtain a reasonable position resolution. Secondly, a wide dynamic energy range of the detectors is important for identification of various nuclear species. Moreover, the detectors need to have a low noise level and to be multihit capable. All these requirements are met by AMS-type [41] double-sided silicon microstrip detectors (SSDs) adopted in the present experiment. They have been specially developed for tracking high-energy cosmic rays (from protons to iron) as an essential part of the Alpha Magnetic Spectrometer (AMS) [42] operating on board of the International Space Station (ISS).

The detection principle in the SSDs is based on creation of electron-hole pairs along the particle trajectory in the depleted semiconducting silicon volume. Due to the presence of an electric field in the volume, the created charges drift towards nearest strip sensors, which cover the silicon bulk from two sides, orthogonally to each other. Thus, an accurate position of the hit on a plane and the energy loss (*i.e.* charge) of the particle can be measured. An implantation pitch on the junction side (p- or S-side) is 27.5 μm with the corresponding readout pitch of 110 μm, *i.e.* only each fourth strip is read out while others are left floating. The charge collection in the floating strips is achieved through capacitive couplings between the strips that enables to get a position resolution with the readout pitch larger than the

Figure 2.4: A design of the AMS-type silicon microstrip detector. The double-sided 0.3 mm thick silicon sensor has the dimension 72×41 mm^2. The number of readout channels is 640 on the long S-side and 384 on the short K-side. The attached front-end electronics board (green) is used to read out signals from the strips.

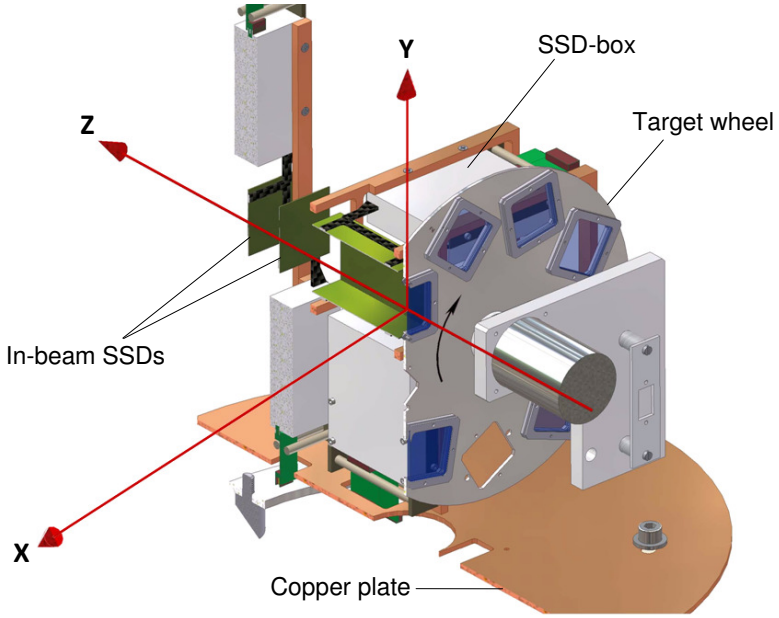

Figure 2.5: The cross-section view of the installation inside the target chamber. Six silicon trackers (green) together with the target-wheel (blue) are fixed on a copper plate. The laboratory coordinate system is shown in red. Z-axis coincides with the beam direction. The target can be changed during the beam time via rotating the target-wheel which is remotely controlled.

implant pitch. On the ohmic (n- or K-side) the implant pitch is 104 μm with every strip being read out. It has been demonstrated [41] that the position resolution of about 10 μm can be achieved with up to 200 μm readout pitch, that corresponds to roughly 1 mrad of angular resolution in the present experimental geometry.

Signals from individual readout strips are preamplified and shaped via DC-coupled VA-chips (64 strips per one chip), which transfer the signals further to the operational amplifiers in the front-end electronics board (see figure 2.4). The output signals are generated separately for the K- and S-side by the front-end electronics, which send the signals to an external custom-designed readout module SIDEREM[8] (see [43] for more information).

In total six SSDs were located inside the evacuated aluminum target chamber as shown in figure 2.5. Two detectors were inserted into the beam line at a distance of 11 cm and 13.5 cm downstream from the target to identify and to track the outgoing reaction fragments. The other four SSDs were assembled into $41\times41\times72$ mm^3 box around the target for measuring the QFS protons.

It should be noted, that the SSDs are rather "slow" detectors. It takes the readout electronics approximately 5 μs to digitize the output signals for all 1024 channels of a single SSD. Therefore, the SSDs are inappropriate for any sort of time measurements and, as a consequence, they cannot be used for triggering purposes. Instead, an external trigger coming from other parts of the setup is always used for these detectors.

2.2.3 The Crystal Ball

The Crystal Ball (CB) is a large calorimeter aimed at the detection of photons and light charged particles. It consists of 162 NaI(Tl) scintillating crystals folding into a sphere around the target. Each crystal is 20 cm long and is canned in 600μm thick aluminum shell. The inner volume of the CB contains the evacuated aluminum target chamber with a supportive construction holding the target-wheel and the SSDs (figure 2.5). The geometrical center of the CB coincides with a point at the downstream surface of the target, which is also chosen to be the origin of the laboratory coordinate system. The view of the CB as well as the rest of the experimental section before the ALADIN is shown in figure 2.6.

The scintillating light produced by photons or by charged particles in individual crystals is converted into electric signal in the PM-tubes attached to the outer flanges of the crystals. The initial design of the CB was intended for γ-ray detection only, however, the energy deposited by a high-energy proton in one crystal can be one or two orders of magnitude higher compared to the energy of γ-rays, that results in intense light pulses and, consequently, in overflow signals generated by the corresponding PMT readouts. For the sake of measuring proton energies, the configuration of some PMTs have been slightly modified [44], so that additional "low-gain" (or "proton") readouts have been implemented on 64 crystals located in the forward (with respect to the beam) hemisphere, where the most of the proton pairs from QFS reactions are expected to be observed. In each of these PM-tubes a signal is additionally read out before the last preamplification stage on the dynode sequence, hence providing a doubled energy measurement ("low-gain" and "high-gain") of the same signal in one crystal. Besides the energy, also the timing of signals can be measured, giving a possibility for triggering on either photons (low energy) or protons (high energy).

2.2.4 The Fragment Arm

After the target, the outgoing reaction fragments have to be identified and measured. It is achieved with the aid of a dipole magnet ALADIN situated approximately 2 m away from the target and via the fragment tracking arm after the magnet.

[8] SIlicon DEtector Readout Module.

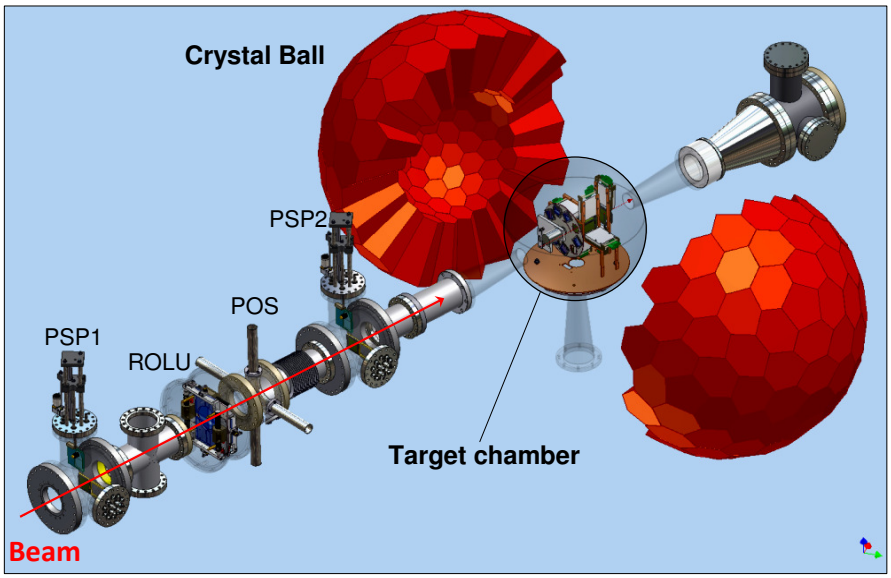

Figure 2.6: View of the Crystal Ball calorimeter and the experimental section before the ALADIN magnet. The target chamber with six Si-microstrip detectors is situated inside the calorimeter. 162 NaI(Tl) crystals cover almost entire 4π solid angle around the target.

Due to the Lorentz force, which acts on charged particles moving through the magnetic field, the trajectories of fully stripped fragments are bent in the magnet depending on their A/Z ratios. Thus, different isotopes travel along different trajectories. The electric current of the magnet was adjusted in a way that the fragments with A/Z≈2 (*i.e.* similar to ^{12}C), were deflected by 16.7° with respect to the incident beam.

Behind the magnet, at a distance of 3 m and 5 m, two GFIs (see figure 2.7) measured trajectories of the fragments in the dispersive plane of the magnet. Each GFI consists of 480 vertical 1 mm thick scintillating fibers arranged in a single row, which forms a sensitive area with a total size of 50×50 cm^2. The scintillating light produced by a charged particle in a fiber is guided onto the cathode mask of the position-sensitive photomultiplier (Hamamatsu R3941). The light signal from each fiber arrives at a specific spot on the cathode and initiates an electron avalanche towards the anode, where the signal appears as a local charge distribution on the two dimensional anode grid represented by 16 and 18 perpendicular readout wires. The center of gravity of this charge distribution is strongly correlated with the initial position of the light spot on the cathode, that is in turn associated with a specific fiber and the X-coordinate in lab. More detailed information about the detectors and the hit reconstruction algorithm can be found in [45, 46]. A horizontal position resolution of about 1 mm can be achieved, which corresponds to the thickness of a single fiber.

Next after the GFIs, the NTF measured the time of flight and the energy losses of the fragments. The NTF consists of two layers of 50 cm long scintillating paddles arranged in vertical and horizontal order as shown in figure 2.8. Each paddle is read out by two PM-tubes at the ends. The measured electrical pulses in the PMTs are related to energy loss ΔE in the paddle and, therefore, to a charge of the passing ion. The NTF provides position and time-of-flight information with a resolution (sigma) of about 5 cm and 30 ps, respectively. A trigger for fragments is also generated by the NTF. Combining the measurements in both GFIs and

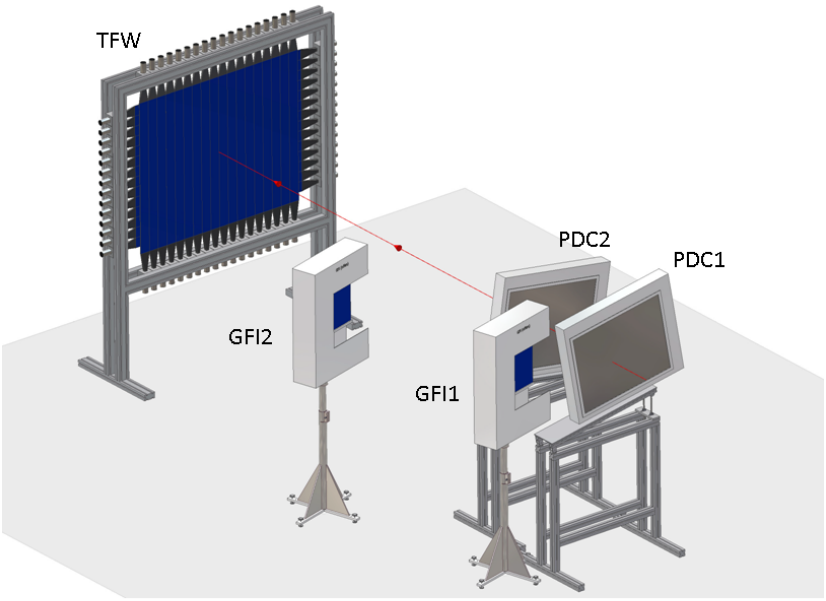

Figure 2.7: View of the tracking systems behind the ALADIN magnet. Only two GFIs without NTF are shown for the fragment arm. PDC1 and PDC2 are used for tracking protons and the TFW provides the corresponding proton trigger and the time-of-flight information.

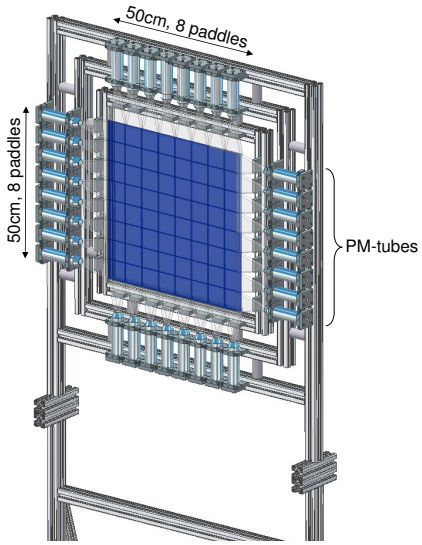

Figure 2.8: View of the small ToF-wall (NTF), which was situated at the end of the fragment arm.

in the NTF with the known field map of the magnet, one can reconstruct trajectories of the fragments, their masses and total momenta.

2.2.5 The Proton Arm

Similar to heavy fragments, the protons are tracked via two drift chambers (PDCs) placed at 2.5 m and 3.5 m behind the magnet and the TFW in the end. One should note, that the protons which are measured here are not the ones emerging in QFS reactions, but rather

in the breakup of highly excited residual states. The QFS protons are expected to emerge at around 40° angle relative to the beam, where they are measured by the Crystal Ball as explained before. Since protons have $A/Z = 1$ and velocities approximately equal to the one of heavy fragments, the deflection angle in the magnet is larger than for the fragments. At the same magnet settings, the average deflection for protons was about 31° relative to the incident beam.

The PDC is a wired chamber filled with a gas mixture (20%CO_2 + 80%Ar), which is ionized when a charged particle passes through. The produced charge cloud drifts in the electric field towards the nearest sense and field wires, where the electric current is measured and used for reconstructing the exact location of the proton track between the two wires. Each PDC consists of two orthogonal planes of the gas-floating wires with a total active area of about 80×100 cm^2 for measuring vertical and horizontal coordinates. Due to a high granularity, the position resolution of about 200 μm can be achieved. The PDCs were tilted by 30 degrees relative to each other in order to eliminate an ambiguity in reconstructing tracks for multi-proton events.

A large time-of-flight wall (TFW) with 18×16 paddles was completing the proton arm. By analogy with the NTF it served for the energy loss, position and time-of-flight measurements. The design and the operation principle are also very similar to the ones of the NTF. The spatial dimensions of vertical and horizontal paddles are 10.4×154.6×0.5 cm^3 and 10.4×196.6×0.5 cm^3, respectively. The estimated position and time resolution for protons is 10 cm and 500 ps.

2.2.6 The Neutron Detector

Neutrons are not influenced by the Lorentz force in the field of ALADIN, because they are not charged particles and, therefore, they distribute at around 0° outgoing angle after the magnet. Since the interaction cross section of relativistic neutrons with matter is small, the measurements rely on a specific detection principle and a large active volume of the detector in order to increase the efficiency. The neutron detection is based on conversion of neutron hits inside iron material into a shower of charged particles, which in turn can produce light in the scintillating material. A schematic view of the LAND detector, which was located at around 14 m after the target, is given in figure 2.9. The detector consists of ten identical 2×2 m^2 planes composed of 20 horizontal or vertical paddles. Each paddle is a composition of alternating 5 mm thick plastic-scintillator sheets and 5 mm thick iron sheets, and two PM-tubes are attached to the ends of a paddle. The times and charges in the PM-tubes are readout by TDCs and QDCs, respectively. This information is used for reconstruction of the time and location of a hit within the paddle. The other two coordinates are determined by the absolute position of the paddle in the detector. The LAND can provide high-efficiency time-of-flight measurements of neutrons with energies ranging from 0.1 to 1 GeV. A total depth of the detector's active volume is about 1 m that is sufficient to reach an absolute efficiency of more than 90% for 1 GeV neutrons [47] and a time resolution of approximately 250 ps.

2.2.7 Targets

For the purpose of the present research a hydrogen target was required. From a practical point of view a CH_2 target is preferable, because it is more compact than a pure hydrogen

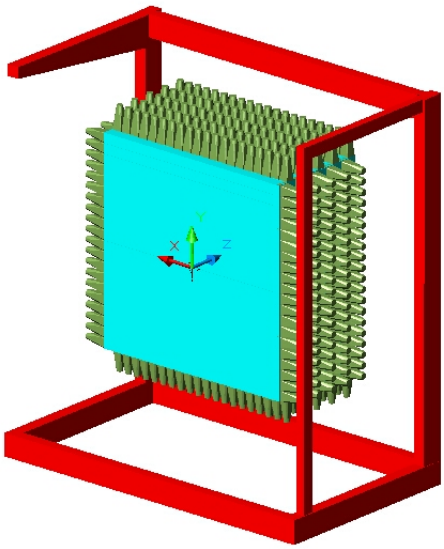

Figure 2.9: Large Area Neutron Detector (LAND) consists of ten 2×2×0.1 m^3 planes. Each plane is composed of twenty horizontal or vertical scintillating paddles.

target (gas or liquid) and is easier to handle. Neglecting the carbon component, the CH_2 can be considered as a hydrogen (or proton) gas confined in the volume of the target sample, where the reaction can occur. However, the carbon constituent also contributes into the total reaction yield and causes an additional straggling of the beam. In order to estimate this background, complementary measurements with a pure carbon target were conducted.

Target	Thickness	Density	Atomic Mass	Area Density
CH_2	2.31 mm	0.92 g/cm^3	14 u	9.1418×10^{21} /cm^2
Carbon	2.01 mm	1.84 g/cm^3	12 u	1.8561×10^{22} /cm^2

Table 2.1: The properties of the experimental targets.

On the other hand, nucleon removal reactions on a composite nuclear target like ^{12}C, ^{9}Be, etc. can be also used to obtain an information about nuclear structure. The investigation of this reaction channel is not a main focus of the present research as it has been already studied in the previous work [48]. Hence, the measurements with the pure carbon target were mainly aimed at the background determination. The properties of the targets which have been used in the presented experiment are listed in table 2.1. In addition to this, the measurements without target were performed in order to estimate the background caused by reactions in the detectors and by random coincidences.

2.2.8 Triggers

Signals from different detectors are collected in the Data Acquisition System (DAQ), where a trigger stamp can be assigned to every event on the basis of some custom defined conditions. Usually, the signal from a triggering channel is sent to a Constant Fraction Discriminator (CFD) which produces a logical output signal with appropriate timing characteristics. Combining coincident logical signals [9] arriving from different parts of the setup, a certain trigger bit can be set in order to characterize the current event by some predefined trigger pattern (Tpat). For example, when the "spill-on" logic signal comes from the accelerator system in coincidence with a signal from POS and no signal from ROLU slits, it means that most likely there was an incoming ion which has reached the target. This trigger is then called "Good Beam". Requiring additionally signals from NTF, LAND or TFW, one can construct a Tpat indicating potential fragment, neutron or proton event, respectively. The Tpat "CB OR" is assigned when at least one crystal in the Crystal Ball has a signal above the threshold, indicating a potential γ-ray event. "CB SUM" is another Crystal Ball trigger intended for the high-energy proton hits. It requires an integrated analog sum of all signals in the detector to be higher then a certain threshold value.

The list of main on-spill triggers established for the present experiment is given in table 2.2. The off-spill triggers with Tpat>256 are not listed in this table, because they were mainly used for calibration of the detectors using cosmic muons as well as for measuring pedestals and for the time calibration purpose.

Tpat	Trigger name	Spill on	CB SUM	CB OR	TFW mul.	LAND	NTF mul.	POS. !ROLU
1	Good beam	X						X
2	Fragment NTF	X					X	X
4	CB OR	X		X			X	X
8	CB SUM	X	X				X	X
16	Proton TFW	X			X		X	X
128	Neutron	X				X	X	X

Table 2.2: The experimental on-spill triggers

[9] Strictly speaking, coincident within a certain time window.

Chapter 3

Calibrating the Setup

This chapter presents an overview of the calibration procedures as well as the results of these calibrations for particular detection systems. The first section describes briefly the general calibration approach, and the following sections explain in more detail the calibration of the Crystal Ball and the silicon trackers since these detectors are used for identification and measurement of QFS reactions. The calibration of other detectors is not highlighted in this thesis as it repeats the methodology which is commonly used in the experiments with the LAND-R^{3}B setup [30, 44, 49, 50].

3.1 The LAND02 Software and Common Calibration Steps

The primary experimental information is provided by the digitized analog signals (*e.g.* from an ADC or TDC) coming from individual detector channels. These observables are collected from all detectors during the experiment, processed and recorded by the Data AQuisition system (DAQ) [51] based on some trigger decisions. Before using the accumulated data for the actual analysis the detectors must be calibrated so that their signals can be interpreted in terms of physical quantities such as times, distances, energy losses etc.

The off-line calibration, which is used in the present work, utilizes the LAND02 software package developed mainly by H. Johansson and R. Plag for the LAND-R^{3}B setup [51, 52]. The code is based on gradual conversion of the initially digitized signals from the electronics ("RAW" level) into individual particle hits in the detectors and eventually to particle tracks ("HIT" and "TRACK" levels, respectively) as shown schematically in figure 3.1. A set of input parameters is determined on every calibration step using specific LAND02-utility programs. Applying these parameters to the current data level, the following level can be reconstructed. Additionally, the LAND02 software can output the data at each level in a user-specified format (*e.g.* ROOT file). Usually, the calibration of the detectors requires dedicated measurements, for example, using cosmic muons or a beam sweeping across the active area of the detector ("sweep run"). The calibration scheme, which is shown in figure 3.1, can be slightly different for some detectors (e.g SSD or DCH), but the general concept remains the same for almost all detectors.

A stability of the most important calibration parameters was monitored throughout the entire experiment as explained in [49] and [48]. Fluctuations of these parameters over time can be due to variation of the temperature in the electronics or in the detectors as well as due to electronics' noise or detector defects. When a parameter exceeds its maximum expected deviation, the current value of the parameter is accepted instead of its global (mean) value.

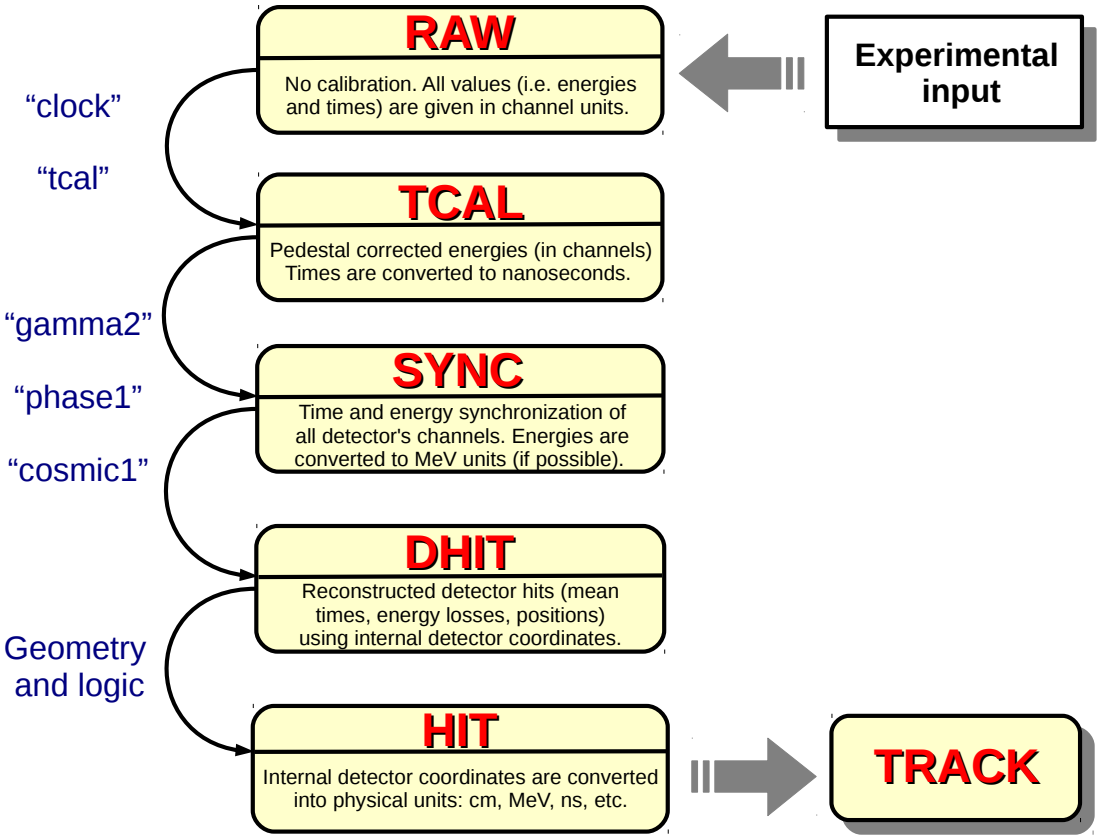

Figure 3.1: Structure of the LAND02 software. Different calibration levels are shown inside boxes together with a short description of the specific calibration steps. The corresponding LAND02-utility programs (blue font) are shown on the left side. In most of the cases, the transition from DHIT to HIT level requires essentially the knowledge of the detector/setup geometry.

3.2 Calibration of the Crystal Ball

3.2.1 Energy Calibration

γ-ray readout. In order to calibrate the γ-ray readout branch of the Crystal Ball, two radioactive sources have been used: a ^{22}Na source emitting two γ-rays with energies 511 keV and 1275 keV, and a ^{88}Y source with 898 keV and 1836 keV γ-rays. Each source was placed at the center of the Crystal Ball before and after the experiment and off-spill data was recorded. Typical energy spectra in a single crystal (after pedestal subtraction) are shown in figure 3.2. Mean value of each peak (in QDC channels) is determined from fitting a Gaussian function constructed on top of a linear background. The latter one is defined within the range of $\pm 3\sigma$ around the mean value. After the fit, the positions of all four peaks are plotted against their corresponding γ-ray energies and fitted with a linear function (figure 3.3a). The slope (gain) and the offset (zero energy in terms of QDC) of the fitted line is used to convert the measured energies from QDC channels into keV units:

$$E_{MeV} = E_{QDC} \times slope + offset. \tag{3.1}$$

From the Gaussian fits the corresponding peak widths (*i.e.* energy resolutions) are deter-

mined for every crystal. As expected, the widths behave like a square root function of the energy and vary between 20 keV and 60 keV for all crystals in the measured energy range.

The present calibration assumes a linear response also at higher energies, although with the used γ-ray sources this can be validated only up to the energy of about 2 MeV. Previous measurements with a PuC radioactive source have demonstrated that the linear behavior retains at least up to 6 MeV [44].

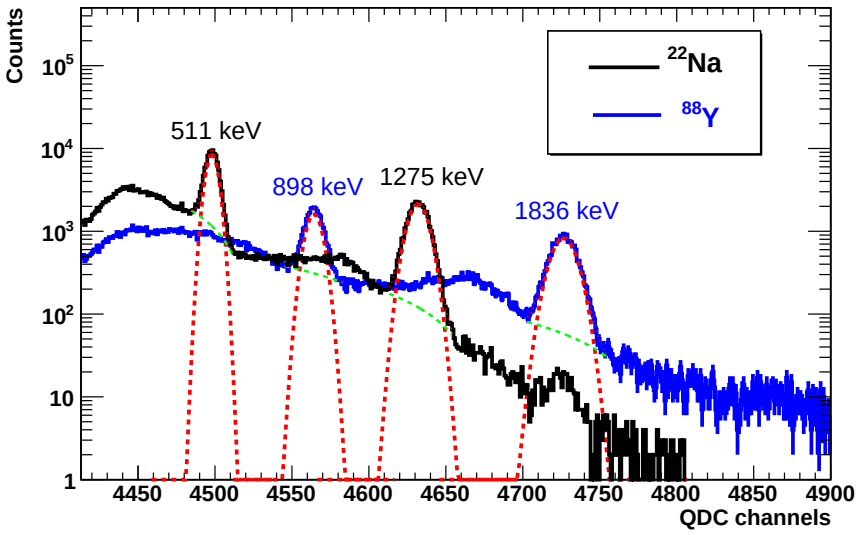

Figure 3.2: Typical γ-ray spectra from the ^{22}Na and ^{88}Y sources measured in crystal with a number 90. Each peak is fitted with a Gaussian plus a linear background determined within the range of $\pm 3\sigma$ of the peak. The mean values of the peaks were used for the linear fit giving the conversion factors from QDC channels into MeV units (see text).

Proton readout. An accurate calibration of the proton-readout branch turns out to be a difficult task, because it requires some source of particles, ideally protons, with known energies in the range from tens to hundreds MeV, emerging at various angles and covering the whole forward hemisphere of the Crystal Ball. In principle, the cosmic muons are suitable for this purpose, since they possess sufficiently high energies (up to a few GeV) and reach the surface of the Earth at different angles. Besides the rather well known angular and energy distributions of the cosmic muons one should also take into account the presence of all materials surrounding the detector such as concrete walls and ceiling of the experimental hall, metal support structures, etc. Therefore, an accurate simulation of the whole experimental hall and of the detector itself is necessary in order to estimate realistic energy losses of the cosmic muons in individual crystals. As a first step, a rough calibration of the proton readout branch is obtained from the energy correlation between γ-ray and proton readouts in every crystal. One can extract the correlation factor from simultaneous energy measurements of cosmic muons in both readouts (see figure 3.3b) and use it as a calibration parameter. Once this is done, one can find the gain in the proton readout by multiplying the gain in the corresponding γ-ray readout by the slope obtained from the correlation (*i.e.* by scaling the gains). In average, the gains in the proton readouts were 15 times smaller than the ones in the γ-ray readouts.

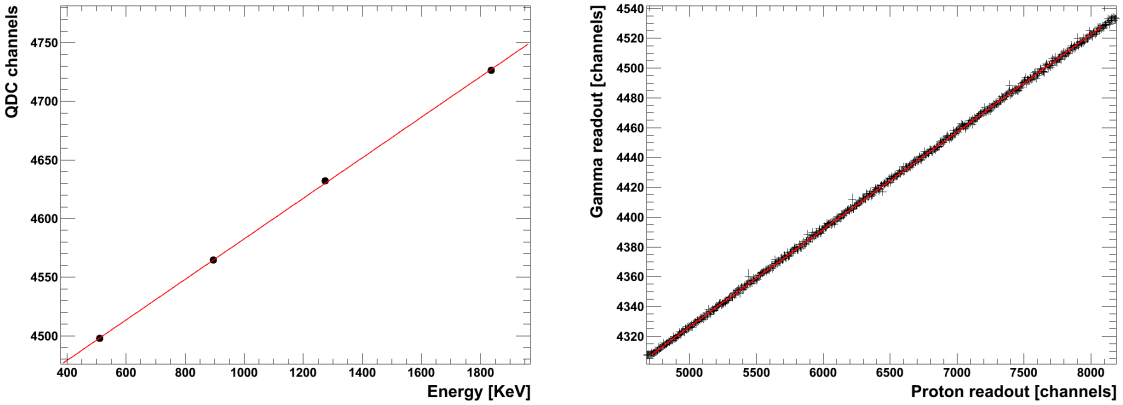

(a) Calibration of γ-ray readout branch

(b) Calibration of the proton readout branch

Figure 3.3: Linear regression of high-gain (γ-ray) and low-gain (proton) readouts for the crystal number 90. In figure (a) a linear fit is applied to the measured positions of the photopeaks plotted against the actual energies of the photons. The conversion (gain) factor from QDC channels to keV units is found from the the slope of the fitted line. In figure (b) the energy from the cosmic muons measured in the γ-ray readout is plotted against the same energy measured in the proton readout of the same crystal.

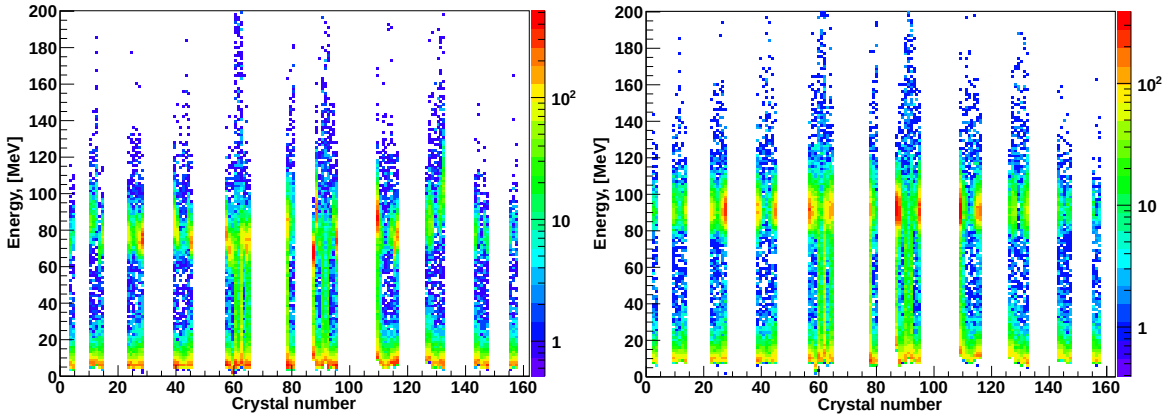

(a) Before cosmic muon calibration

(b) After cosmic muon calibration

Figure 3.4: Calibration of the proton readout branch using traversing cosmic muons. The figure shows the measured energy losses in 64 forward crystals against the crystals' numbers before (a) and after (b) correction. Mean values of the energy distributions in individual crystals are adjusted to a common value of 92 MeV that was obtained from GEANT3 simulation.

As a second step, a more detailed calibration is obtained using events where a single muon traverses the Crystal Ball centrally and hits only two opposing crystals. In this case the muon travels the maximum path inside the crystals and deposits sufficiently large amount of energy. The average energy loss of the cosmic muons in the crystals has been estimated via GEANT3 simulation under a somewhat naive assumption that all detected muons have

approximately the same energy of 2 GeV regardless of their incident angles. In general, the energy of the cosmic muons is a function of the incident angle, but, as mentioned before, a more detailed simulation is needed in order to take this into account. Nevertheless, in this approximation one can determine the mean energy loss of about 92 MeV for the traversing muons and adjust the individual gains in the proton readouts, so that the measured energies peak at the same value as shown in figure 3.4. The gain factors obtained in this way are used as additional calibration parameters to the ones obtained in the previous stage.

3.2.2 Time Calibration and Synchronization

Time measurements in the Crystal Ball can be extremely helpful for having a better selectivity of "good" photon-hits and for background reduction. In the present experiment it is realized via TDC (Time to Digital Converter) modules implemented in readout electronic chains. Performance of the modules was monitored throughout the full experiment in offspill mode using a signal from the time calibrator module, which was continuously generating pulses with known time delay. The necessity for using the calibrator is due to the fact that gains of the TDC channels can deviate during the experiment because of changes in the electronics' temperature or other effects. The signal from the time calibrator was sent in parallel to TDC channels from different parts of the setup and was used for the offline calibration and correction (when necessary) of the TDC gains.

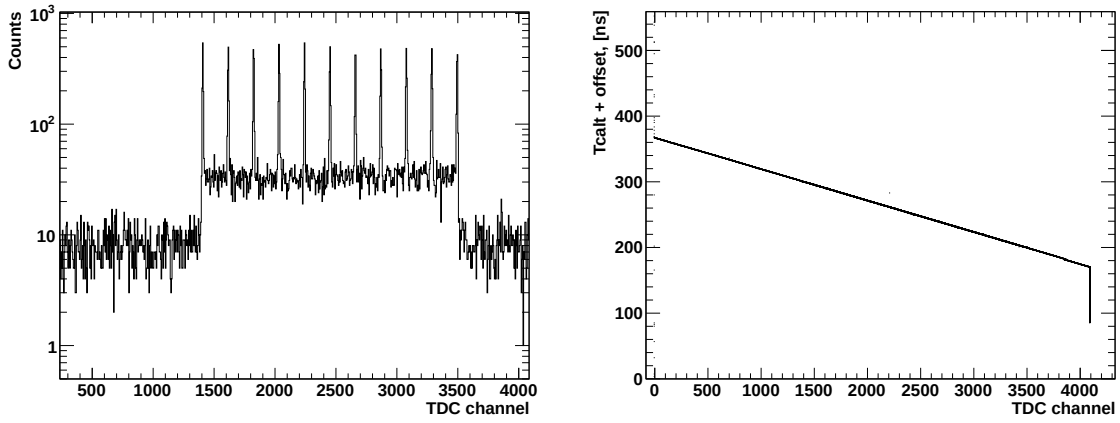

(a) time calibrator signal (Tcalt)

(b) time calibration graph

Figure 3.5: The time calibration of TDC channels. The left picture shows a typical signal of the time calibrator module. Eleven equidistant peaks with a step of 10 ns are used as a reference. The right picture shows the correlation between the signals in the TDC and the time calibrator signal. The slope of the correlation is used to convert channels to nanoseconds.

A typical signal form the time calibrator is shown in figure 3.5a. Eleven equidistant peaks with a step of 10 ns can be recognized as well as the region with low-statistics covering the entire channel range of the TDC. The conversion of channels into time units (*i.e.* nanoseconds) is found by plotting the time signals in the TDC against the calibration signal (figure 3.5b) and making a linear fit of the correlation.

Time synchronization. Besides the time calibration of individual crystals it is also necessary to synchronize them with each other. This is achieved with the aid of the "gamma2" utility program in LAND02. Data from the ^{88}Y γ-ray source run has been used to find coincident signals in pairs of crystals, originating from two γ-rays emitted from the source. It is assumed that both γ-rays arrive simultaneously, hence the time difference between each coincident pair must peak at zero. This fact is used to synchronize the two time signals by applying a relative time offset which is measured. All crystals were synchronized with respect to the crystal 52, which had the best timing characteristics. In figure 3.6 an example of the measured time difference between crystals 62 and 52 is shown after correcting for their relative offset (*i.e.* mean value is shifted to zero). For almost all crystal pairs the peak widths lie between 2.4 and 3.5 ns. Assuming an average width of 3 ns for all crystal pairs, one can find the average resolution of a single crystal to be $\sigma_t = 3/\sqrt{2} \approx 2.1$ ns.

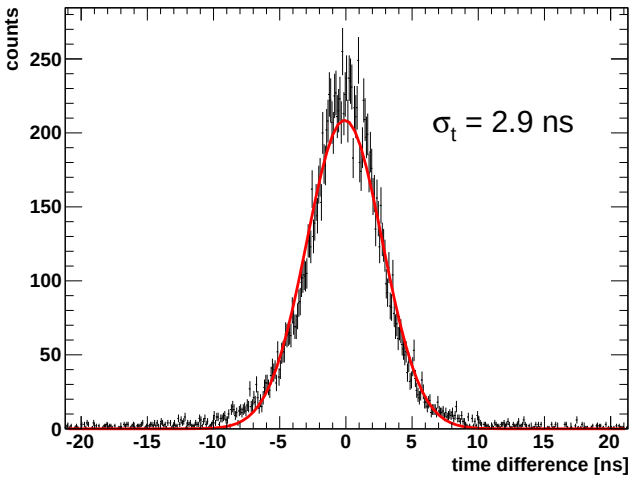

Figure 3.6: The result of the time synchronization of the crystal 62 with respect to the crystal 52. The width of the fitted Gaussian reflects the combined time resolution of both crystals.

It was found during the calibration that four crystals delivered no time signal and fifteen other crystals possessed rather bad time resolutions (double-hump shapes in the time spectra or very broad distributions). Hence, only 88% of all crystals could provide good timing. The crystals which produced bad time signals can be optionally excluded from the later analysis if good time measurements are needed.

When the crystals are synchronized with each other, a global time offset can be applied to the whole detector in order to synchronize it with the rest of of the experimental setup, for instance relative to the POS detector.

3.3 Calibration of the Silicon Trackers

There were in total six silicon microstrip detectors used in the present experiment. Two of them were situated in the beamline (in-beam SSDs) for tracking heavy fragments, and the other four were located around the target (box-SSDs) for measuring QFS protons. The presented calibration procedure, which is aimed to enhance the energy and the position resolution of the detectors, has been adopted from the original AMS work [41].

The calibration procedure consists of a few sequential steps. After each step the detector response is modified and used for the following manipulations. Due to peculiarities in the readout schemes and different charge carriers, the responses of K- and S-strips are also somewhat different and require separate sets of the calibration parameters.

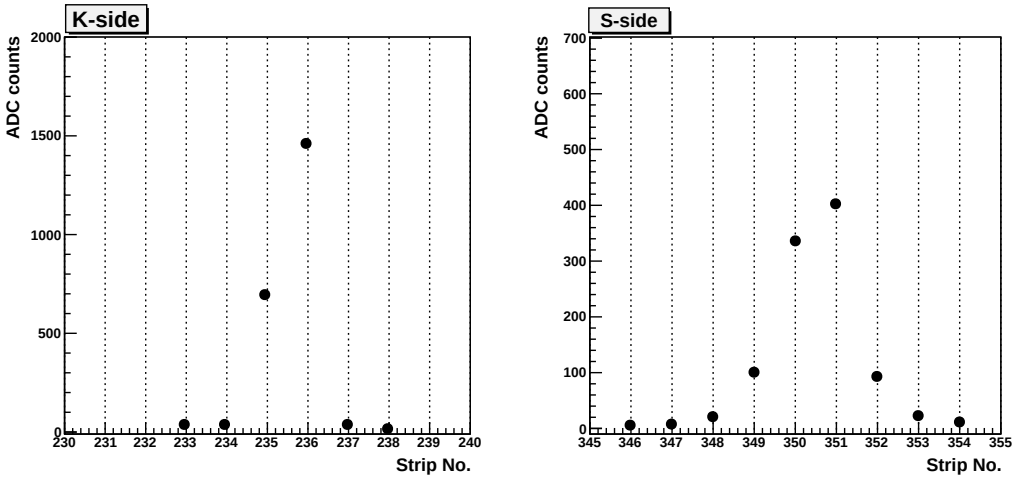

Figure 3.7: An example of a cluster of strips in K-side (left) and S-side (right) originating from a single carbon hit in the in-beam SSD.

In a general form the ADC signal from an individual read-out strip is given by:

$$S_{ADC} = \sigma_{ped} + \sigma_s + \sigma_{va} + S_p, \tag{3.2}$$

where σ_{ped} is a constant offset (pedestal), σ_s is the strip noise (sigma of the pedestal), σ_{va} is a coherent (common) noise component of the VA-chip and S_p is the useful signal stemming from the energy loss of the charged particle in the depleted silicon volume.

On the first calibration stage, the pedestals in individual strips are determined together with the corresponding standard deviations σ_s using the off-spill data. In the present measurements the average strip noise was around 2 and 4 ADC counts on the K- and S-side, respectively. The strips which are known to be "dead" (*i.e.* delivering no signal S_p) or which have abnormally large σ_s (noisy strips) are marked by setting their pedestals to negative values and excluded from the common noise calculation as well as from the following cluster reconstruction algorithm.

After the pedestal subtraction a coherent noise of a particular VA-chip is determined on the event-by-event basis as a mean ADC value over all 64 strips associated with this chip. Only those strips are accepted into the common noise determination, which have signals within $\pm 4\sigma_s$ in order to discriminate the presence of noisy strips and the strips fired by the ionizing particle.

Depending on the charge of the particle, its overall energy signal (*i.e.* the total collected charge) is distributed over a group of neighboring strips. The number of strips in one cluster (the so-called "cluster basewidth"), is not larger than three for a minimum ionizing particle like a proton, while for Z=6 particles it is in average 5.4 strips on the K-side and 8.3 strips on the S-side. A typical cluster from a single ^{12}C hit is shown in figure 3.7. Adjacent strips which have signals above $3\sigma_s$ are combined and stored in a preliminary cluster structure (SYNC level), which is used later for the energy and position reconstruction of the particle hit.

The position information can be obtained from the signal-weighted center-of-gravity (CoG) of the cluster:

$$CoG = \frac{\sum_{i=a}^{b} S_i N_i}{\sum_{i=a}^{b} S_i}, \tag{3.3}$$

where a and b denote the first and the last strip of the cluster, S_i is a signal in individual i-th strip (after pedestal and noise correction) and N_i is the corresponding strip number. In this definition the CoG is expressed in terms of strip numbers, and the summation is done over all strips contributing into the cluster. The hit position is then calculated as:

$$X_{CoG} = p \times CoG, \tag{3.4}$$

where p is the readout pitch size that is 104 μm and 110 μm on K- and S-side, respectively.

3.3.1 Energy Correction in In-Beam SSDs

The total energy loss of a penetrating ion is reconstructed via summation of the signals in all strips forming a cluster ("cluster sum" or "cluster area"):

$$E = \sum_{i=a}^{b} S_i. \tag{3.5}$$

Due to the presence of floating strips in the readout gap and spacing between the strips, the reconstructed cluster sum is influenced by a relative position of the hit with respect to the nearest readout strip. This dependence can be expressed through the impact parameter η, which characterizes the interstrip position of the hit:

$$\eta = \{CoG - int(CoG)\} \in [0; 1], \tag{3.6}$$

where $int(CoG)$ is an integer part of the CoG, that is essentially the number of the central strip of the cluster. When $\eta \approx 0$, it means that the hit is exactly in the center of the readout strip and $\eta \approx 1$ means the hit is in the center of the next readout strip (similarly η=0.5 stands for the hit which is exactly inbetween two readout strips).

Figures 3.8 (a) and (b) show how the cluster area depends on the reconstructed hit position. Such behavior decreases the overall energy resolution and must be corrected. Due to different implantation schemes, the cluster sums in K- and S-side behave differently with respect to the impact parameter. The η-effect is also sensitive to the energy loss (*i.e.* charge) of the passing ion. However, if the charges do not differ too much, *i.e.* by one or two units, their η-effects are quite similar. Additionally to the η-correction, the resulting cluster sums for ^{12}C hits in K- and S-side are adjusted (gain-matched) to a common value of 1000 a.u., to correct for different gains of the VA-chips. In order to calibrate full active areas of the in-beam SSDs, a defocused ^{12}C beam was used which almost entirely illuminated the surfaces of both detectors. The results of the eta-correction and the gain-matching are shown in figures 3.8 (c) and (d).

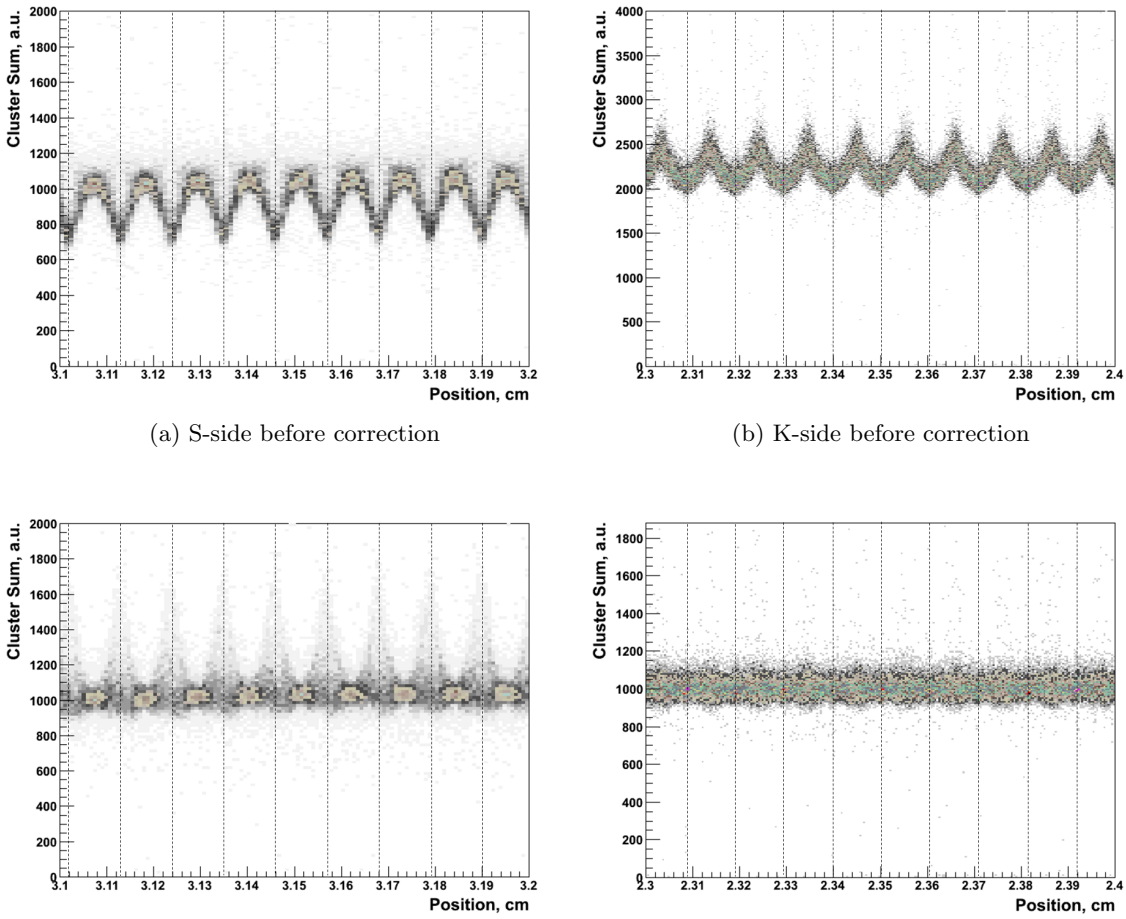

(a) S-side before correction

(b) K-side before correction

(c) S-side after correction

(d) K-side after correction

Figure 3.8: Position dependence of the cluster sums corresponding to ^{12}C hits in K- and S-side of SSD3 (upstream detector) before and after η-correction. Each dashed line is a middle of a readout strip. The influence of the interstrip impact parameter η on the cluster sum results in a regular pattern across the readout gap. This pattern is identified and corrected accordingly.

3.3.2 Position Correction

The above formulation assumes a homogeneous η-distribution *i.e.* no dependence of the reconstructed hit position on its inter-readout-strip distance. However, the effect of non-linear charge collection as a function of the η-parameter results in distinct enhancements in the position distribution which are correlated with the strip structure of a sensor.

This effect can be corrected using the integrated value of the η-distribution function f(η) as a correction factor for the reconstructed hit position as has been proposed in [41]. Thus, the corrected position can be determined as follows:

$$X_\eta = X_1 + p \int_0^\eta f(\eta) \mathrm{d}\eta, \tag{3.7}$$

where X_1 is the position of the central strip in a cluster (an integer part of the CoG), p is

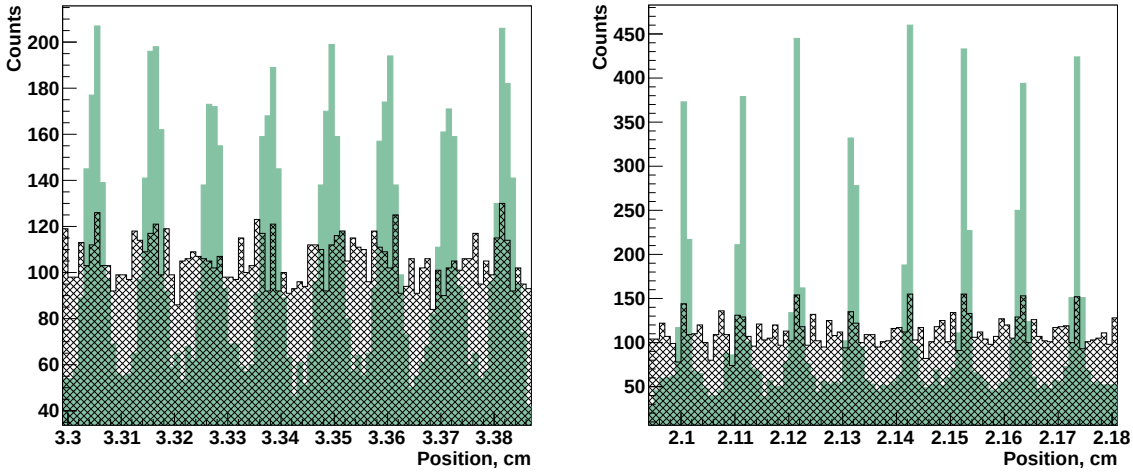

(a) S-side (b) K-side

Figure 3.9: Eta-position correction in SSD4. The non-corrected position distribution (green) correlates with the strips structure of the sensor and shows an inhomogeneous response with respect to the interstrip impact parameter η. The corrected positions (black) are uniformly distributed across the readout gaps.

the readout strip pitch, and $f(\eta)$ is the normalized η distribution. As mentioned before, the effect of η-dependence varies for different charges, so that the present correction is only valid for charges in the vicinity of Z=6. For other particles the position resolution is determined roughly by the readout pitch size.

3.3.3 Correcting dead strips

A strip which does not deliver any signal (as seen after pedestal/noise subtraction) or whose signal is systematically too low is defined as "dead" strip. A reason for that might be a broken bonding to the VA-chip or some other physical damage. In any case, the presence of dead strips has to be taken into account when searching for clusters of strips, because such defects can be falsely interpreted by the reconstruction algorithm as the cluster edges, which results in splitting into two or more separate clusters. To avoid this problem, the dead strips are marked and excluded from the cluster finding algorithm. If the dead strip appears to be a central strip or a neighbor of the central strip, the cluster sum is additionally corrected by adding the mean ADC value of the left and right neighbors scaled by a factor proportional to the corresponding η-parameter. If a dead strip is at the cluster edge, the cluster sum is not influenced and doesn't need to be corrected. An illustration of the dead-strip correction is shown in figure 3.10.

3.3.4 Efficiencies and Charge Selection

After the final corrections, the information about the charge and position of the detected particle can be obtained. The charge identification in both in-beam detectors is shown in figure 3.11. The measured energies are not identical in K- and S-side due to different energy responses. The energy correlation in both sides can be used, if necessary, to identify the

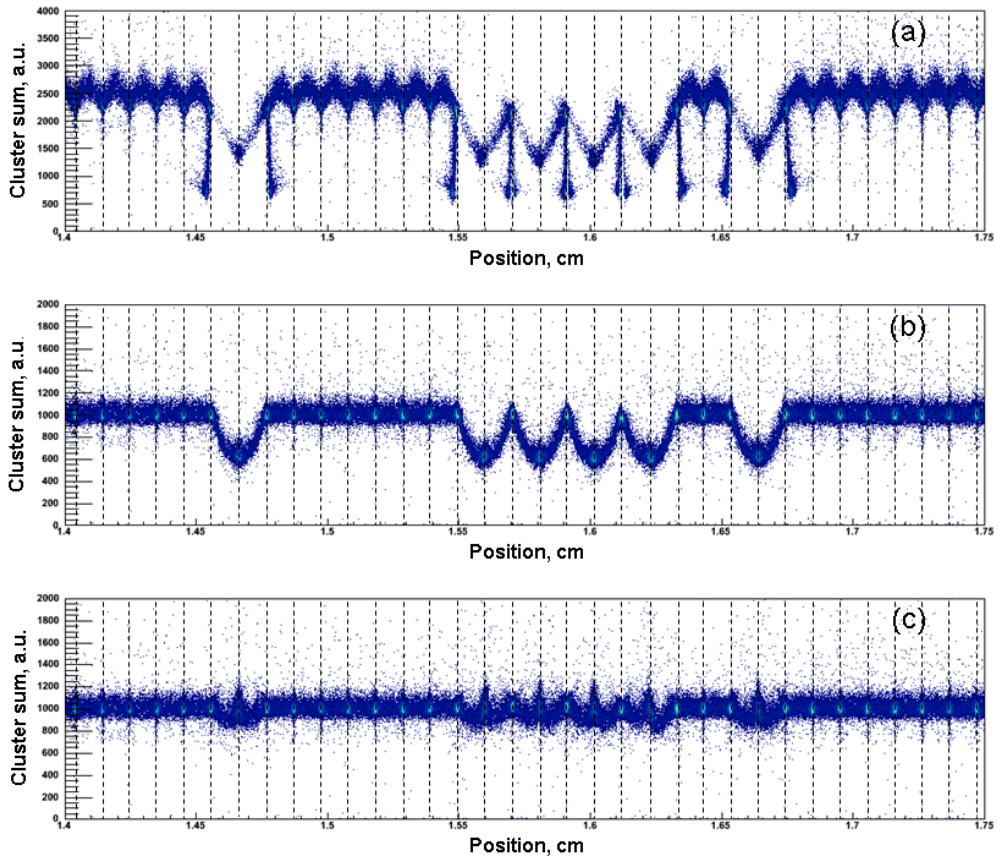

Figure 3.10: An example of the dead-strip correction on the K-side of SSD3. Figure (a) shows non-corrected data; the dead strips tend to split original clusters, which leads to the wrong CoG and cluster sum reconstruction. Figure (b) shows the first step of the correction, in which the dead strips are marked and excluded from the cluster finding algorithm. Although the positions are correctly reconstructed, the total collected charge (cluster sum) is underestimated in the vicinity of a dead strip. The final correction is shown in (c), where the cluster sum is corrected as a function of the η-parameter.

charge of a particle via 2D graphical cut. The obtained energy resolution in the K-side is somewhat better than the one in the S-side due to a lower saturation threshold. This fact implies that the K-side is more preferable choice for outgoing charge identification, although, in principle, different combinations of the energy cuts in both sides can be used as well.

To estimate the detection efficiency of the in-beam SSDs, data from a non-reacted ^{12}C beam was used. The number of ^{12}C detected in the time-of-flight wall behind the magnet was compared with the corresponding number of Z=6 hits in each in-beam SSD using measurements in the K-side. Depending on the chosen energy cuts, the efficiency varied by a few percent, but always exceeded 95% for both in-beam detectors.

3.3.5 Proton Response in SSDs

Fast protons are minimum ionizing particles and their energy losses in SSDs are close to the noise level of individual strips and to the energy of secondary δ-electrons. A proton response in the upstream SSD is shown in figure 3.12. It agrees well with previous measurements [43].

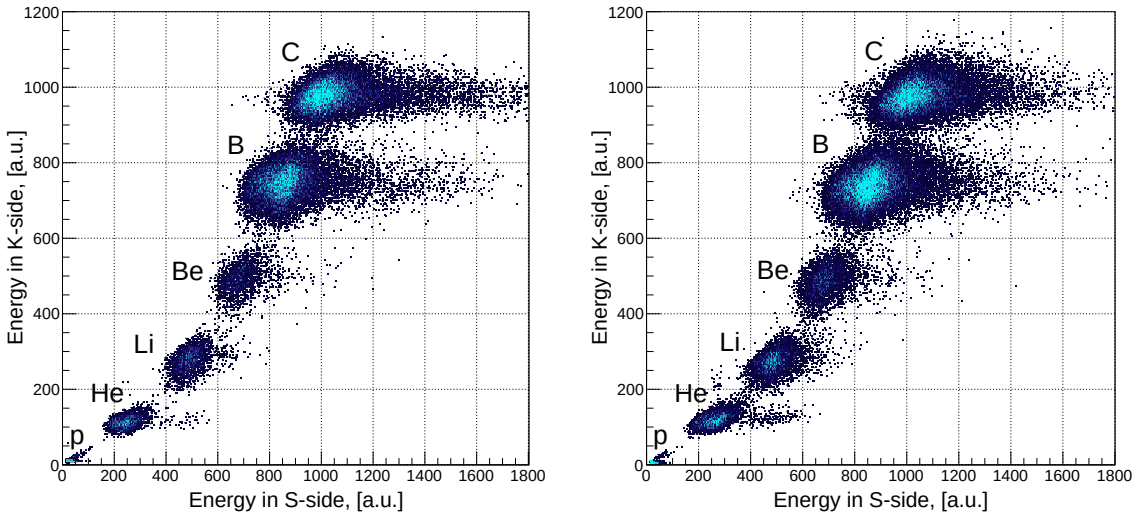

(a) SSD3 (upstream)

(b) SSD4 (downstream)

Figure 3.11: Outgoing-charge identification in two in-beam SSDs. Non-linearity in the responses of K- and S-side is observed. The energy losses in both sides were adjusted so that in each one the energies from Z=6 hits peak at 1000 a.u.

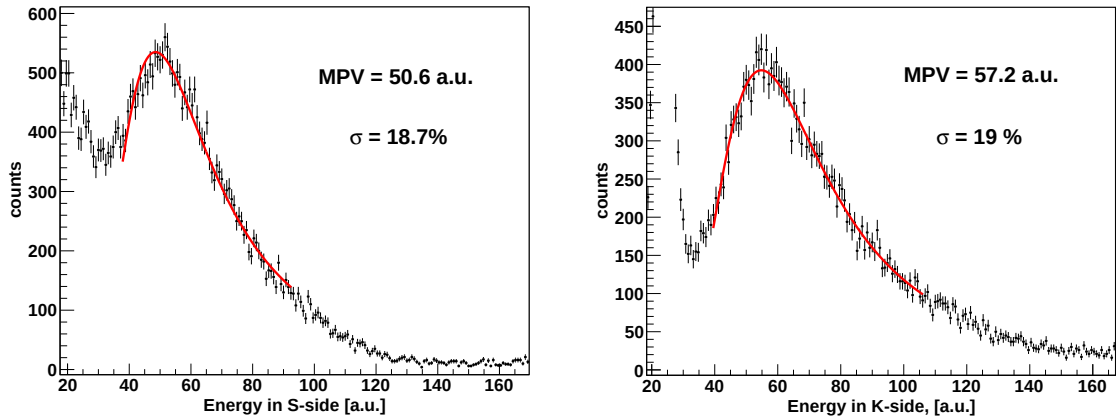

Figure 3.12: Proton response in the first in-beam SSD in coincidence with a signal in the proton ToF-wall (TFW). The inset numbers represent the most probable values (MPV) and the widths of the peaks obtained from the Landau distribution fits. The hits with energies below 40 a.u. are interpreted as noise (*e.g.* due to secondary electrons). Since the protons in the in-beam SSDs originate mainly from the breakup of heavy fragments, their energies remain approximately equal to the beam energy (*i.e.* 400 MeV per unit mass).

The calibration of the box-SSDs, which are not directly hit by the beam, turns out to be difficult since it requires incident protons, which in turn can emerge only from the reactions in the target. Another complication is a large energy variation of the scattered protons from the QFS reactions. The energy of such protons is generally a function of the angle relative to the beam and can vary from a few MeV for the angles close to 90° up to several hundreds

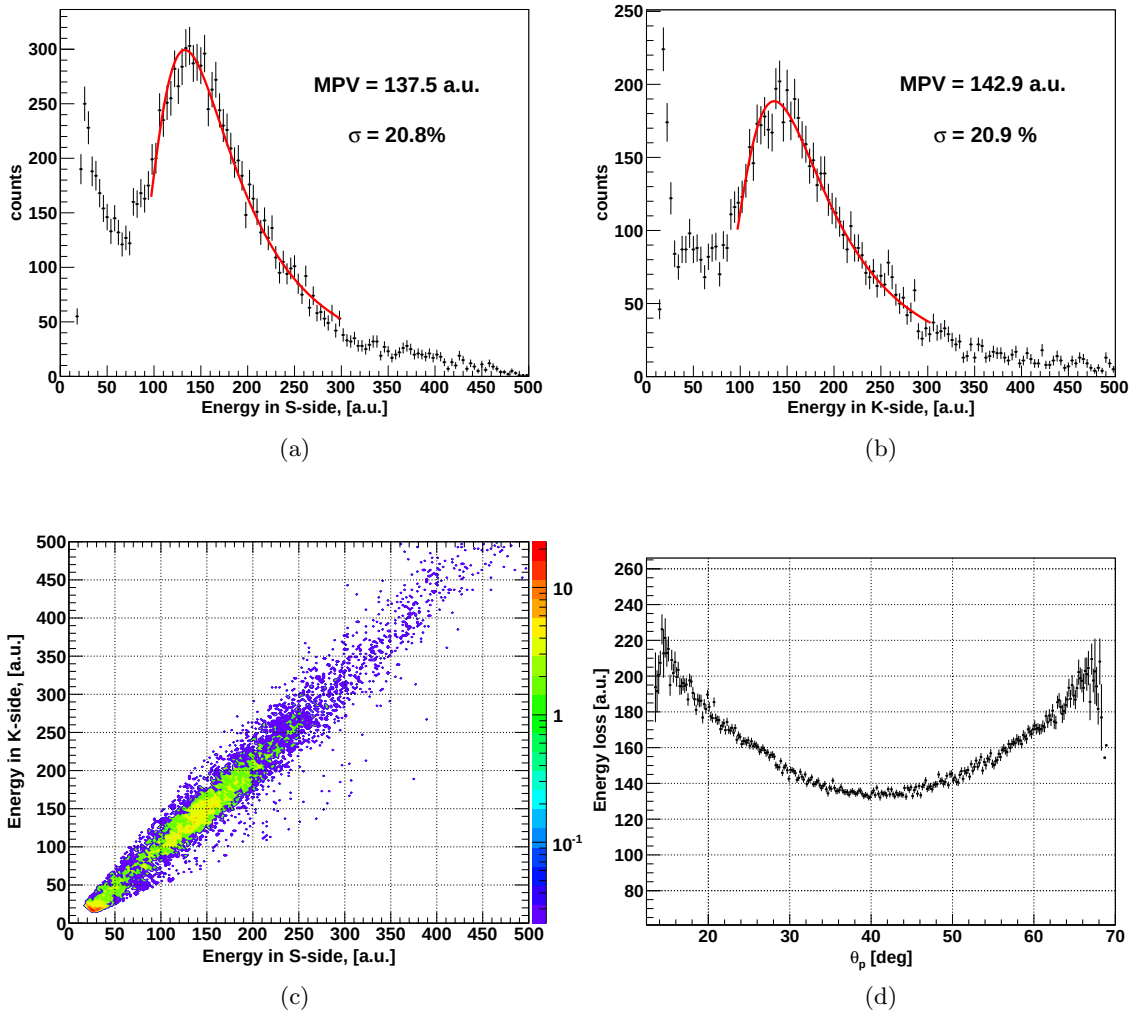

Figure 3.13: Proton response in SSD5 (box, top) is measured in coincidence with high-energy hits in the Crystal Ball. Energy spectra in S- and K-side are shown in (a) and (b), respectively. Based on this, a minimum threshold of 50 a.u. is applied to cut the noise. Correlated energies in S- and K-side on figure (c) are used to find matching hits. Figure (d) shows the dependence of the average energy loss (an arithmetic mean of S- and K-energy) on the corresponding proton polar angle (see explanation in text).

MeV at smaller angles. Additionally, the protons traverse the box-SSDs at different angles relative to their surfaces. This changes a flight path in the active volume as well as the energy which is deposited on the way. Applying the add-back algorithm to the Crystal Ball and requiring additionally ^{11}B fragment in the outgoing channel, one is able to identify two proton hits in the calorimeter and to find coincident hits in the box-SSDs (see section 4.2). A typical energy response for such protons in a single SSD is shown in figure 3.13. Figure 3.13d illustrates how the average energy losses in the SSD depend on the protons' angles relative to the beam axis. Small angles correspond to longer flight paths inside the silicon bulk, however, such protons are in average more energetic and deposit less energy, while at larger angles the protons are slower but travel shorter distances inside the detector. All these effects result in a complex proton-response function of the box-SSDs that depends simultaneously on the

initial angle and energy of a proton. The minimum energy deposition of about 140 a.u. is observed around the angle $\theta_p = 40°$, where the most of QFS protons are expected to emerge. This energy is almost three times greater compared to the MPV for the breakup protons which are measured in the in-beam SSDs (compare with figure 3.12).

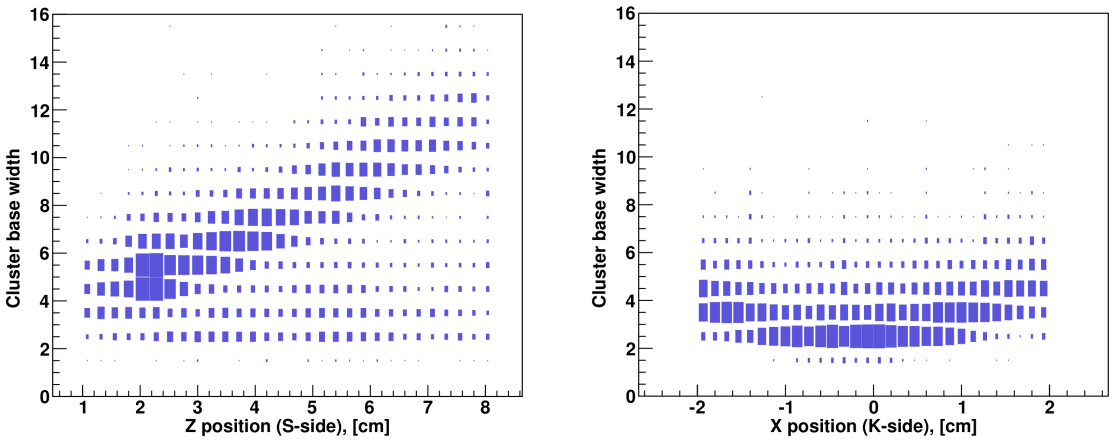

(a) S-side (b) K-side

Figure 3.14: Observed dependences of the cluster basewidths on the coordinates of proton hits relative to the target center (in top-SSD). The number of strips in a cluster changes as a function of an incident angle relative to the surface of the detector.

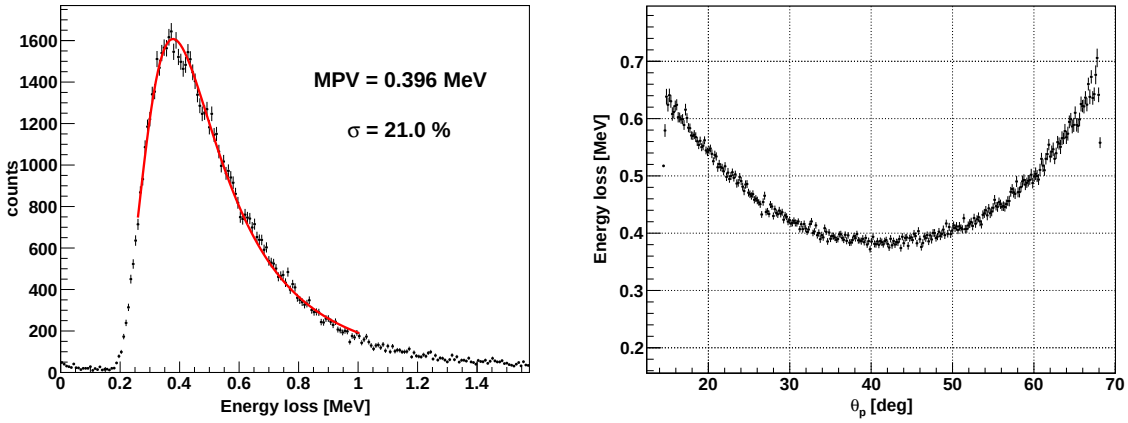

(a) Energy losses (b) Energy vs. proton polar angle

Figure 3.15: Simulated proton response in SSD5 (box, top). Figure (a) shows the energy-loss spectrum for the QFS protons. The resolution of 21% matches with the experimental resolutions for the K- and S-side. Also, a similar behavior of the average energy loss as a function of the proton angle is observed in the experiment (compare with figure 3.13d).

Different flight paths in the detectors are reflected in a number of strips (cluster basewidth) fired by a penetrating proton as a function of the impact position as shown in figure 3.14. The average size of a cluster in S-side can reach 12 strips, while in average only 2-3 strips are expected for the protons, which traverse almost perpendicularly to the surfaces of the

detectors (*i.e.* in in-beam SSDs).

Hence, the corrections regarding the interstrip parameter η, which are described in previous sections, could not be applied for the box-SSDs, because the η-effect is in rather complex relation with angles and energies of the protons. Only pedestal subtraction, common noise corrections and dead-strip elimination were used for calibrating the box-SSDs. The position resolution for the QFS protons is therefore roughly determined by the size of the readout-pitch, *i.e.* 104 μm (K-side) along X- and Y-axis and 110 μm (S-side) along Z-axis.

The observed energy-loss distributions in the box-SSDs are in a good agreement with the GEANT4-based simulation, which uses realistic kinematics of the $(p, 2p)$ reaction and the actual experimental geometry of the box-SSDs (see Appendix). The results of the simulation are shown in figure 3.15. The most probable value of 396 KeV with the resolution $\sigma = 21\%$ was found from the Landau distribution fit of the simulated spectrum (compare it with figures 3.13a and 3.13b).

Chapter 4

Analysis and results

4.1 Identification of Outgoing Fragments

A charged particle which travels with the velocity β inside a magnetic field with the strength B is affected by the Lorentz force. Assuming countervailing centrifugal and Lorentz forces along the curved particle trajectory, one can derive the following equation:

$$\frac{m_u c}{e}\frac{A}{Z}\beta\gamma = B\rho, \tag{4.1}$$

where m_u is the unit mass, c is the speed of light, e is the charge unit, A and Z are the charge and mass numbers of the particle, β and γ are the speed and the Lorentz factor, ρ is the curvature radius of the trajectory. As one can see, for a fixed velocity β the $B\rho$ product is proportional to the mass-over-charge (A/Z) ratio of a given particle. This principle is used for the identification of the reaction fragments behind the ALADIN magnet. A dedicated tracking algorithm developed by Ralf Plag [52] has been used for this purpose. The algorithm is based on the reconstruction of the trajectories starting from the NTF detector through the magnetic field towards the silicon trackers. In this way the masses, velocities and total three-momenta of the fragments can be calculated. This routine has been successfully used in the analysis of previous experiments performed at the LAND-R^{3}B setup (see for example [44]). As a necessary input, the tracking program utilizes absolute positions of the detectors in the laboratory system and known magnetic field map of ALADIN, which was previously measured throughout the entire volume of the magnet [53] and can be scaled according to the applied value of electric current in the magnet. In addition to this, one needs to specify the charge of the fragment being tracked that is achieved via redundant charge measurements in the NTF and in the in-beam SSD directly after the target (see figure 4.1).

Using position measurements in the tracking detectors and the initial value of β (from the incoming beam) as starting parameters, the tracking program calculates trajectories through the magnet. After that, Δx and Δy offsets of Si-trackers are calculated and the mass A is varied as well as the velocity β to match the measured and the calculated time-of-flight values between NTF and POS. The operation is repeated iteratively until the SSD offsets become smaller or equal to required values. In a similar way, tracks of protons are reconstructed, using position and time-of-flight measurements in the proton arm.

The resulting mass distribution under the condition to have two high-energy hits in the Crystal Ball is shown in figure 4.2. The mass identification in combination with the charge measurements allows for an accurate identification of the reaction products (figure 4.3).

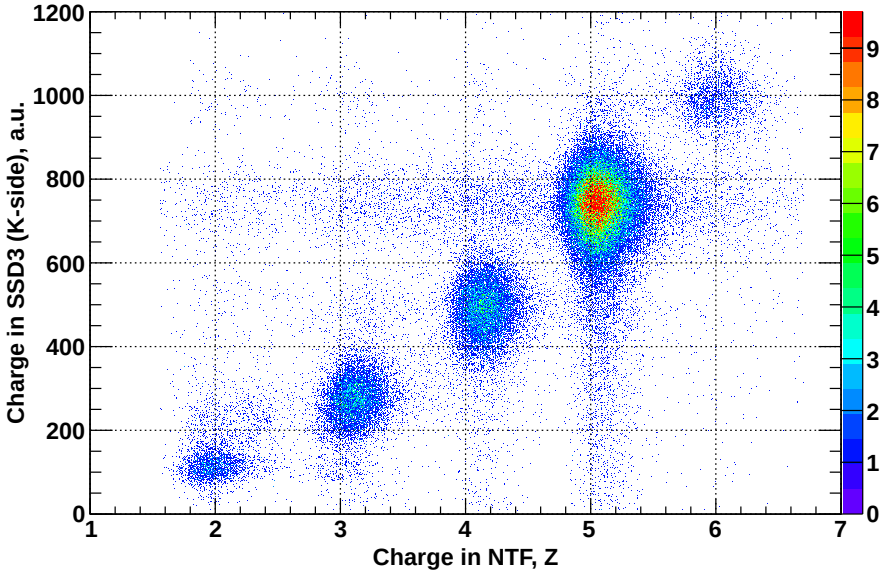

Figure 4.1: Charge identification of outgoing fragments in the upstream SSD directly after the CH_2 target and in the NTF behind the magnet. Not more than one hit in NTF has been required in coincidence with a high-energy signal in the Crystal Ball.

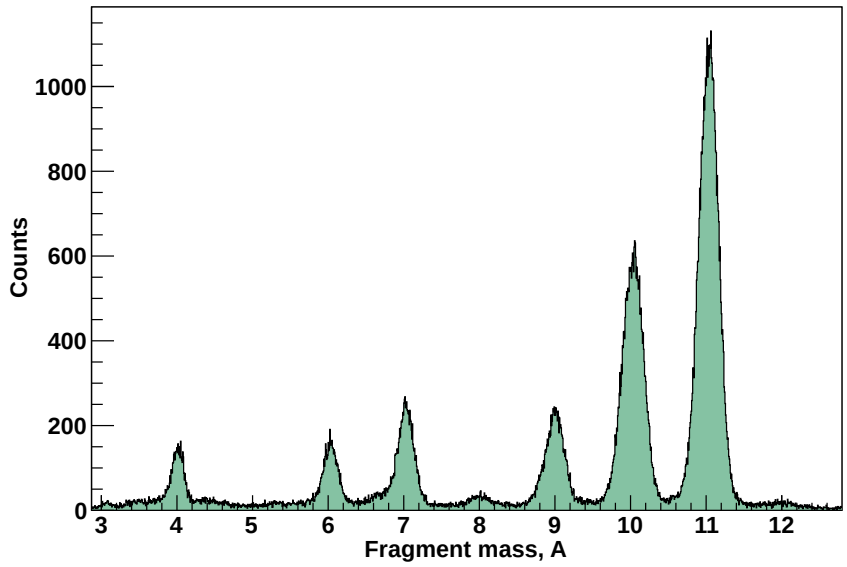

Figure 4.2: Mass-spectrum of all outgoing fragments measured with the CH_2 target in coincidence with two potential proton hits in the Crystal Ball. The resolution varies between 1.2% and 2.3% for the mass peaks at A=11 and A=4, respectively.

It should be noted, that in the present measurements the GFI detectors lack multihit capability. Therefore, it is possible to track only one fragment at a time, *i.e.* when there are two or more particles in the fragment arm, the tracker reconstructs them as one track.

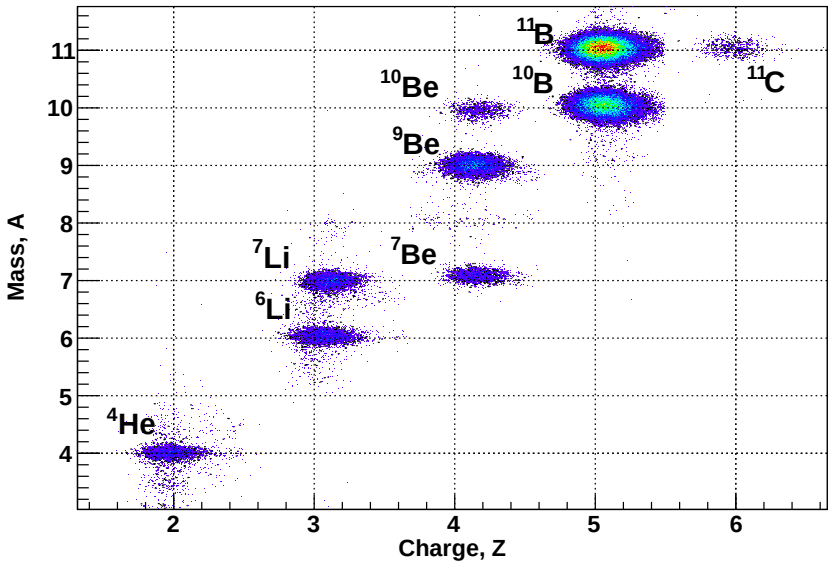

Figure 4.3: Mass and charge identification of outgoing fragments reconstructed via the tracking program in coincidence with two high-energy hits in the Crystal Ball.

4.2 QFS Protons

A crucial part of the present analysis is based on the identification and measurements of energetic pairs of nucleons emerging in QFS reactions of a type $^{12}\mathrm{C}(p,2p)^{11}\mathrm{B}$ and $^{12}\mathrm{C}(p,pn)^{11}\mathrm{C}$. The particles have been measured in a broad angular range with the aid of the Crystal Ball detector and the four SSDs surrounding the target (box-SSDs). The following sections describe the analysis steps aimed at the reconstruction of the $(p,2p)$ reactions, and the (p,pn) channel is discussed in section 4.6.

4.2.1 The Add-Back Algorithm

When an energetic particle (*e.g.* proton or photon) hits a crystal in the Crystal Ball, some part of its deposited energy in form of secondary electrons, positrons, gammas, etc. can spread to surrounding crystals. Alternatively, the particle itself can re-scatter and transit through a chain of crystals. Hence, the total energy loss of the particle can be found by summing up individual energies measured by a group of adjacent crystals, which is also called a "cluster". This is particularly relevant for proton hits, in which larger amount of energy is released compared to γ-rays, and it is very likely to trigger more than one crystal. On the other hand, it is necessary to separate crystals which belong to proton clusters[1] from ones which belong to γ-ray clusters, since both types of particles can emerge from the same QFS reaction.

In order to identify clusters of crystals and to find the total deposited energy in each particle hit, the so-called "add-back algorithm" was applied event by event. A few assumptions are made regarding the add-back. Firstly, one assumes that the central crystal in a cluster (*i.e.* the one which was hit first) should receive the biggest part of the total deposited energy

[1]Strictly speaking, high-energy signals are not necessarily caused by protons. They can be due to other particles like energetic photons, neutrons, deuterons, alphas etc. For simplicity, a cluster with a high energy will be further called "proton cluster".

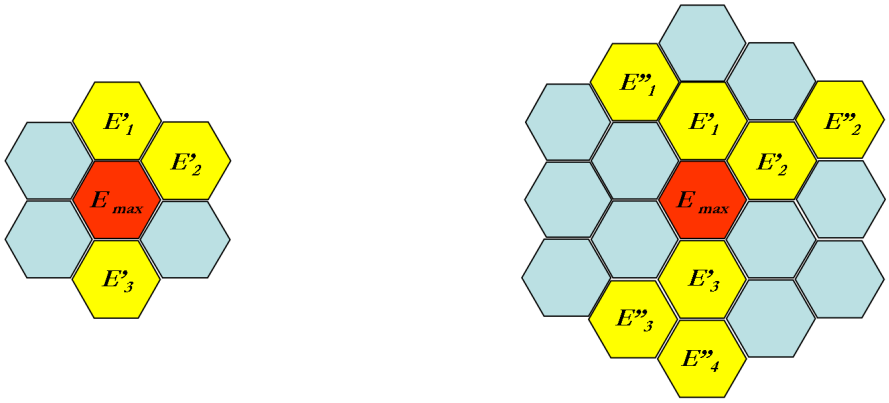

(a) Simple add-back (b) Improved add-back

Figure 4.4: Schematic view of different add-back algorithms. In the simplest case (a) the maximum cluster size is limited by the number of closest neighbors surrounding the central crystal with the highest energy (red); the total energy of the cluster is $E_{tot} = E_{max} + \sum_i E'_i$ (crystals with secondary hits are shown in yellow). The improved algorithm expands to the second-ring crystals (b), to account for the case when a chain of crystals gets energy from one particle hit; the total deposited energy is determined as $E_{tot} = E_{max} + \sum_i E'_i + \sum_j E''_j$. The following condition is required for crystals which can be accepted into such "expanded" cluster: $E_{max} > E'_i > E''_j$.

compared to the neighbors, so that an assignment of the cluster type (*i.e.* caused by photon or by proton) can be made judging from the energy in this crystal. Another assumption is that, if the energy in a γ-readout is less than 25 MeV (the limit of a QDC range in the γ-readouts), the hit is considered to be a photon. Otherwise, when the γ-ray energy is in overflow and the energy in the proton readout is larger than 25 MeV [2] the hit is considered as a proton event. Hence, the add-back algorithm performs the following steps:

1. All crystals, which have meaningful energy in γ-ray or in proton readouts and meaningful times, are added into a global list. Only those crystals are accepted which have energies above 400 keV.

2. The crystals in the global list get sorted from higher to lower energies, so that a crystal with a highest energy is always on the first position, and the one with smallest energy is on the last position.

3. The sorted global list is analyzed starting from the very first crystal, which is by definition a central one in some cluster. The type of this crystal/cluster is determined (*i.e.* proton or γ-ray), and the crystal is added to the corresponding list of clusters. The algorithm continues looking for the neighbors of this crystal in the global list until it reaches the end. Every time, when a new neighboring crystal is found, its energy is added to the total energy of the cluster, and the crystal is removed from the global list.

4. After the first iteration the procedure is repeated for the crystal on the second position in the reduced global list and so on until the last element. In parallel with this the identified clusters are stored into separate containers for gammas and for protons.

[2] Only for crystals in the forward hemisphere.

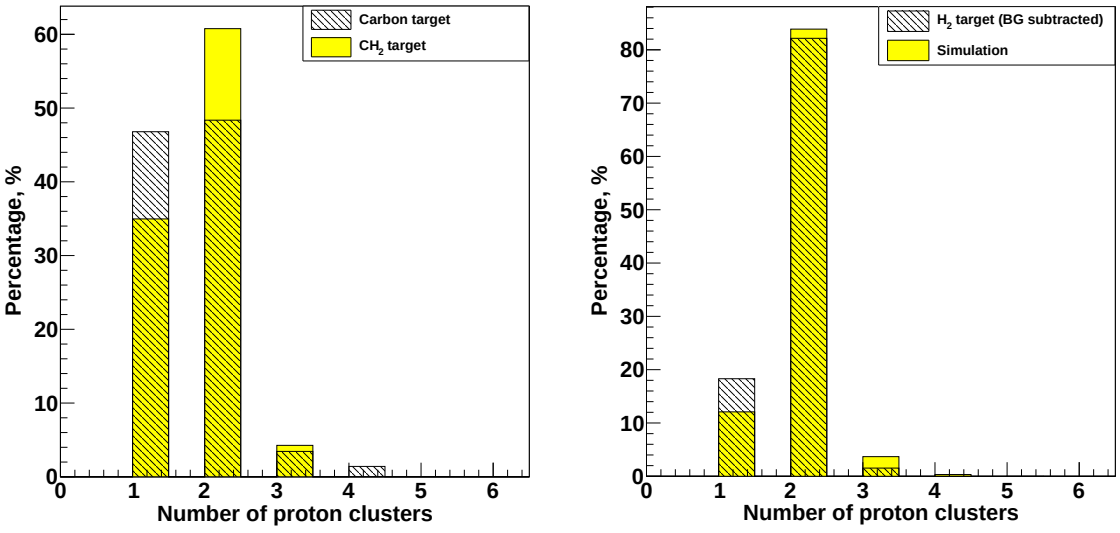

(a) (b)

Figure 4.5: Normalized multiplicity distributions of high-energy clusters in the Crystal Ball are obtained under condition to find at least one crystal with a high energy in the forward hemisphere of the Crystal Ball and ^{11}B in the outgoing channel. Comparing the measurements for the CH_2 and the carbon target (a), one can see enhanced multiplicity of two for the CH_2, which can be attributed to the QFS reactions induced by the hydrogen component. In figure (b) the multiplicity for the H_2 target (carbon-background subtracted) is compared with the simulated detector response.

The described above algorithm accounts for only closest neighbors of a central crystal (maximum 7 crystals in one cluster). It might happen though, that in one hit the deposited energy is distributed over a chain of crystals. In such case the algorithm can be improved in a way to account for the energies in the second ring of crystals and even further. To avoid overlapping clusters, the algorithm has been limited to the "second order" neighbors as explained in figure 4.4.

High-energy hits in the backward hemisphere of the CB can also be taken into account. Such hits can originate, for instance, in knockout reactions with short-range-correlated nucleon pairs inside ^{12}C or from resctattering of energetic particles in the forward hemisphere, or simply due to cosmic muons. Although energy measurement via proton-readout branch is not possible in this case, still such hits can be identified during the add-back procedure by requiring the γ-energy branch of a central crystal to be in overflow (*i.e.* above 25 MeV energy).

The cluster multiplicity distributions measured with the CH_2 and carbon targets are presented in figure 4.5a. Enhanced multiplicity of two for the CH_2 target indicates the presence of QFS reactions induced by the hydrogen constituent.

The normalized distribution of cluster multiplicities for the CH_2 data after subtracting the carbon background (*i.e.* for the H_2 target) is shown in figure 4.5b. It is compared with the expected detector response, which has been obtained through the R3BROOT simulation (see Appendix) using the same type of "improved" add-back algorithm. The agreement between the measured and simulated responses is quite good for the multiplicity of two. However, the

multiplicity of one is somewhat underestimated in the simulation, that is probably due to not very accurate measurements of low proton energies close to 25 MeV threshold and other imperfections of the simulation, *e.g.* lacking aluminum casing of the crystals and some other materials in the target chamber. In the following discussion the condition to have exactly two high-energy clusters in the Crystal Ball will be implied.

4.2.2 Angular Distributions of QFS Protons

Due to the pronounced radial symmetry of the QFS reaction, it is convenient to represent laboratory measurements using the spherical coordinate system, where the inclination θ (or polar angle) of a particle is defined with respect to the beam (Z-axis): $\theta \in [0; \pi]$; and the azimuth angle $\varphi \in [0; 2\pi]$ is defined relative to the X-axis as shown in figure 4.6.

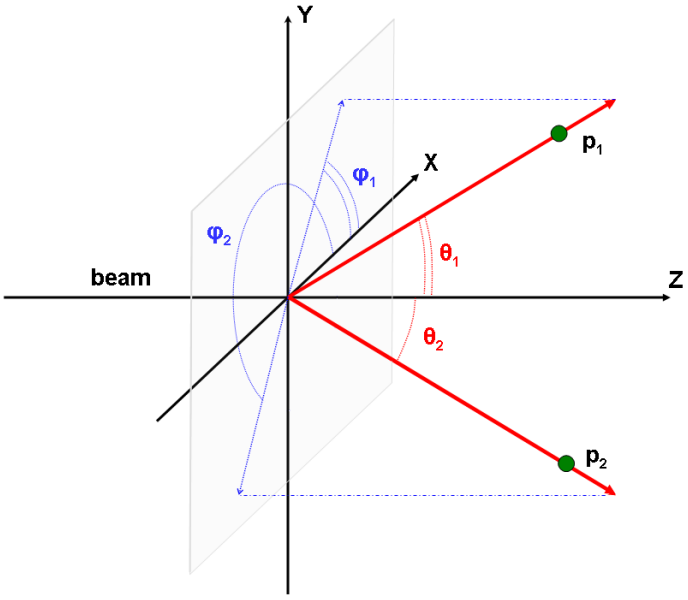

Figure 4.6: The measured laboratory angles of an outgoing proton pair from the $(p, 2p)$ reaction. Spherical coordinate system is chosen such that the polar direction is associated with the beam axis Z.

From the scalar product of two vectors $\vec{p_1}(\theta_1, \varphi_1)$ and $\vec{p_2}(\theta_2, \varphi_2)$ in the spherical system, one can derive the following expression for the opening angle θ_{op} between the vectors:

$$\alpha_{op} = \sin\theta_1 \sin\theta_2 \cos(\varphi_2 - \varphi_1) + \cos\theta_1 \cos\theta_2. \tag{4.2}$$

A qualitative picture of the free proton-proton scattering at non-relativistic energies (*i.e.* when both protons are unbound and $\beta \to 0$) assumes that the recoil protons comply with the coplanar reaction kinematics (*i.e.* $\Delta\varphi = (\varphi_2 - \varphi_1) \approx 180°$)[3] and share an average opening angle of 90°. If one proton possesses a large kinetic energy, so that its velocity β is comparable with the speed of light, the average opening angle between the two scattered protons in the laboratory frame will have smaller magnitude (approximately 82° at $\beta \approx 0.712$). This is due to the fact that the relativistic mass of the incident proton is larger than the mass of the motionless proton.

[3]It is defined such that if $\Delta\varphi > 180°$ or $\Delta\varphi < 0°$, then $\Delta\varphi = 360° - \Delta\varphi$.

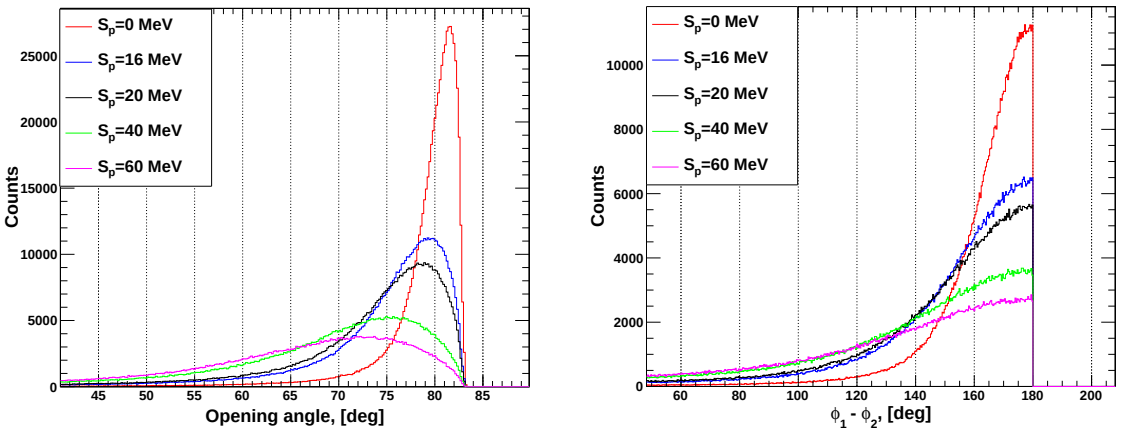

(a) Opening angle distributions

(b) Distributions of $\Delta\varphi$

Figure 4.7: Simulated angular distributions of proton pairs from the ^{12}C$(p,2p)^{11}$B reaction are shown for different proton separation energies S_p. The Goldhaber model for the internal momentum distribution is considered (for $S_p = 0$ the momentum width is artificially set to 100 MeV/c). The opening angle distribution (a) becomes wider with increasing Q-value of the reaction, since the internal momentum width also increases. The peak for $S_p = 16$ MeV (proton-separation threshold in ^{12}C) is located at around 80°. The $\Delta\varphi$ distribution (b) is plotted with a condition $\Delta\varphi = 360 - \Delta\varphi$ when $\Delta\varphi > 180°$. This plot shows a tendency of the two protons to be correlated "back-to-back" (*i.e* coplanar kinematics) with a maximum of the distribution at 180°.

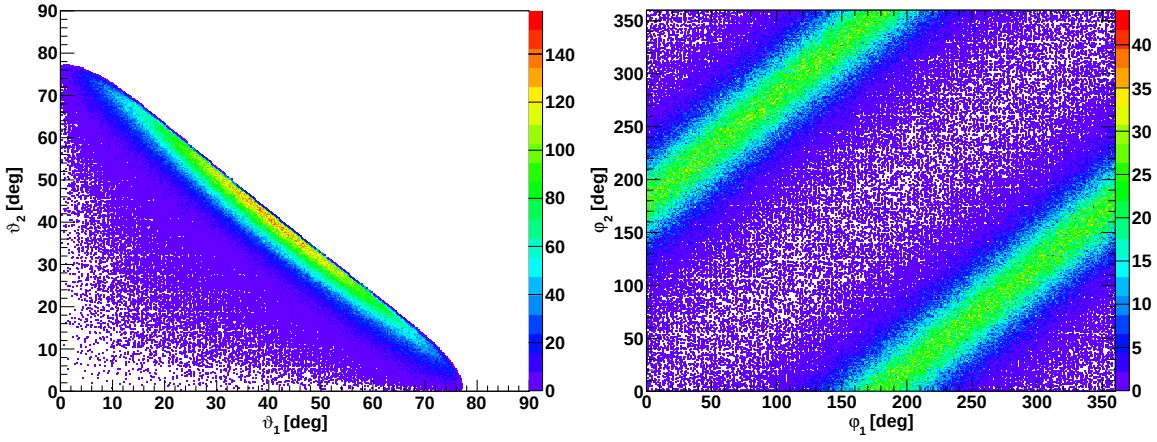

(a) Correlation of polar angles

(b) Correlation of azimuthal angles

Figure 4.8: Simulated correlations of polar (a) and azimuthal (b) angles of the two outgoing protons from the ^{12}C$(p,2p)^{11}$B reaction. The Goldhaber momentum width of 165 MeV/c corresponding to the proton separation energy of 16 MeV in ^{12}C has been used.

In case of the quasi-free scattering, the bound proton has non-zero momentum due to its internal motion inside the nucleus. This introduces additional spread in the angular distributions of outgoing proton pairs. The broadening effect must be especially strong for

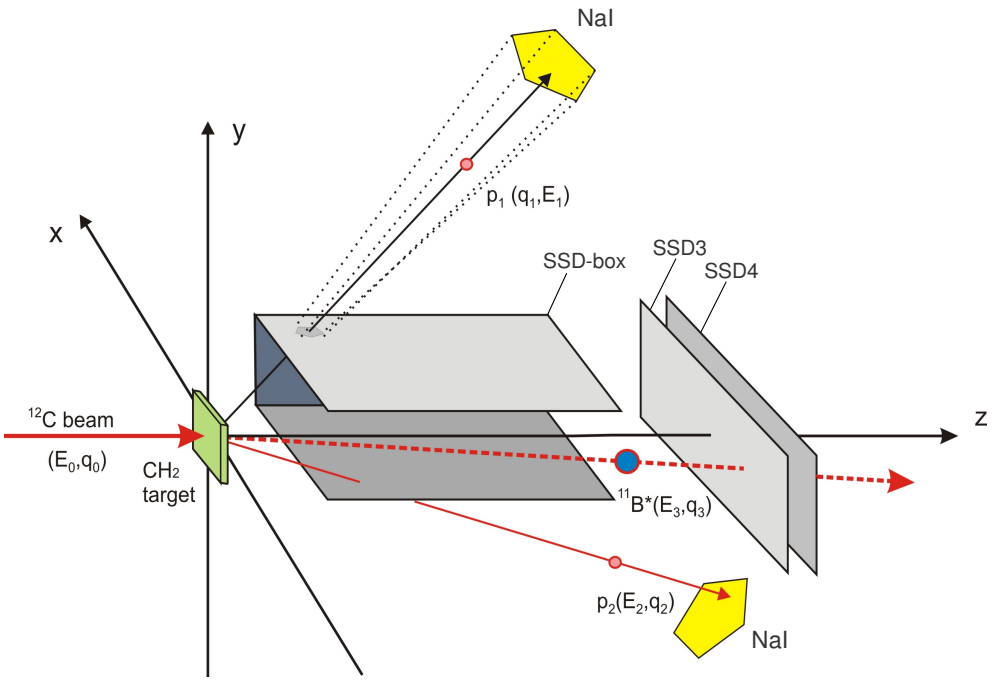

Figure 4.9: A schematic view of the proton tracking procedure. The two protons from the $^{12}C(p,2p)^{11}B$ reaction travel through the box-SSDs and hit the Crystal Ball, where their energy losses are measured. Appropriate hits in the SSDs are identified within the solid angles determined by the crystals which were hit (proton p_1 in the picture).

the knockout from deeply bound states, where the momentum uncertainty is presumably larger compared to valence loosely bound states.

To get an idea about the influence of the binding energy and the internal momentum on the observed proton angles, a kinematical simulation of the $^{12}C(p,2p)^{11}B$ reaction, employing the Goldhaber model (see Appendix), has been performed. The FORTRAN code for the simulation was kindly provided by Leonid Chulkov [54]. Figure 4.7 illustrates how the simulated angular distributions of proton pairs evolve with the binding energy, which characterizes the internal momentum widths of protons in the given model. Figure 4.8 presents the simulated correlations of polar and azimuthal angles of outgoing protons for the standard proton separation energy in ^{12}C, which corresponds to the Goldhaber momentum width of 165 MeV/c.

The present simulation is based on a simple kinematical approach employing the Feynman diagram technique (see Appendix), where no secondary interactions occur between the nucleus and the incident and the outgoing protons. In reality, the interaction with the spectator nucleons can have a significant distortion effect on the outgoing trajectories and hence affect the observed angular distributions, especially in the case of knockout from inner deeply bound states, when the protons are expected to travel longer distances inside the nuclear

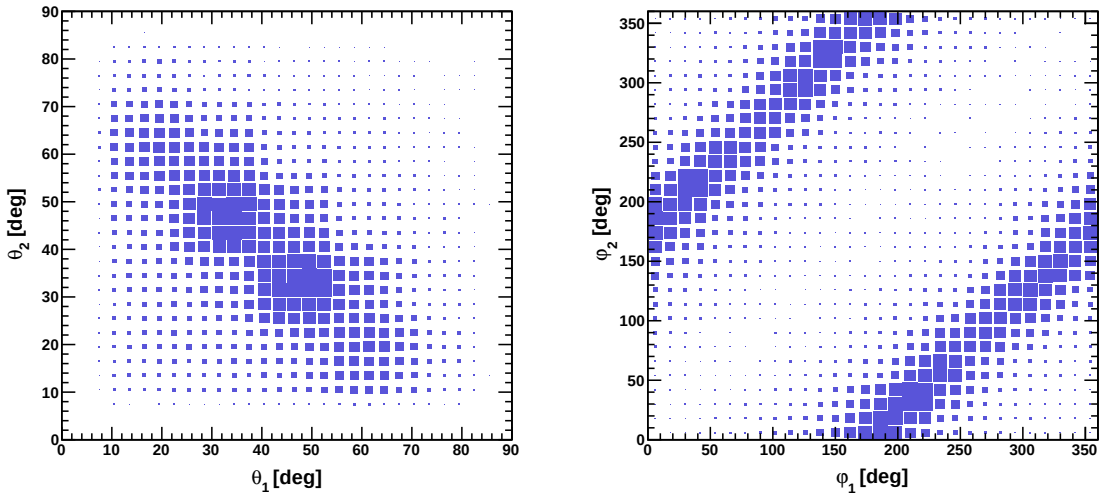

Figure 4.10: Correlation of polar (left) and azimuthal (right) angles of two protons observed in the Crystal Ball with the CH_2 target.

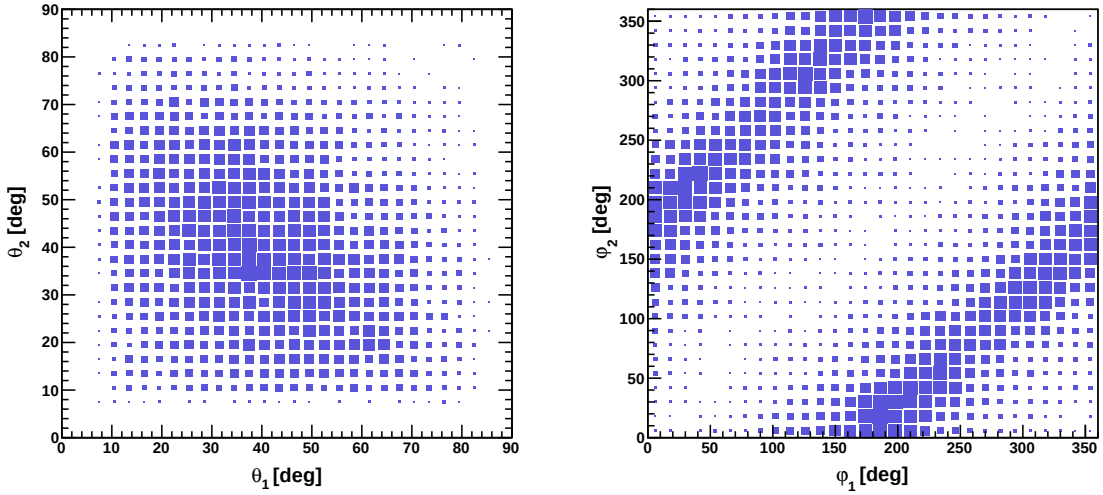

Figure 4.11: Correlation of polar (left) and azimuthal (right) angles of two protons observed in the Crystal Ball with the carbon target.

medium. Estimation of such distortions requires a rather complex reaction theory, which is not available at the moment. Therefore, in this thesis only a qualitative analysis of the angular distributions is presented.

The information about proton angles can be roughly obtained from the angular measurements in the Crystal Ball. Applying the add-back algorithm, one can identify which crystal was directly hit by each proton and use nominal angles of these crystals, namely, their positions with respect to the center of the detector. In order to get a more uniform distribution of the proton hits, the nominal angle of every crystal can be randomized over the solid angle covered by the corresponding crystal shape. Obtained in this way angular distributions of proton hits are shown in figures 4.10 and 4.11 for the CH_2 and the carbon target, respectively. Despite large angular uncertainties determined by crystal shapes, one can observe an

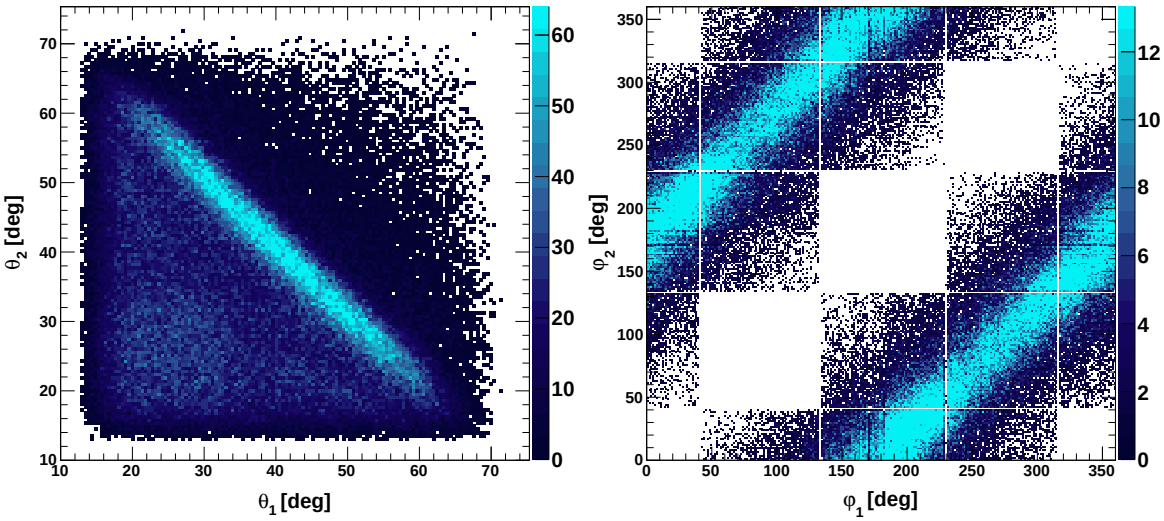

(a) Polar angles, CH_2

(b) Azimuth angles, CH_2

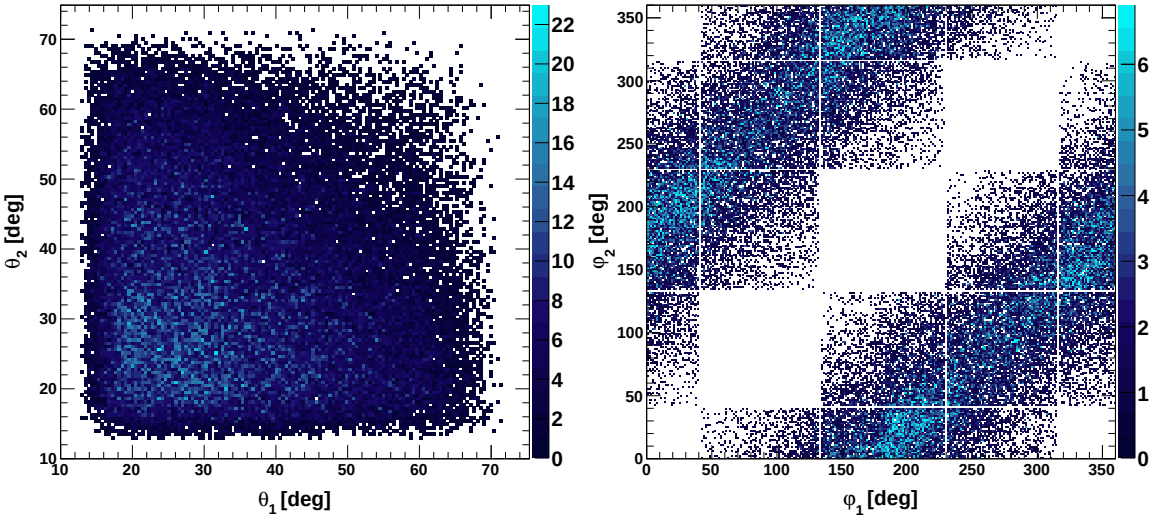

(c) Polar angles, Carbon target

(d) Azimuth angles, Carbon target

Figure 4.12: Angular correlations of proton pairs measured in the box-SSDs. Figures (a) and (b) present measurements with the CH_2 target, for which one observes enhanced angular correlations due to hydrogen-induced QFS reactions. This can be compared with the measurements on the carbon target which are shown in figures (c) and (d), where no such strong correlations is observed. Apparently, reactions on the carbon contribute mainly into background events in the CH_2 distributions. The narrow gaps in figures (b) and (d) are due to the distances between neighboring SSDs in the box, and the large square-shaped gaps are due to the requirement to detect two proton hits in different SSDs.

enhanced correlation pattern with the CH_2 target, which is similar to the simulated angular correlation (figure 4.8). The angular information is significantly improved, when coincident hits in the box-SSDs are required. If a proton hit in the box-SSD appears to lie within the angular range of the associated crystal, then the position information from the SSD is used

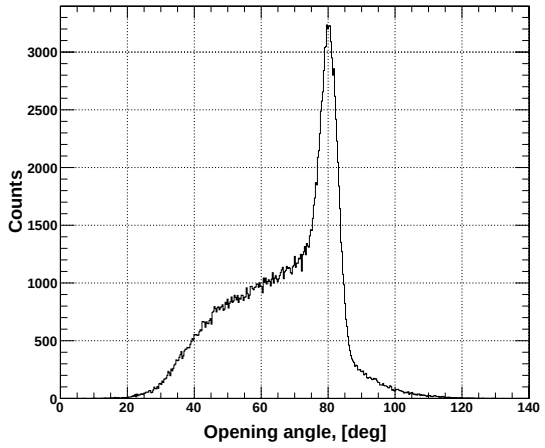

(a) CH_2

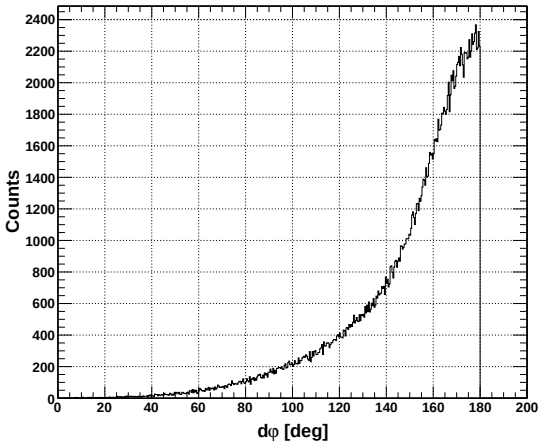

(b) CH_2

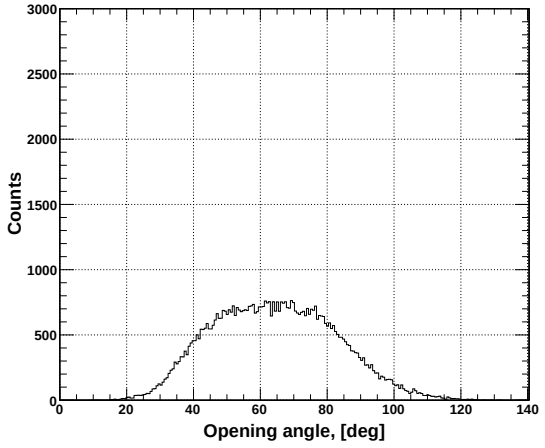

(c) Carbon target

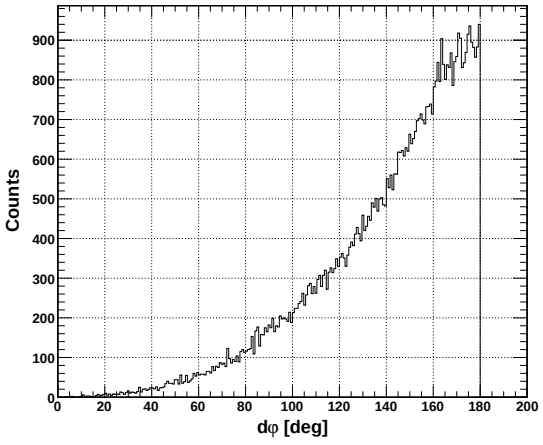

(d) Carbon target

Figure 4.13: Angular distributions of two-proton hits in the box-SSDs. Figures (a) and (b) present opening angles between the protons and their $d\varphi$ distribution measured with the CH_2 target. This result can be compared with the measurements on the carbon target in figures (c) and (d). From this comparison the background from the carbon in the CH_2 can be clearly identified.

to reconstruct the trajectory of the proton (see figure 4.9). This also requires a second point *i.e.* reaction vertex in the target which, however, cannot be determined precisely due to the lack of position information about the incident beam before the target. Therefore, it is assumed that all the reactions take place in average at a half of the target thickness along the Z-axis; the X and Y coordinates of the vertex can be then calculated by tracking back heavy fragments measured in the in-beam detectors SSD3 and SSD4. This leads to an additional uncertainty in the reconstructed angles, which is estimated to be $\pm 2.5^\circ$ for the 2.31 mm thick CH_2 target [44].

In order to have a better angular separation, the two proton hits are required to be detected by different SSDs. A strong argument for this is that the recoil protons are moving predominantly in opposite azimuthal directions and therefore should be observed in opposite

SSDs. This condition leads to an additional acceptance limit for the measured angles when $\Delta\varphi \lesssim 90^\circ$ (maximum φ-range of a single SSD from the box). Nevertheless, the reaction cross section at such angles is expected to be small. The acceptance efficiency of the box-SSDs has been estimated by comparing the total number of events for having outgoing ^{11}B and two high-energy clusters in the CB with the number of events when the protons are additionally tracked in the box-SSDs. The efficiency of tracking two protons in the box-SSDs is found to be approximately 70%, which comprises both, acceptance and detection efficiencies.

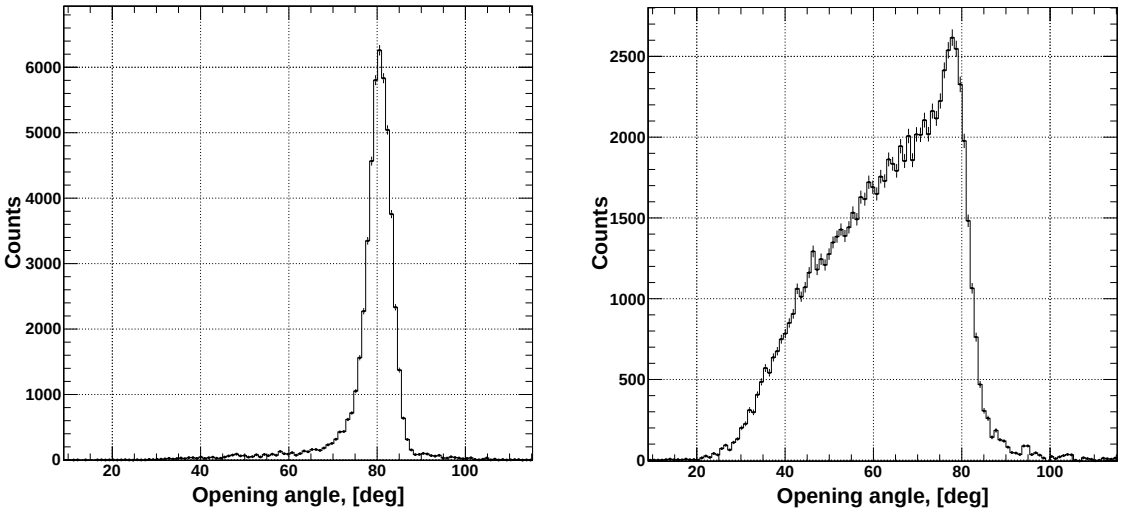

(a) Bound ^{11}B (b) Unbound ^{11}B

Figure 4.14: Opening angle distributions of proton pairs (without carbon background) are measured for bound and unbound states of outgoing ^{11}B from the ^{12}C$(p, 2p)^{11}$B reaction. This can be interpreted as a proton knockout form p- and s-shell, respectively.

A distinct correlation of polar angles of outgoing protons is observed with the CH_2 target (figure 4.12). At the same time, reactions on the carbon target do not reveal any strong correlation effect and therefore can be recognized as smooth uncorrelated background in the CH_2 distribution. The same indication of hydrogen-induced reactions is seen as a narrow peak at around 80° in the opening angle distribution for the CH_2 target (figure 4.13a). These observations agree very well with the simulated kinematics of the ^{12}C$(p, 2p)^{11}$B reaction (compare with figure 4.8a). Figure 4.14 illustrates distributions of the opening angles for the two cases: a) when only ^{11}B is observed in the final state, b) when any other fragment with the mass $A < 11$. In the first case, a proton is most likely knocked out from the valence p-shell of ^{12}C, leaving the residual ^{11}B in its ground state or in a weakly excited bound state. For such events, a narrow peak is observed at around 80.6° which agrees well with the simulated value of 81°. In the second case, which corresponds to the knockout of deeply bound protons and unbound s-hole states in ^{11}B, the opening angle distribution is broader and has a maximum value at approximately 78°. This can be explained by a larger variation of the binding energies and internal momenta of protons occupying the inner s-shell in ^{12}C.

4.2.3 Energy Measurements in the Crystal Ball

The energy losses of QFS protons in the Crystal Ball were reconstructed during the add-back procedure by energy summation in clusters of crystals. If a proton releases its full energy in the detector, *i.e.* if it's completely absorbed, the total kinetic energy can be measured. The energy-loss measurements have been previously studied by irradiation of a single CB crystal with proton beams at different energies [44]. It was shown that for the fully stopped protons the resolution of about 2% can be achieved for the total-energy-deposition peak even at high energies (between 180 MeV and 240 MeV). Despite a relatively large thickness of

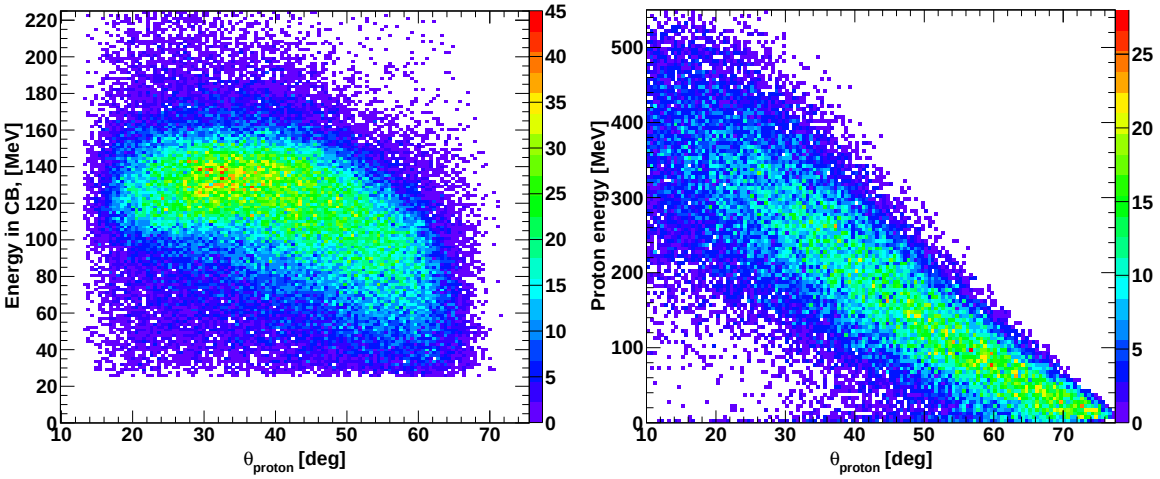

(a) Experiment (b) Simulation

Figure 4.15: Correlation between proton energies and their polar angles are compared for the experiment and the kinematical simulation. It is observed that more energetic protons at small angles tend to punch through the Crystal Ball.

the crystals ($\approx$ 20 cm), not all QFS protons can be fully stopped in the detector. When the energy is large enough, the protons can punch through the crystals leaving only some fraction of the energy. It was found via GEANT4 simulation [44, 48] that the majority of protons with an energy above $\sim$ 250 MeV tend to punch through the detector. From the kinematical simulation of the QFS reaction one expects the energies of outgoing protons to be correlated with the polar angle θ (see figure 4.15b). At small angles ($\theta \lesssim 40°$), where more energetic protons emerge, the total energy cannot be reconstructed due to the punch-through effect. On the other hand, when protons have small energies (*i.e.* below 25 MeV) and large angles, the add-back algorithm reconstructs them as photon hits. Hence, in the present experiment the energy measurements of protons are possible only in the angular range $\theta \gtrsim 40°$.

4.3 Integrated Cross Sections

The cross section of a nuclear reaction is a quantity, which characterizes the probability for interacting particles to end up in a certain final state. The value of the cross section σ_τ can be found experimentally by measuring the number of reactions R_τ occurring in the target τ

relative to the total number of incoming particles I_τ. This can be expressed as follows:

$$\sigma_\tau = \frac{R_\tau}{I_\tau}\frac{1}{T_\tau}, \tag{4.3}$$

where T_τ is the number of scattering centers per unit area of the given target:

$$T_\tau = s_\tau \times \frac{1}{m_\tau} = \rho_\tau d_\tau \frac{N_A}{A_\tau}, \tag{4.4}$$

where $s_\tau = \rho_\tau d_\tau$ is the area density of the target with volume density ρ_τ and thickness d_τ; $m_\tau = A_\tau/N_A$ is the mass of a single scattering center expressed via the molar mass of the target A_τ, and the Avogadro constant N_A.

In the present experiment, the CH_2 and pure carbon targets have been used to measure the cross sections of hydrogen- and carbon-induced knockout reactions. Additionally, measurements without target have been conducted in order to estimate the background from the setup. The number of reactions R_{H_2} induced by the hydrogen component of the CH_2 target can be found by subtracting the number of carbon-induced reactions (R_{CT}) and the reactions observed with empty target (R_{ET}):

$$R_{H_2} = R_{CH_2} - \frac{I_{CH_2}}{I_{CT}}\frac{T_{CH_2}}{T_{CT}} \times R_{CT} - \left(1 - \frac{T_{CH_2}}{T_{CT}}\right)\frac{I_{CH_2}}{I_{ET}} \times R_{ET}, \tag{4.5}$$

where the ratios T_{τ_1}/T_{τ_2} and I_{τ_1}/I_{τ_2} are statistical scaling factors which take into account the different numbers of scattering centers in the targets and the different numbers of measured incoming particles, respectively. Eventually, the cross section on hydrogen σ_H can be found by dividing the cross section for H_2 by two:

$$\sigma_H = \sigma_{H_2} \times \frac{1}{2}, \tag{4.6}$$

Statistical errors of the cross section for given target τ can be calculated by adding quadratically the statistical errors, which are associated with the number of reactions δ_{R_τ}, the number of incoming particles δ_{I_τ}, and with the number of scattering centers in the target δ_{T_τ} as follows:

$$\delta_\tau = \sqrt{(\delta_{R_\tau})^2 + (\delta_{I_\tau})^2 + (\delta_{T_\tau})^2}, \tag{4.7}$$

Similarly, the systematic errors can be taken into account. Table 4.1 presents the measured cross sections for different targets and for various reactions. A few comments will be made about each type of measurements.

Total (p,2p) cross section

The total cross section of the QFS reaction $^{12}\mathrm{C}(p, 2p)X$, irrespectively to the final state X, has been calculated using events with the "GOOD BEAM" trigger bit (see table 2.2). Although it is not a reaction trigger (it requires only "spill-on" and POS signals) and has a large downscaling factor of 512, this trigger is more suitable for counting the unbiased number of incoming particles due to its independence (unlike other triggers) on any detector signal after the target.

Events with two outgoing protons were identified using the add-back procedure and coincident hits in box-SSDs as explained in previous sections. In order to eliminate "pile-up"

Reaction \ Target	CH_2	Carbon	Hydrogen
$^{12}C(p,2p)X$	81.5 ± 4.0	20.5 ± 1.9	30.5 ± 2.3
$^{12}C(p,2p)^{11}B$	47.3 ± 3.3	11.1 ± 1.5	18.1 ± 2.0
p-removal	82.7 ± 7.7	45.9 ± 4.4	18.4 ± 2.7
pn-removal	48.1 ± 5.3	30.7 ± 2.3	8.7 ± 1.7
Inel. breakup to ^{11}B	2.64 ± 0.97	0.96 ± 0.65	0.84 ± 0.59

Table 4.1: Experimental cross sections in millibarns. The errors comprise statistical and systematic uncertainties as explained in text.

events, additional cuts were made on the energy in the POS detector and on the measured time intervals relative to the previous and to the following triggering event (not less than 5 μs in both cases). The number of measured $(p,2p)$ reactions on hydrogen has been corrected for the efficiency of 71±1.5% for the add-back algorithm as obtained from the simulation, and for the efficiency of the box-SSDs, which is approximately 70±1.4%. The total systematic error due to the efficiency corrections is estimated to be about 2%, which is small compared to the statistical error of about 7% for the cross section on hydrogen.

The reaction $^{12}C(p,2p)^{11}B$

The cross section of this reaction channel has been calculated in a similar way as before. In addition to all previous conditions, the outgoing ^{11}B was required to be detected in the fragment arm behind the magnet. This requirement has a disadvantage that some portion of the fragments may break up on the way from the target to the ToF wall, so that the number of measured reactions is always underestimated. Nevertheless, it is assumed that the break-up rate is the same for unreacted ^{12}C and for lighter reaction fragments and that the number of incoming particles can be well approximated by the number of unreacted ^{12}C behind the magnet. This approach has been proven to be valid in previous experiments at LAND-R^{3}B setup (see for example [44] or [49]). Besides efficiency corrections for the QFS protons in the Crystal Ball and in the box-SSDs, the acceptance of ^{11}B in the NTF (approximately 95±4%) has been taken into account. The total systematic error due to the efficiency corrections is estimated to be about 4.5% and the corresponding statistical error amounts approximately 10% for the cross section on hydrogen. The obtained cross-section of 18.1 ± 2 mb agrees quite well with the value of 16 ± 4 mb obtained in the previous QFS experiment employing normal kinematics with a 153 MeV proton beam [3]. Bound ^{11}B in the outgoing channel indicates the knockout of valence p-shell protons with relatively small binding energy. Comparing to the total $(p,2p)$ cross section, one can extract the contribution of unbound states, which are populated presumably via knockout from the s-state: $(30.5 - 18.1) = 12.4 \pm 3$ (mb), that comprises approximately 45% of the total cross section.

One-proton removal

The cross section of one-proton removal from ^{12}C on the carbon target has been calculated using data with the fragment trigger (Tpat&2 in table 2.2), which requires the outgoing fragment to be detected in the NTF. The energy cut on the fragments with Z=5 was made in the upstream SSD3 and the charge and mass selection of the outgoing ^{11}B was made in the fragment arm as well. Only outgoing ^{11}B fragments were considered for the reaction, regardless if there was any coincident signal in the CB or not. The calculation of this cross section is highlighted in more details in the previous work by Jon Taylor [48].

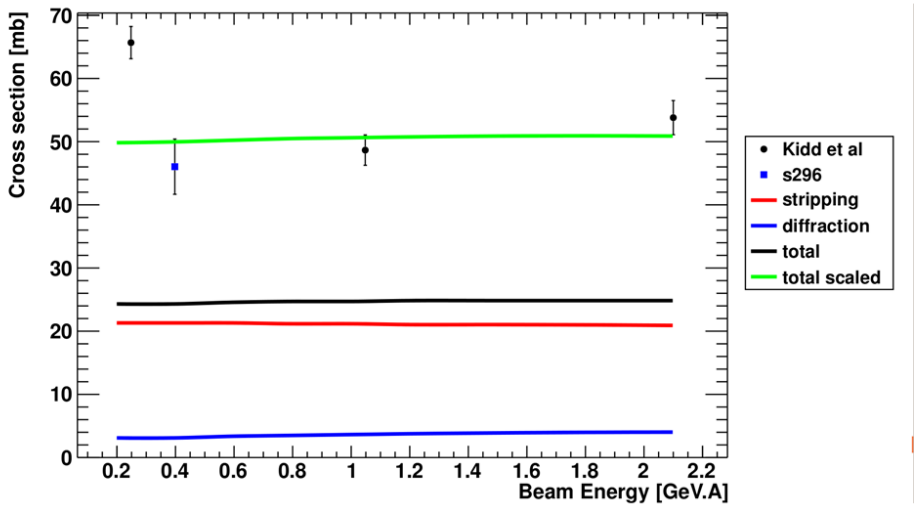

Figure 4.16: Comparison of the measured proton-removal cross section on the carbon target from the present experiment ('296') with previous results obtained at beam energies 250, 1050 and 2100 AMeV. The theoretical result (black line) is shown together with the contributing diffraction and stripping reactions which are indicated by blue and red lines, respectively. The black line is scaled by a factor of 2 (green line) to fit the experimental data. Due to the large discrepancy, the point at low energy can be discarded as a false measurement, like it has been done in other work [55].

The comparison of the obtained cross section with the results from other experiments and with the theoretical calculations is given in figure 4.16. The theoretical cross sections have been obtained via Glauber model calculations [56] [57] for removal of a single proton from the p-state in ^{12}C , The theoretical result is scaled by a factor of approximately 2 (spectroscopic factor) to fit the experimental measurements. Assuming that in the classical shell model there are four protons occupying the p-shell, one can find that the obtained spectroscopic factor is quenched by 50% compared to the shell model prediction (see figure 1.5 for comparison). The present measurement is in a good agreement with the measurements at higher energies and follows the expected energy dependence.

The reaction of pn-removal

This cross section was calculated in a way similar to the one-proton removal (see also [48]) *i.e.* without requiring a signal in the crystal Ball. The number of outgoing ^{10}B nuclei was

counted in the same way too. Besides the direct pn-removal reaction mechanism, this cross section contains contributions from two-step processes like proton or neutron removal with subsequent evaporation of a neutron or a proton from the respective final state.

Inelastic proton scattering

In order to estimate the role of inelastic proton scattering, *i.e.* excitation of ^{12}C into continuum with subsequent breakup to ^{11}B and a proton, a signal in the proton arm has been required in coincidence with the outgoing ^{11}B (only the proton-breakup is considered here). The cross section with hydrogen is found to be below 1 mb in both types of measurements (*i.e.* using the "GOOD BEAM" or fragment triggers), although the errors exceed 50% in both cases due to low statistics. The smallness of contribution from the inelastic scattering and the similarity of the cross sections for the $(p, 2p)$ and p-removal reactions on hydrogen permits one to attribute almost fully the QFS reaction mechanism to the proton removal process on hydrogen.

4.4 Momentum Distributions

4.4.1 Recoil Fragments

As follows from formula 1.2, the information about internal motion of the knocked-out proton from ^{12}C can be directly obtained by measuring the recoil momentum of the residual ^{11}B fragment. Since the incident beam carries a large momentum of 11.42 GeV/c with the transverse spread of about 0.02 GeV/c (see figure 4.19a), and the recoil momentum of outgoing ^{11}B is expected to be comparable with the Fermi momentum ($\approx$ 0.25 GeV/c), apparently, the transverse beam component has sufficient sensitivity to measure the recoil momentum. The longitudinal momentum component cannot be measured precisely in the present experiment in consequence of the limited time-of-flight resolution. Due to the straggling of the beam in the target, the transverse momentum width of the unreacted ^{12}C beam after the CH_2 target (figure 4.19b) shows an increase of about 10% with respect to the measurement without target. This is still negligible compared to the expected value of the recoil momentum.

The total momentum of the fragment is reconstructed from the velocity measurements in the tracking system behind the ALADIN magnet. For the known particle mass M with the relativistic velocity β, the total three-momentum can be written as follows:

$$P_0 = M\beta\gamma. \tag{4.8}$$

The transverse Cartesian components of the three-momentum in the laboratory coordinate system can be calculated using angular measurements in the in-beam SSDs:

$$P_x = P_0 \times sin(\alpha_x - \alpha_{x_0}), \qquad P_y = P_0 \times sin(\alpha_y - \alpha_{y_0}), \tag{4.9}$$

where α_x and α_y are the angles of outgoing fragments relative to the Z-axis in (X,Z) and (Y,Z) planes, respectively; α_{x_0} and α_{y_0} are the corresponding incident beam angles on the target (see figure 4.17) Lacking position measurements before the target, the incoming angles cannot be determined on an event-by-event basis. However, due a strong focusing of the primary beam on the target and nearly constant incident angle throughout the entire experiment, one

can instead use averaged values of α_{x_0} and α_{y_0} determined with the aid of non-reacted beam (figure 4.18).

Figure 4.20 presents the transverse recoil momentum distributions of outgoing ^{11}B fragments from the ^{12}C$(p, 2p)^{11}$B reactions on the hydrogen target. The background from the carbon-induced reactions in the CH_2 was measured with the pure carbon target and was subtracted according to formula 4.5. The obtained distributions are normalized to the integral cross section of 18.1 mb for the ^{12}C$(p, 2p)^{11}$B reaction, and the Gaussian fit is used to obtain the corresponding momentum widths which are 107.5±1.4 MeV/c and 106.6±0.7 MeV/c (with the errors from the fit) for the P_x and P_y components, respectively.

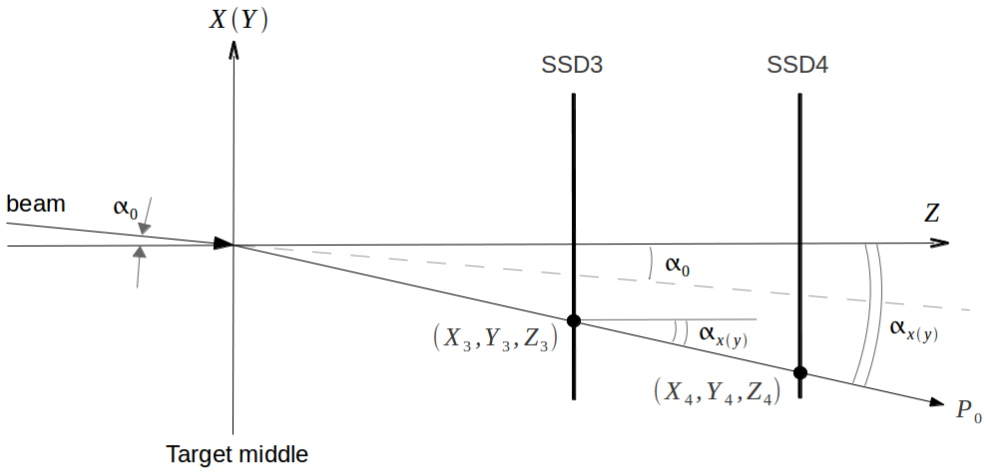

Figure 4.17: Schematic view of the heavy fragment tracking in the two silicon trackers (SSD3 and SSD4). Outgoing angles are reconstructed from the position measurements in the trackers as follows: $\alpha_x = \arctan(\frac{X_4-X_3}{Z_4-Z_3})$ and $\alpha_y = \arctan(\frac{Y_4-Y_3}{Z_4-Z_3})$. The incident angle α_0 is then subtracted in order to determine the outgoing angle relative to the incident beam.

The initial momentum spread of the ^{12}C beam is taken into account by quadratically subtracting the momentum width of the unreacted beam from the measured recoil momentum width. Thus, one can obtain σ_x=105.5 MeV/c for the P_x component and σ_y=104.6 MeV/c for the P_y component of the recoil momentum of ^{11}B, which correspond to the internal momentum of the p-shell protons in ^{12}C.

4.4.2 Recoil Protons

Alternatively to the momentum measurements of residual ^{11}B fragments, the internal momentum of a struck proton can be determined through the outgoing proton pair. When a single proton is completely absorbed in the Crystal Ball, so that its full kinetic energy T_k is measured, the total momentum Q of this proton is given by:

$$Q = \frac{1}{c}\sqrt{T_k(T_k + 2m_pc^2)}. \tag{4.10}$$

The energy measurements in the CB have been discussed in section 4.2.3. It was pointed out that at small polar angles ($\theta \lesssim 40°$), due to a large kinetic energy, the protons tend to

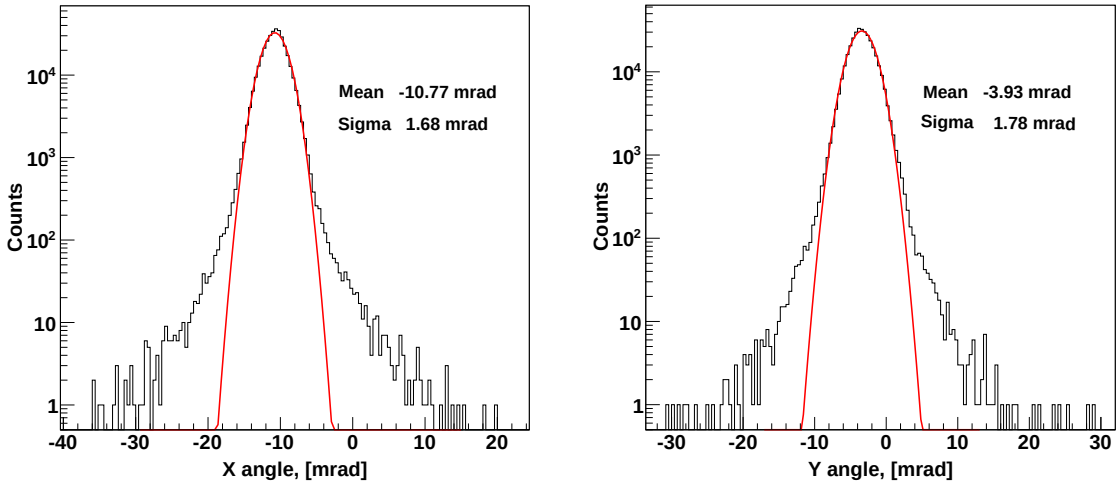

(a) (b)

Figure 4.18: Transverse angular distributions of the unreacted ^{12}C beam after the CH_2 target. The measurements in (X,Z) and in (Y,Z) planes are shown on the left and on the right figures, respectively. The observed mean values are used as α_{x_0} and α_{y_0} in the equation 4.9

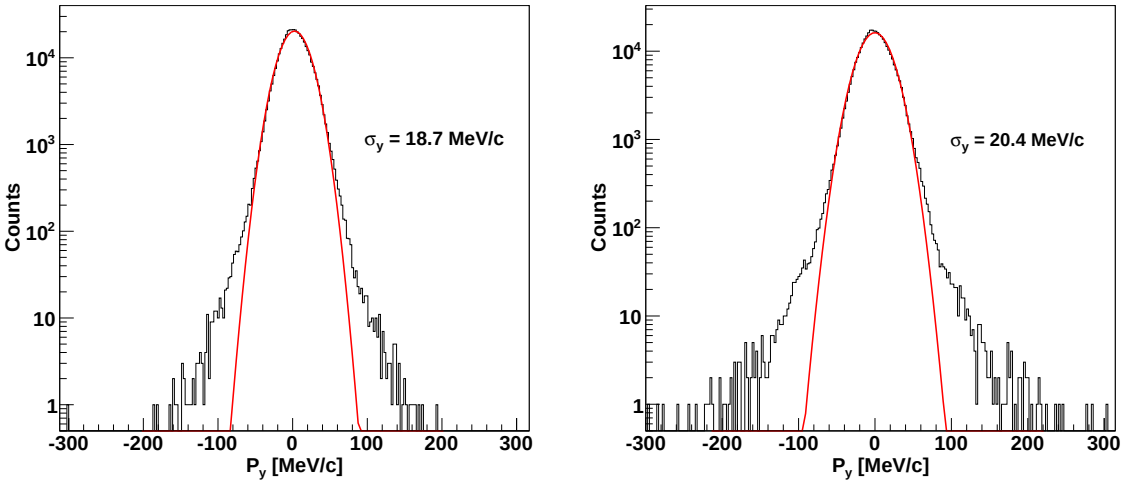

(a) Empty target (b) CH_2 target

Figure 4.19: Transverse momentum distributions of the incident ^{12}C beam were measured without target (a) and after the CH_2 target (b). A slight increase of about 10% is observed with the CH_2. The result is in agreement with the simulations via the ATIMA code [58].

punch through the CB crystals depositing only some portion of the energy (see figure 4.15). Nevertheless, due to nearly constant separation angle of about 80° between two outgoing protons and the average detection angle of 40° for both of them, it is very likely that at least one proton is detected at $\theta > 40°$, where the chance to punch through is smaller and the total energy can be measured. Using additionally the angular correlation with the second proton, one can determine the transverse Cartesian component of the internal momentum, applying

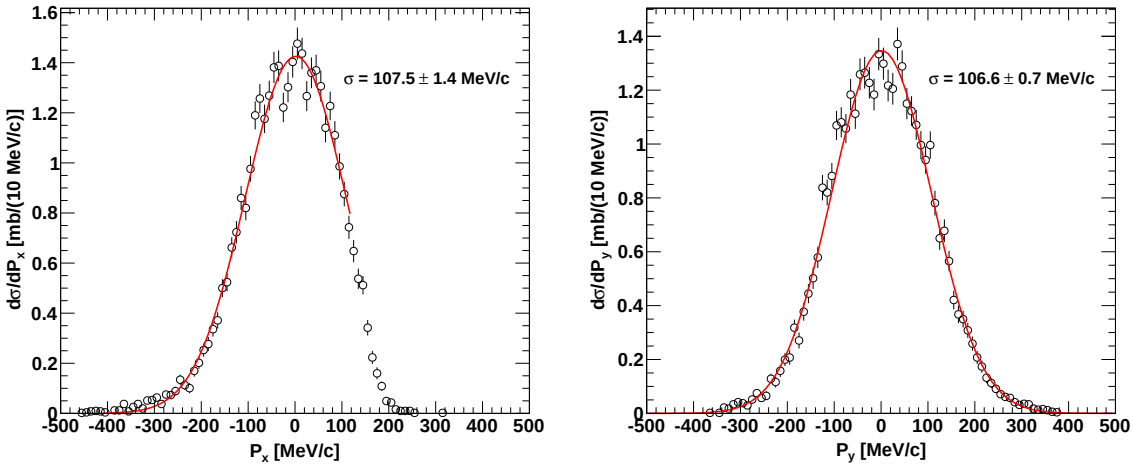

Figure 4.20: Transverse recoil momentum distributions of residual ^{11}B from ^{12}C$(p, 2p)^{11}$B reaction. The distribution of P_x has been fitted in the limited range due to acceptance losses in NTF along the dispersive X-axis of the magnet.

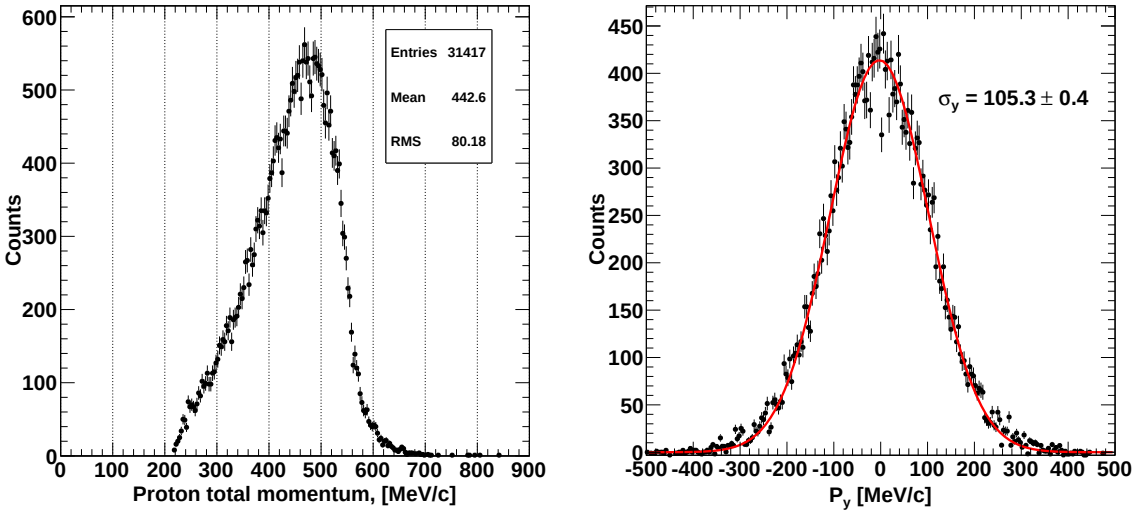

(a) (b)

Figure 4.21: Total momentum of one proton (a) is measured at polar angle above 40°. It is used for the reconstruction of the internal momentum (b). The obtained momentum width is in a good agreement with the measurements of the recoil ^{11}B fragments.

the formula from reference [9]:

$$P_y = Q_k \times sin\theta_k sin(\varphi_k - \varphi_i), \tag{4.11}$$

where k and i denote respectively "knocked-out" and "incident" protons in the outgoing channel, Q_k is the total outgoing momentum of k-proton in the lab, θ and φ are measured polar and azimuthal angles of the protons. Figure 4.21 presents the reconstructed momenta for the QFS protons when ^{11}B is observed in the final state. The resulting internal momentum

width of 105.3±0.4 MeV/c (figure 4.21b) agrees well with the direct measurement of the recoil momentum (compare to figure 4.20) and reflects the internal motion of protons occupying the p-shell in ^{12}C.

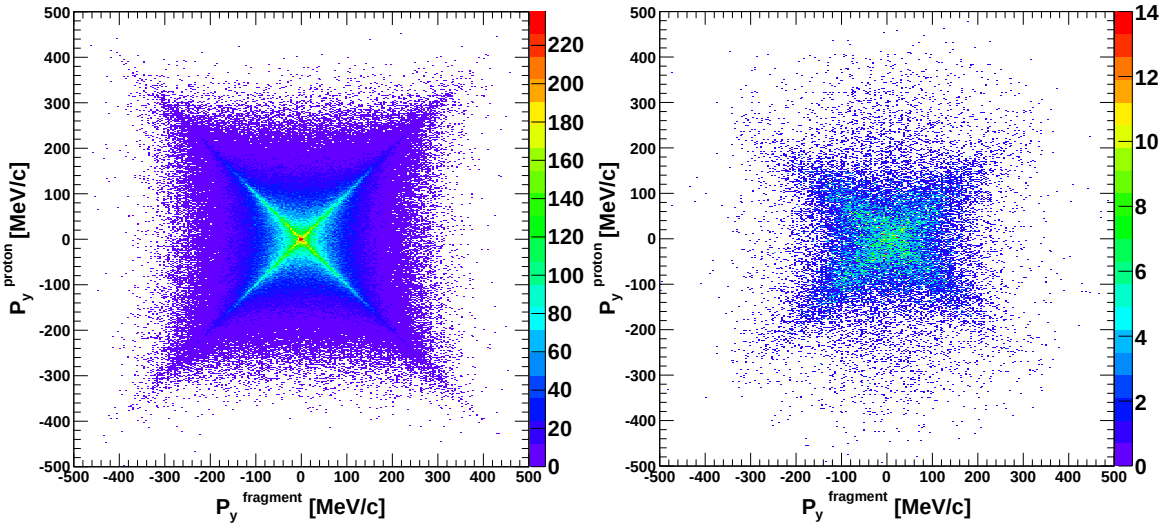

Figure 4.22: Correlation between Cartesian components of the internal momentum obtained via QFS proton pairs (P_y^{proton}) and through the measurements of the recoil ^{11}B fragments ($P_y^{fragment}$) in the same reactions. Left and right figures present the kinematical simulation and the experimental measurements, respectively. The fact that protons are indistinguishable particles gives rise to the correlated and anti-correlated components of the cross-like distributions.

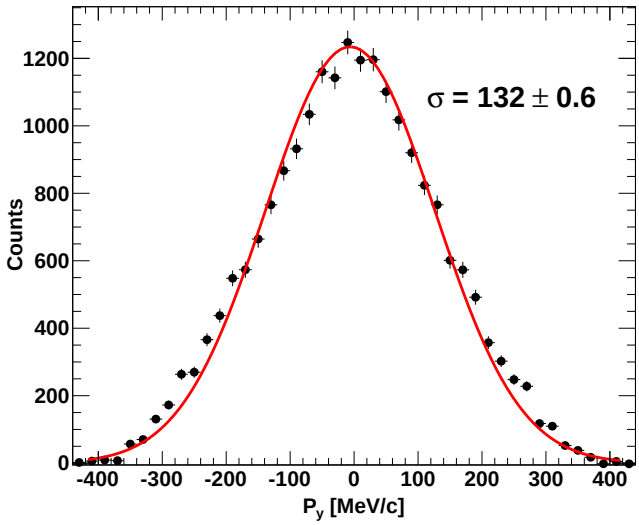

Figure 4.23: Internal momentum distribution of deeply bound protons is reconstructed via measurement of QFS proton pairs, when anything but ^{11}B is observed in outgoing channel.

Both types of measurements can be cross-checked by plotting the recoil momentum of ^{11}B against the internal momentum measured via proton pairs (figure 4.22b). A clear correlation

between the two measurements is also in agreement with the kinematical simulation (figure 4.22a). This validates both approaches as well as the consistency of the obtained results. Due to impossibility to identify which of the two protons is knocked out and which is scattered, the correlation has a diagonal-cross shape with the two components - one is the case when the incident proton is falsely assigned to be the knocked-out one (correlated component); the second component (anti-correlation) is when the assignment is correct.

The method with QFS protons can be applied to obtain the internal momentum distribution of strongly bound states in ^{12}C (*i.e.* s-shell), when direct measurements of unbound recoil fragments are difficult. In order to select the reaction channel, any outgoing fragment except ^{11}B has been required. This selection ensures that the excitation energy of the residual hole-state in ^{11}B is above the lowest particle separation threshold. The binding energy of knocked-out protons in this case: $B_p \gtrsim (S_p^C + S_\alpha^B) \approx (16.0 + 8.7) = 24.7$ MeV, where S_p^C and S_α^B are proton and alpha separation energies in ^{12}C and ^{11}B, respectively. The internal momentum component of such deeply bound protons in ^{12}C is shown in figure 4.23 (after background subtraction). The observed width of 132 MeV/c is about 25% larger compared to the previously obtained width of 105 MeV/c for the p-shell protons.

4.5 Reconstruction of the Excitation Energy

Binding energy of a struck proton from the ^{12}C$(p, 2p)^{11}$B reaction can be obtained via direct measurement of the residual excitation energy E^* of the final hole-state. Using a simple summation with the proton separation threshold in ^{12}C ($S_p \approx 16.0$ MeV), one can calculate the binding energy B_p as follows:

$$B_p = S_p + E^*. \tag{4.12}$$

The magnitude of E^* can vary in a broad range from 0 MeV (ground state) up to several tens of MeV (continuum states), depending on how deeply the knocked-out proton is bound. Hence, from the experimental point of view, the excitation spectrum of outgoing ^{11}B can be divided into two regions - the low-energy part, where the nucleus is bound due to knockout from valence p-shell states; and the high-energy part, where it is unbound mainly due to knockout from the inner s-shell. In the first case, some low-lying discrete excited states can be populated. These states decay via emission of γ-rays, which are measured in the Crystal Ball. In the second case, invariant-mass reconstruction of the breakup fragments can be employed. The following sections explain in details each type of the measurements. Due to a strong "punch-through" effect in the Crystal Ball, the more traditional way of measuring the missing energy of the scattered protons is not suitable and therefore will not be further discussed.

4.5.1 Bound States and the γ-Ray Spectroscopy

The present experimental approach utilizes γ-ray spectroscopy as a tool to measure populations of low-lying discrete states in ^{11}B. A large percentage of ^{12}C$(p, 2p)^{11}$B reactions is expected to populate the $(3/2^-)$ ground state of ^{11}B [7], while less reactions lead to the excited states below the lowest particle evaporation threshold in ^{11}B (S_α=8.7 MeV).

The level scheme of ^{11}B is shown in figure 4.24. Considering $(s_{1/2})^2(p_{3/2})^4$ proton-shell configuration of the ^{12}C ground state, one can expect that the removal of one proton from

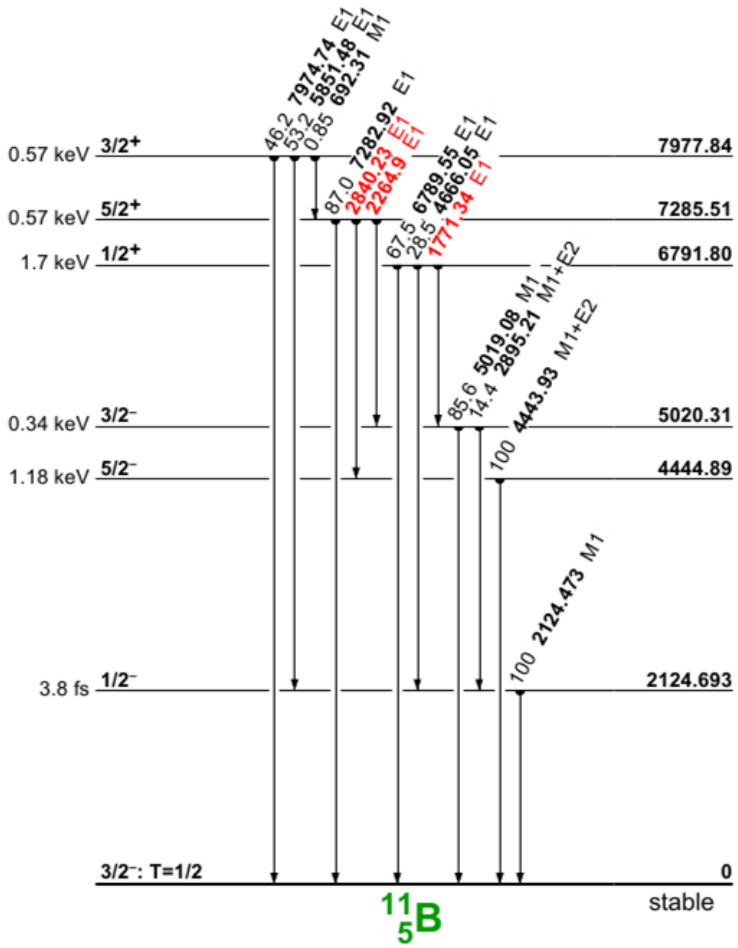

Figure 4.24: Level scheme of ^{11}B (according to [59]).

the p-shell creates a hole-state with the momentum and parity of either $(3/2^-)$ or $(1/2^-)$. This has been also confirmed by many other experiments (see for example [37]). Only a weak population of the states with higher momentum values can take place due to indirect two-step processes or due to ground-state correlations in ^{12}C [60]. The present analysis of the measured γ-ray spectrum has been conducted in essentially two steps: a) Doppler correction of the γ-ray energies; b) comparison of the resulting spectrum with the simulated detector response.

Doppler correction As a consequence of the Doppler effect, the observed energy of a photon emitted by a fast moving nucleus is a function of the emission angle relative to the beam axis and of the emitter velocity. The relation between the photon energy in the center-of-mass (CM) system of the nucleus and in the laboratory frame is given by:

$$E_{CM} = E_{lab}\gamma \times (1 - \beta cos\theta), \tag{4.13}$$

where E_{CM} is the photon energy in the CM system and E_{lab} is the energy observed in the detector; $\gamma = 1/\sqrt{(1-\beta^2)}$ is the Lorentz factor; $\beta = v/c$ is the velocity of the nucleus relative to the speed of light; θ is the emission angle.

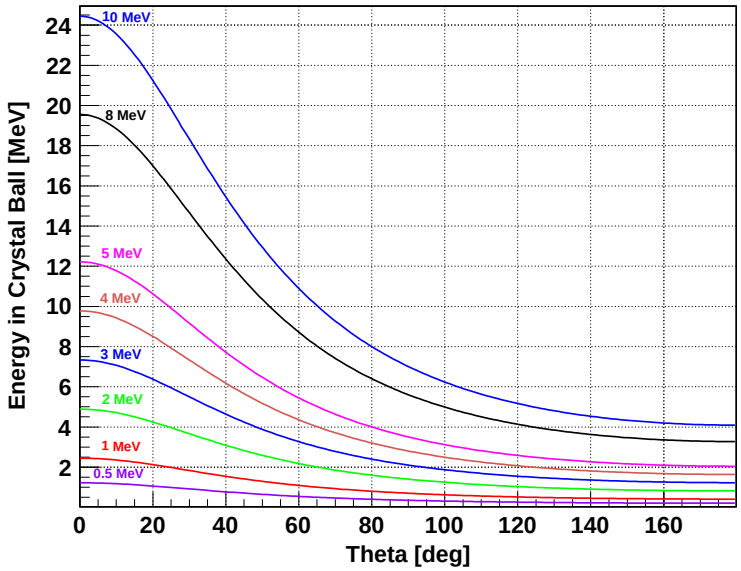

Figure 4.25: Calculated laboratory energies of γ-rays with different CM-energies as a function of the emission angle relative to the beam axis. The emitter velocity β is taken to be 0.711646 of speed of light that corresponds to the beam velocity at a half thickness of the target. Maximum energy amplification is expected at forward angles.

In figure 4.25 the effect of the Doppler shift on several γ-ray energies at given value of β is shown as a function of the angle θ. At forward angles ($\theta < 90°$), the laboratory energy increases nearly twice compared to the CM-value, while at backward angles ($\theta > 90°$) it can be two times smaller. Based on this, the energy of 25 MeV has been chosen as the upper threshold for γ-rays in the Crystal Ball.

The angles of the detected photons are determined at the uncertainty associated with solid angles of individual crystals ($4\pi/162 \approx 0.08$ sr for a single crystal). Thus, nominal angles of the crystals (*i.e.* the angles of their geometrical centers relative to the target) were used for the Doppler correction. Having such a large angular uncertainty, one can neglect the comparatively small outgoing angle of the forward-focused ^{11}B fragments. Using the angular information and the known fragment velocity, the photon energy can be transformed back to the center-of-mass system using equation 4.13.

Figure 4.26 presents the Doppler-corrected γ-ray spectra for the CH_2 and for the carbon target, measured in coincidence with two proton hits in the CB and with ^{11}B in the final state. The low-energy threshold of 400 keV has been used during the add-back procedure in order to eliminate crystals with low-energy noise produced by proton hits. As a result of the Doppler correction, the low-energy cut gives rise to the background peak at around 1 MeV in the corrected spectra. The first few excited states of ^{11}B can clearly be observed using both targets (compare to the level scheme in figure 4.24). The peaks appear at a slightly lower (by about 7%) energies, presumably due to a non-linearity of the present calibration at high energies, where the calibration has not been accurately tested. Excited states above 5 MeV are not observed due to domination of noise.

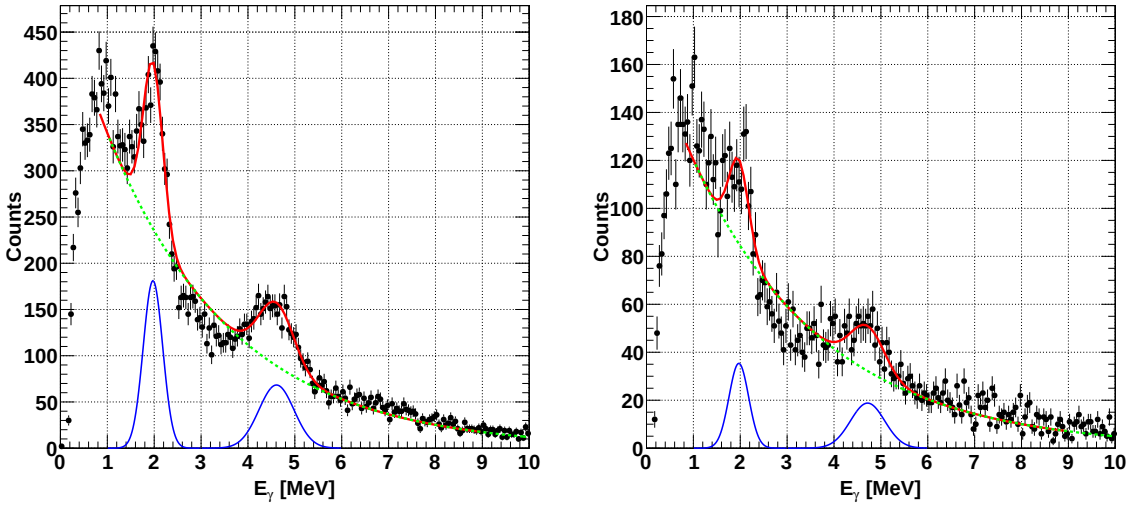

(a) CH_2 target (b) Carbon target

Figure 4.26: Doppler corrected γ-ray spectra are measured in coincidence with two-proton hits in the CB and with outgoing ^{11}B. A time window of $3\sigma_t \approx 6.4$ ns has been used to reduce the noise from protons (see figure 4.27). In every $(p, 2p)$ event, only those γ-hits are accepted which satisfy the timing condition. The two peaks correspond to the the first excited states in ^{11}B with the energies 2.125 MeV and 5.02 MeV (the state at 4.44 MeV is not expected to be populated in the QFS reaction). Each spectrum is fitted by two Gaussian functions combined with an exponential background. The resolution of the peaks is around 10%, which is mainly due to the angular acceptance of the crystals.

Simulated detector response In order to find the number of $(p, 2p)$ reactions populating a particular final state of ^{11}B, the experimental γ-ray spectrum is to be compared to the simulated detector response. For this purpose, the $^{12}C(p, 2p)^{11}B$ reaction has been simulated in the CB simultaneously with Lorentz-boosted γ-rays corresponding to the known γ-transitions from the excited states: a single γ-line at 2.125 MeV for the $(1/2^-)$ first excited state and three γ-lines (one from transition to the ground state and two from the cascade) for the $(3/2^-)$ state at 5.02 MeV. In the latter case, the appropriate percentages of all cascade transitions were taken into account. The simulated photons were isotropically distributed in a sphere in the center-of-mass system of the emitter (see Appendix). In order to achieve a more realistic detector response, the simulated energy losses in individual crystals were broadened according to the experimental energy resolutions obtained during the calibration procedure. In addition to this, the timing of a first interaction in every crystal was used as the actual timing of a hit in the crystal. Similar to the energy response, the time was randomized over a Gaussian distribution with the experimentally determined width (resolution) which was also obtained from the calibration.

Eventually, an identical analysis procedure as in the experiment was carried out for the simulated data, that includes the add-back and the Doppler correction algorithms as well. Clusters of crystals created by protons and by photons were separated from each other, and the times in the central crystals were assigned to the reconstructed hits.

A comparison of the experimental and the simulated time spectra is presented in figure

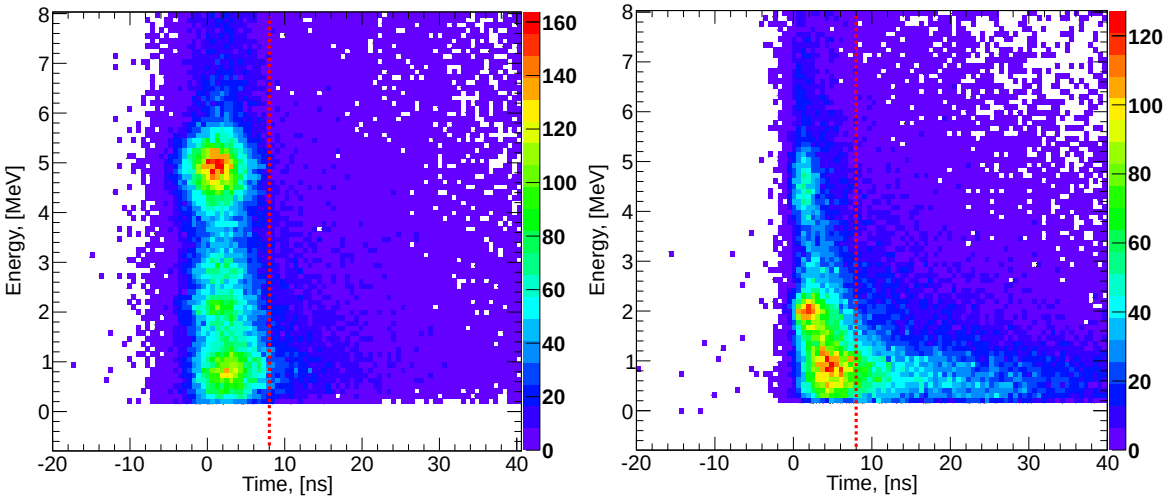

(a) Simulation with a cascade from 5.02 MeV state

(b) Experiment

Figure 4.27: Time spectra in the Crystal Ball for γ-rays from $^{12}\mathrm{C}(p,2p)^{11}\mathrm{B}$ reactions are shown for the simulation with a cascade from 5.02 MeV final state of ^{11}B (left) and for the experimental data (right) with the CH_2 target. The time cut at $3\sigma_t \approx 6.4$ ns (red dotted line) after the γ-peak was used to suppress noise.

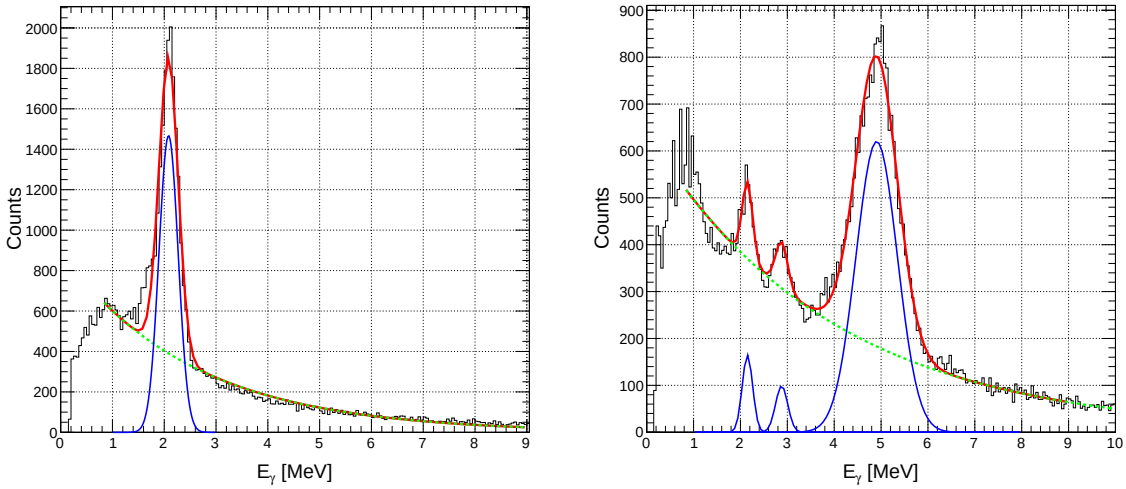

Figure 4.28: The simulated energy response of the Crystal ball for the two excited states of ^{11}B at 2.125 MeV (left) and 5.02 MeV (right) in coincidence with the $^{12}\mathrm{C}(p,2p)^{11}\mathrm{B}$ reaction.

4.27. Only those hits are accepted in the final spectra which arrive not later than 6.36 ns after the γ-peak (*i.e.* $3\sigma_t$, where $\sigma_t = 2.12$ is the nominal time resolution of individual CB crystals). The obtained responses for the two excited states in ^{11}B are shown in figure 4.28.

The final spectrum of photons accompanying the $^{12}\mathrm{C}(p,2p)^{11}\mathrm{B}$ reaction is obtained after subtracting the γ-ray spectrum measured with the carbon target (figure 4.26b) from the spectrum for the CH_2 target (figure 4.26a) using equation 4.5. In parallel, the corresponding number of hydrogen-induced $(p,2p)$ reactions is calculated in a similar way, *i.e* subtracting

the number of contributing carbon-induced reactions. The resulting spectrum is fitted by the simulated detector responses for the two excited states at 2.125 MeV and 5.02 MeV, and by a simulated background from protons. The result of the fit is shown in figure 4.29.

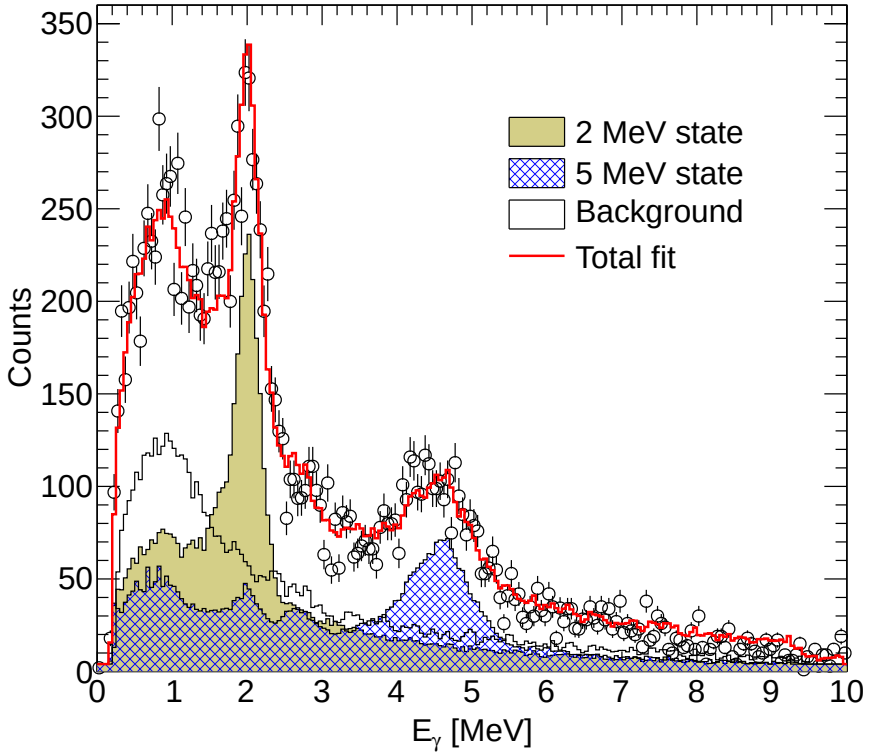

Figure 4.29: Background subtracted γ-ray spectrum in coincidence with $^{12}\mathrm{C}(p,2p)^{11}\mathrm{B}$ reactions. The spectrum is fitted by the simulated responses of the Crystal Ball for the two excited states of ^{11}B (see figure 4.28). Due to a slight energy mismatch between the simulated and the experimental positions of the peaks, a variable bin size and a common offset have been used as fitting parameters.

Using the integrated value of each response function $I_{fit}(i)$ in the fit and comparing it with the original integrated value $I_{sim}(i)$ from the simulation, one can find the corresponding number of $(p,2p)$ reactions $R_{exp}(i)$ populating the excited state i:

$$R_{exp}(i) = \frac{I_{fit}(i)}{I_{sim}(i)} \times R_{sim}(i), \tag{4.14}$$

where $R_{sim}(i)$ is the total number of reconstructed $(p,2p)$ events in the simulation. The number of reactions leading to the ground state is found by subtracting the sum $\sum_i R_{exp}(i)$ from the total number of measured $^{12}\mathrm{C}(p,2p)^{11}\mathrm{B}$ reactions. Hence, from the fit in figure 4.29, the following populations of the states in ^{11}B can be calculated relative to the total number of $^{12}\mathrm{C}(p,2p)^{11}\mathrm{B}$ reactions (using only statistical errors):

- 2.125 MeV state: $17.4 \pm 1.2\%$
- 5.02 MeV state: $12.1 \pm 0.9\%$
- Ground state: $70.5 \pm 3.1\%$

Considering the total cross section of 18.1±2 mb for the $^{12}C(p,2p)^{11}B$ reaction, one can calculate the following cross sections: 3.1±0.4 mb, 2.2±0.3 mb and 12.7±1.5 mb for the states at 2.125 MeV, 5.02 MeV and for the ground state, respectively.

Lacking the experimental sensitivity and energy resolution, no attempt was made to estimate the population of the states lying at higher energies. However, the contribution from these states must be smaller by approximately one order of magnitude compared to the two given states (see, for example, results from the $(e,e'p)$ experiment [60, 7]).

4.5.2 Unbound States and the Invariant-Mass Approach

The invariant-mass method has been successfully used for reconstructing the excitation energy of unbound reaction products in previous experiments at LAND-R^{3}B setup (see for example [61, 62]) and in other experiments [63]. The invariant mass M_{inv} of the system compounded of N particles is a physical quantity which remains constant under Lorentz transformations and which can be expressed via the square of the total four-momentum of the system[4]:

$$M_{inv}^2 = \mathbf{P}^2 = E_{tot}^2 - \vec{P}_{tot}^2 = \left(\sum_j^N E_j\right)^2 - \left(\sum_j^N \vec{p}_j\right)^2, \tag{4.15}$$

where $\mathbf{P}$ is the total four-momentum, E_{tot} and $\vec{P}_{tot}$ are the total energy of the system and the total three-momentum respectively, E_j and $\vec{p}_j$ are the total energies and momenta of the system's constituents.

Keeping in mind that the invariant mass is equal to the rest mass M_0 of the system, one can write for the initial state with the excitation energy E^*:

$$M_{inv} = M_0 + E^*. \tag{4.16}$$

If a nucleon is knocked out from a deeply bound state, and the excitation energy of the residual hole-state is above a particle separation threshold, the system will break into fragments. Equation 4.15 can be then applied to reconstruct the invariant mass of the system. Assuming that all breakup fragments are produced in their ground states, the sums in the expression 4.15 can be expanded, using the relations: $E_j = \gamma_j m_j$ and $p_j = \gamma_j \beta_j m_j$, in the following way:

$$\left(\sum_j^N E_j\right)^2 = \sum_j^N (\gamma_j m_j)^2 + \sum_{j\neq k}^N \gamma_j \gamma_k m_j m_k, \tag{4.17}$$

$$\left(\sum_j^N \vec{p}_j\right)^2 = \sum_j^N (\gamma_j \beta_j m_j)^2 + \sum_{j\neq k}^N \gamma_j \gamma_k \beta_j \beta_k m_j m_k cos\theta_{jk}. \tag{4.18}$$

Requiring the balance of the invariant masses before and after the decay, one can eventually write for the sought-for excitation energy:

$$E^* = \sqrt{\sum_j^N m_j^2 + \sum_{j\neq k}^N \gamma_j \gamma_k m_j m_k (1 - \beta_j \beta_k cos\vartheta_{jk})} - M_0. \tag{4.19}$$

[4]Here, the metric of Minkowski space-time is assumed and that the speed of light is unity (Plank units).

As one can see from the last equation, the excitation energy E^* depends on the velocities β_j of the breakup fragments and on their relative angles ϑ_{jk}. Using complete kinematics measurements at the present setup, one can identify the forward-focused fragments and measure all required input parameters for the equation 4.19. The approximation that all decay fragments are produced in their ground states can be corrected by introducing into equation 4.19 the energies of γ-rays accompanying the reaction, however, no such attempt has been made in the present analysis.

The cross sections associated with individual breakup channels are calculated on the ground of the following common steps:

1. In order to find the number of $(p, 2p)$ reactions, the Crystal Ball trigger "CB OR" (see table 2.2) is always requested in coincidence with two-proton events, except for the case of a neutron decay, which has a dedicated (not downscaled) trigger in the neutron branch. During the experiment, the CB trigger was downscaled by a factor of 4 ($\pm$10%) that has been taken into account when calculating the absolute number of $(p, 2p)$ reactions.

2. The number of carbon-induced background reactions is determined using the same conditions. It is then subtracted from the CH_2 data according to the equation 4.5.

3. The absolute number of incoming particles is approximated by the number of non-reacted ^{12}C ions counted in coincidence with the fragment trigger in NTF, which has a downscaling factor of 128 ($\pm$10%). This approach has been discussed in section 4.3. Similar energy cuts in the in-beam SSDs are used for counting the number of non-reacted particles and the number of reaction fragments.

4. The number of $(p, 2p)$ reactions is corrected for the two-proton total detection efficiency (approximately 50%), which combines the efficiency of the add-back algorithm and of the box-SSDs. The corresponding detection and acceptance efficiencies for the breakup fragments are taken into account as explained in the following text.

The above-described approach has been tested for the $(p, 2p)$ cross section leading to bound states of ^{11}B. The obtained value of 19.4$\pm$3.3 mb agrees within the error bars with the value of 18.1$\pm$2 mb, which was calculated via the method explained in section 4.3. Statistical errors are estimated to be about 7%, while a larger systematic error comes from the uncertainty associated with fluctuations of each trigger-downscaling factor during the experiment, and from the total error of 4.5% due to efficiency/acceptance corrections of the Crystal Ball, box-SSDs and NTF.

The following sections explain in detail the reconstruction of excitation energy spectra for a few observed decay modes. The analysis of the fragmentation into three and more particles is difficult due to the lack of tracking sensitivity and only the case of the triton decay will be highlighted.

Breakup channel $^{11}B^* \rightarrow ^{10}B + n$

This channel has been investigated through simultaneous measurements of outgoing ^{10}B in the fragment arm and a neutron in the LAND detector. The time of flight and position information from LAND is used to reconstruct the neutron velocity (figure 4.30a). The γ-peak

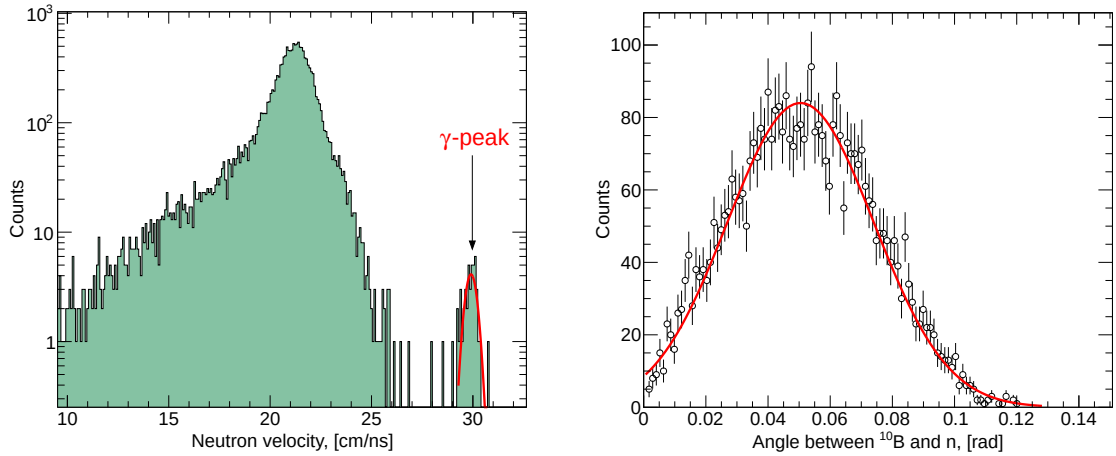

Figure 4.30: The velocity distribution of neutrons in LAND (left) and their relative angles with respect to the residual ^{10}B fragments (right) are shown for the CH_2 target in coincidence with $(p, 2p)$ reactions. The γ-peak is due to photons which originate from the target. The average opening angle between a neutron and a fragment is approximately 50 mrad in the laboratory coordinate system.

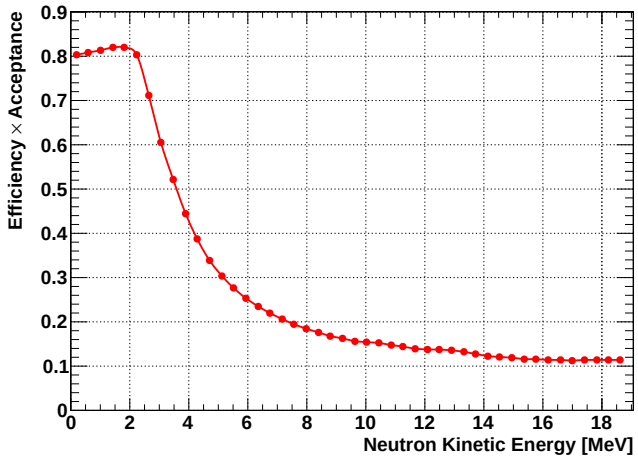

Figure 4.31: The detection efficiency of a neutron in LAND is obtained in simulations using the LEG code. The rapid drop of the efficiency at around 2 MeV is mainly due to acceptance losses for neutrons with large kinetic energies in the rest frame of a fragment.

at around 30 cm/ns (*i.e.* speed of light) with a width of 0.24 cm/ns serves as a reference point for the ToF/velocity calibration [49], and the broad peak from slower neutrons is observed at approximately 21.2 cm/ns. Applying the shower-reconstruction algorithm for neutrons, which is implemented in the LAND02 package ([49], [52]), one can determine spherical coordinates of neutron hits in LAND. At the same time, identification and velocity measurements of ^{10}B fragments are obtained from the tracking system behind the magnet, and the position information from the in-beam SSDs is used to reconstruct the corresponding outgoing angles. A relative angle between ^{10}B and a neutron is then calculated event by event (figure 4.30b).

The number of observed neutron decays has been corrected for the detection efficiency

in the neutron detector. This requires the knowledge of a neutron kinetic energy in the rest frame E_{kin} of the decaying system, which can be calculated using the relativistic formula taken from [49]:

$$E_{kin} = \gamma_f \gamma_n m_n - \beta_f \gamma_f p_{||} - m_n, \tag{4.20}$$

where m_n is the neutron rest mass, subscripts f and n denote the fragment and the neutron quantities, respectively, and $p_{||}$ is the longitudinal component of the neutron momentum.

A simulation with the code LEG[5] [64] has been performed in order to estimate the combined acceptance-efficiency value for a single-neutron detection in LAND (figure 4.31). The obtained efficiency curve is then folded with the reconstructed excitation energy of ^{11}B which is given by formula 4.19. Besides that, the geometrical acceptance of 93% for the ^{10}B fragments in the NTF is taken into account.

Subtracting the contribution of carbon-induced reactions from the CH_2 data, one can eventually find the total $(p, 2p)$ cross-section of 2.08±0.22 mb for the neutron breakup channel (figure 4.32).

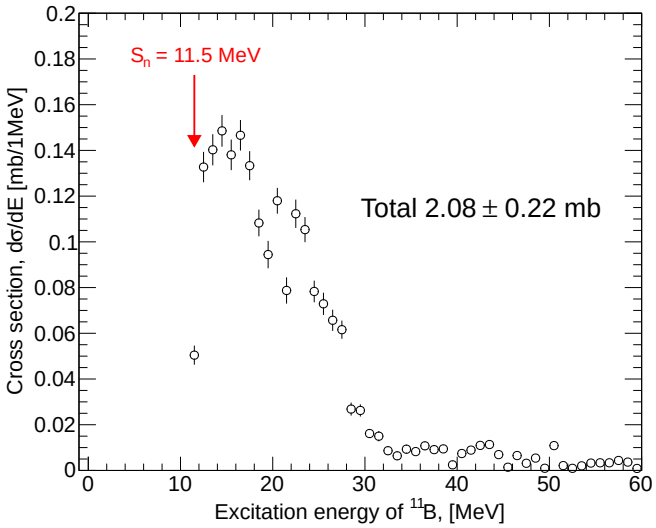

Figure 4.32: The excitation energy spectrum of ^{11}B is reconstructed for the neutron decay channel. The neutron separation threshold in ^{11}B is indicated by the red arrow.

Breakup channels $^{11}B^* \rightarrow (^{10}Be + p)/(^{9}Be + {}^{2}H)$

A proton breakup is analyzed using coincident measurements of ^{10}Be fragments and protons in two in-beam SSDs and in the tracking systems behind the magnet. In addition to the velocity measurements, the angular information from the in-beam SSDs is used to reconstruct the excitation energy as required by formula 4.19. Simultaneous detection of Z=1 and Z=4 particles in a single silicon tracker is shown in figure 4.33, and the resulting excitation spectrum of ^{11}B can be viewed in figure 4.34a.

It should be noted that, due to a rather poor geometrical acceptance for ^{10}Be fragments in the NTF (about 35%), the excitation energy spectrum contains only the information

[5] Land Event Generator.

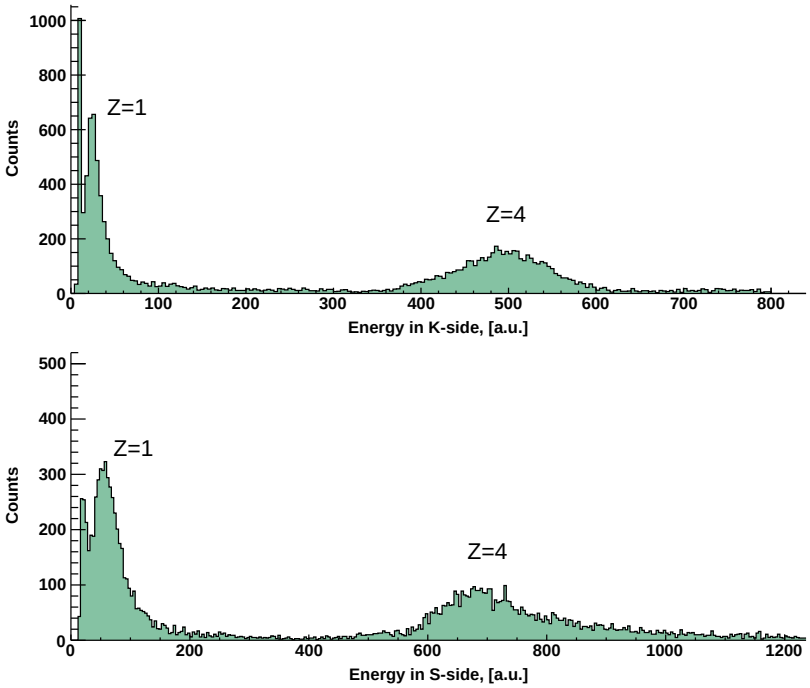

Figure 4.33: Coincident charge identification of two fragments with Z=1 and Z=4 in K- and S-side of the upstream SSD. An outgoing Be fragment is required behind the magnet.

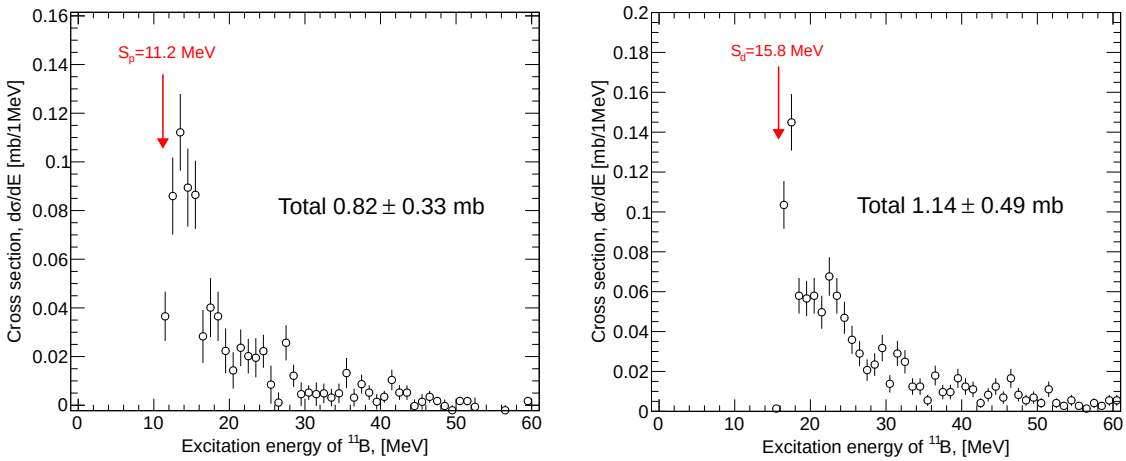

(a) Proton breakup

(b) Deuteron breakup

Figure 4.34: The excitation energy spectra are reconstructed for the proton (left) and the deuteron (right) decay modes of ^{11}B. The inset numbers display the total estimated $(p, 2p)$ cross sections for each channel.

associated with the reduced momentum space of the (^{10}Be + p) system, and no correction has been made for this as well as for the proton acceptance in the TFW and in the magnet. Such corrections would require a detailed simulation, which is not available at the moment. Nevertheless, an attempt is made to estimate the total $(p, 2p)$ cross section for this channel.

For this purpose, coincident energy cuts on Z=1 and Z=4 in both SSDs have been used regardless to the measurements in the proton arm. The efficiency of such cuts has been estimated for the case when both, the proton and the fragment, are successfully tracked behind the magnet, that gives the value of about 57%. Taking into account the acceptance efficiency of the ^{10}Be fragments in the NTF, a cross section of 0.82±0.33 mb is obtained. The reconstructed excitation spectrum is then normalized to the given value.

A very similar analysis procedure has been conducted for the deuteron-breakup channel. In contrast to the previous case, the deuterons, having A/Z ratio of two, are expected to be observed in the fragment arm, that is, however, not possible due to the lack of tracking sensitivity for Z=1 particles. For this reason, deuterons were identified only indirectly by requiring coincident Z=1 and Z=4 signals in both in-beam SSDs (see figure 4.33), ^{9}Be behind the magnet and no coincident signals in LAND and in the proton ToF-wall (in order to suppress the three-body decay). Since the decaying particles move with a velocity approximately equal to the velocity of the initial system, the same β-value can be assigned for the deuterons as for the ^{9}Be fragments. The reconstructed in such way excitation energy is shown in figure 4.34b. Similarly to the proton breakup, the cross section is calculated using the in-beam SSDs. The same energy cuts and efficiency corrections in the SSDs have been used as for the proton breakup, and the acceptance efficiency of ^{9}Be fragments in the NTF has been taken into account as well. Thus, the total cross section of 1.14±0.49 mb is calculated for the deuteron decay.

Breakup channel ^{11}B$^{*} \rightarrow$ (^{7}Li + ^{4}He)

Due to the ambiguity of tracking more than one heavy fragment in the fragment arm (see section 4.1), it turns out difficult to get a precise identification of all fragments' masses in case of the alpha breakup. Geometrical acceptance limitations in the NTF also play a role, when one is trying to explore exceptionally charge measurements in the ToF-wall, because one or another fragment can be missed if their relative momentum is large enough. In contrast to this situation, the silicon trackers have sufficient acceptance and multihit capability for measuring both particles at the same time, although their masses cannot be determined. Hence, an indirect mass identification has been attempted.

Figure 4.35 illustrates the charge identification of two coincident hits in a single in-beam SSD under condition to detect any fragment with Z≤3 in the NTF and a lithium ion in the second SSD. A clear evidence of coincident He and Li signals is observed. Applying the energy cuts in both SSDs and requiring no signals in the neutron and proton branches, the fragments can be treated as ^{4}He and ^{7}Li stemming from the breakup of ^{11}B. Of course, this method cannot provide a precise mass identification, and a three-body breakup cannot be fully eliminated as well as the admixture of another breakup channel ^{11}B$^{*} \rightarrow$ (^{8}Li + ^{3}He), nevertheless, the upper value of the cross section can be established. For the reconstruction of the excitation energy, the angular information from the SSDs is used as usually, and only mean values of the fragments' velocities are used in all events. The resulting excitation energy spectrum can be viewed in figure 4.36. The spectrum is normalized to the estimated cross section of 1.66±0.18 mb (with a statistical error), which has been calculated using relevant energy cuts only in K-sides of both SSDs and requiring at least one fragment with Z≤3 in the NTF. It is also assumed that the efficiency of the NTF to detect at least one of the two fragments is close to unity.

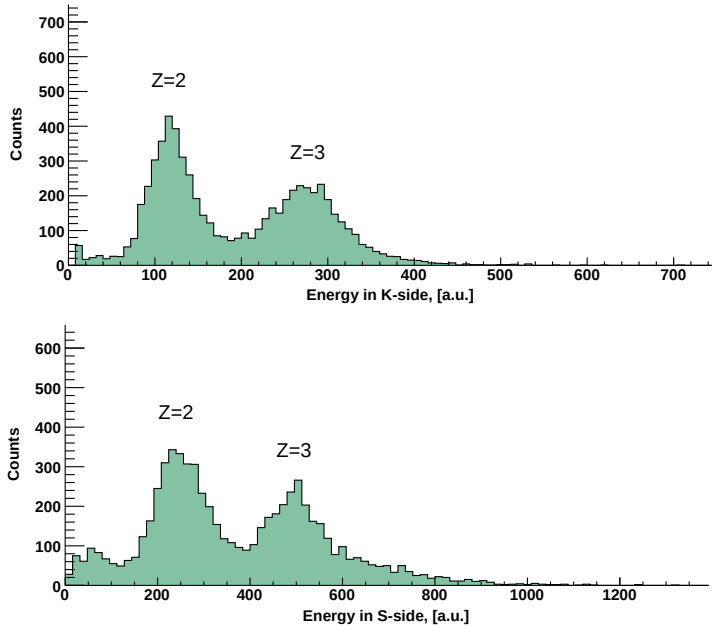

Figure 4.35: Coincident charge identification of Li and He isotopes in the in-beam SSD.

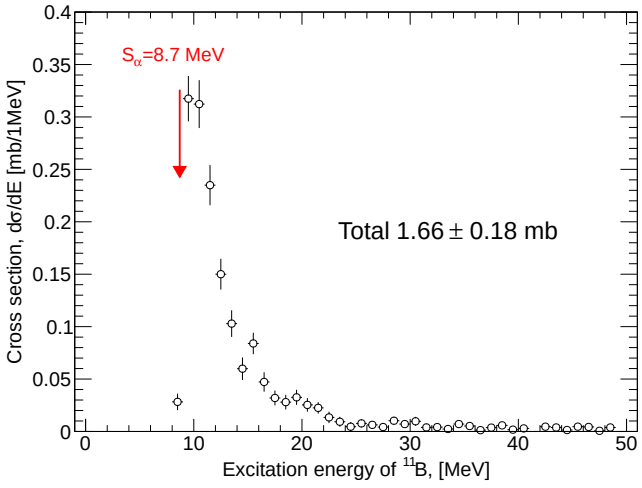

Figure 4.36: The excitation energy spectrum is reconstructed for the $^{11}B^* \rightarrow (^7Li + ^4He)$ breakup channel. The separation threshold for the alpha particle in ^{11}B opens at an energy of 8.7 MeV.

Three-body breakup

The invariant-mass method can be applied in the case of three-body decay, if the velocities and the angles of all three particles are known. Here, only a triton decay of ^{11}B leading to unbound system $^8Be \rightarrow (^4He + ^4He)$ will be considered. This channel is expected to carry a dominant strength of the s-hole decay at the excitation energies above 20 MeV, as reported by Yosoi *et al.*[37].

Although the three particle hits (*i.e.* two with Z=2 and one with Z=1) can be identified in

the in-beam SSDs, a correct velocity measurement for them is not possible. The situation is also complicated by significant acceptance losses for alpha-particles in the NTF. Nevertheless, the reconstruction of the excitation energy and of the cross section has been attempted under the assumption that all three particles have in average the same velocity as the decaying fragment, and that the probability to detect at least one particle in the NTF is close to unity. As before, an additional condition to have no coincident signals in the neutron and proton branches is applied. The resulting excitation spectrum is shown in figure 4.37. The cross section of 1.11±0.5 mb is determined for this decay channel, taking into account previously obtained efficiency of the energy cuts on Z=1 in the SSDs.

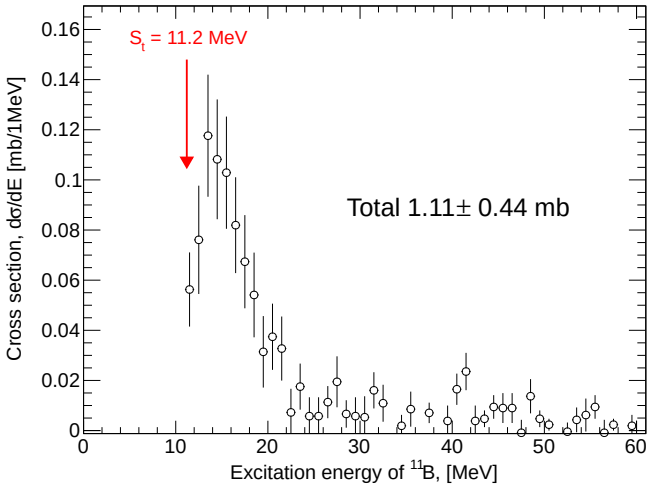

Figure 4.37: The excitation energy spectrum of ^{11}B for the three-body triton breakup.

4.5.3 The Total Excitation Spectrum

The total excitation spectrum of the ^{11}B from the ^{12}C$(p, 2p)^{11}$B reaction is reconstructed by combining the results of the γ-ray spectroscopy and the invariant-mass measurements described in previous sections. The resulting spectrum is shown in figure 4.38. The low-energy part, which corresponds to the proton knockout from the outer p-shell in ^{12}C, is filled according to the observed populations of low-lying states in ^{11}B. Only the bins which are associated with the actual energies of these states are filled, ignoring the experimental resolution for the γ-rays.

The high-energy part of the spectrum, lying above the lowest particle threshold (8.7 MeV), is represented by the sum of individual energy spectra reconstructed via the invariant-mass method. The broad peak at around 15 MeV can be associated with the proton knockout from the deeply-bound s-shell in ^{12}C, although the peak position is lower by about 5 MeV compared to what is usually observed for the s-hole state in ^{12}C. Apparently, the high-energy part of the s-hole state is missing due to many-body decays of ^{11}B, which were not considered in the present analysis. The integrated cross section, for all measured fragmentation channels (see table 4.2) is about 6.8±1 mb, which is about 55% of the total estimated cross section of 12.4 mb for the unbound states.

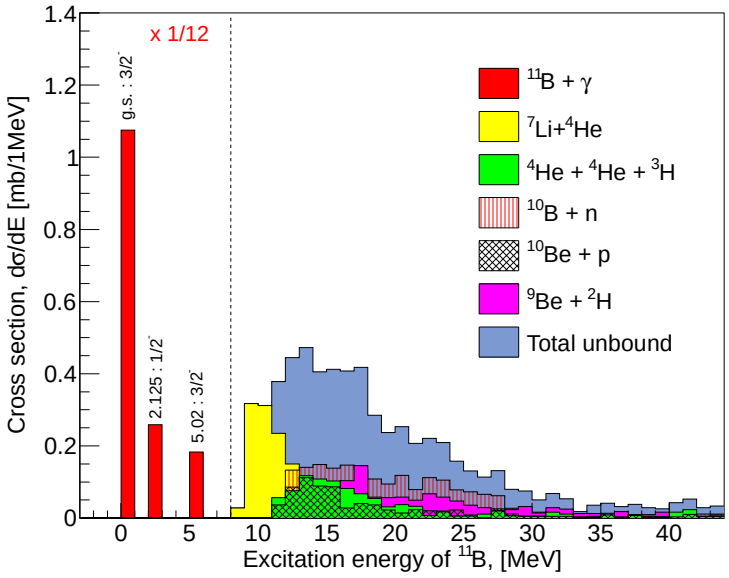

Figure 4.38: The total excitation energy spectrum of the residual ^{11}B from the ^{12}C$(p, 2p)^{11}$B reaction. The contributions of different decay modes are shown in colors. The low-energy part below 8.7 MeV is scaled down by a factor of 12 for a better representation.

SP shell	Final state	Cross section, mb	Total, mb
p-shell	G.S $\left(\frac{3}{2}\right)^-$	12.7±1.5	18.1±2
	2.01 MeV $\left(\frac{1}{2}\right)^-$	3.1±0.4	
	5.02 MeV $\left(\frac{3}{2}\right)^-$	2.2±0.3	
s-shell	^{10}B + n	2.08±0.22	12.4±3
	^{10}Be+p	0.82±0.33	
	^{9}Be + ^{2}H	1.14±0.49	
	^{7}Li + ^{4}He	1.66±0.2	
	^{4}He + ^{4}He + ^{3}H	1.11±0.44	
	Unidentified	5.7±3	

Table 4.2: Experimental cross sections for the ^{12}C$(p, 2p)^{11}$B reaction.

4.6 The Reaction (p, pn)

The analysis procedure, which is described in previous sections, can be also used for investigating the $^{12}C(p, pn)^{11}C$ reaction in inverse kinematics. Unfortunately, at the moment of writing this thesis a complete GEANT4 simulation for the $^{12}C(p, pn)^{11}C$ reaction is not ready, so that only experimental observations will be presented in this section.

Since the neutron separation energy at 18.7 MeV in ^{12}C is not very much different from the corresponding proton separation energy at 16 MeV, the reactions $^{12}C(p, 2p)^{11}B$ and $^{12}C(p, pn)^{11}C$ are expected to be rather similar from a kinematical point of view. However, it is more difficult to observe neutrons in the Crystal Ball, because they are weakly interacting particles and can escape the detector without producing a signal. Nevertheless, it is possible to detect the events in which outgoing ^{11}C fragment is accompanied by two high-energy hits (clusters) in the Crystal Ball. Such hits can be interpreted as proton-neutron pairs emerging from the $^{12}C(p, pn)^{11}C$ reaction. The analysis procedure is very similar to the one described previously for the $(p, 2p)$ reaction with the only exception, that neutrons cannot be tracked in the box-SSDs. The following criteria are used for identifying the (p, pn) reaction: a) ^{11}C in the fragment arm; b) two coincident high-energy hits in the Crystal Ball; c) only one coincident hit in the box-SSDs. The requirement to observe bound ^{11}C in the final state ensures that a neutron is removed from the valence p-shell in ^{12}C, leaving the residual nucleus either in its ground state or in some low-excited state.

The angular information about neutrons is obtained from the measurements in the Crystal Ball as explained in section 4.2.2, while the angles of protons are reconstructed in a usual way via the box-SSDs. The observed angular correlations of proton-neutron pairs are shown in figure 4.39. As expected, a distinct correlation pattern is observed with the CH_2 target, and the measurements with the carbon target do not reveal such strong effect. This indicates, that the correlations originate from the QFS reactions induced by the hydrogen component of the CH_2. The angular correlations are very similar to the ones measured for two protons from the $^{12}C(p, 2p)^{11}B$ reactions (compare with figure 4.10). The opening angles and dφ distributions of the proton-neutron pairs are shown in figure 4.40. The peak in the opening angle distribution for the CH_2 (see figure 4.40a) is at around 80°, which agrees quite well with the expectations from the reaction kinematics. The width of the peak is dominated by the angular resolution for neutrons *i.e.* the resolution of CB crystals. The corresponding dφ distribution also indicates a tendency for the coplanar reaction mechanism. Hence, the QFS reactions of a type (p, pn) can be clearly identified.

Deposited energies of protons and neutrons in the Crystal Ball are reconstructed via the add-back algorithm as explained in section 4.2.1, and the resulting energy-loss spectra are shown in figure 4.41. The energy response from neutrons has maximum at around 50 MeV which is about 80 MeV lower compared to the one from protons, although both distributions behave similarly at higher energies *i.e.* have similar tails above 150 MeV.

The recoil momentum distribution of outgoing ^{11}C fragments was measured in the same way as the one for ^{11}B fragments from the $^{12}C(p, 2p)^{11}B$ reactions (see section 4.4.1). The total momentum of ^{11}C was reconstructed via measurements in the fragment arm, and the angular information from the two in-beam SSDs was then used for reconstructing the transverse Cartesian component of the recoil momentum. The resulting momentum distribution has a width of 108.4±1.1 MeV/c (see figure 4.42) after subtracting the carbon background in the CH_2. The momentum spread of 20.4 MeV/c for the incident beam has been quadratically

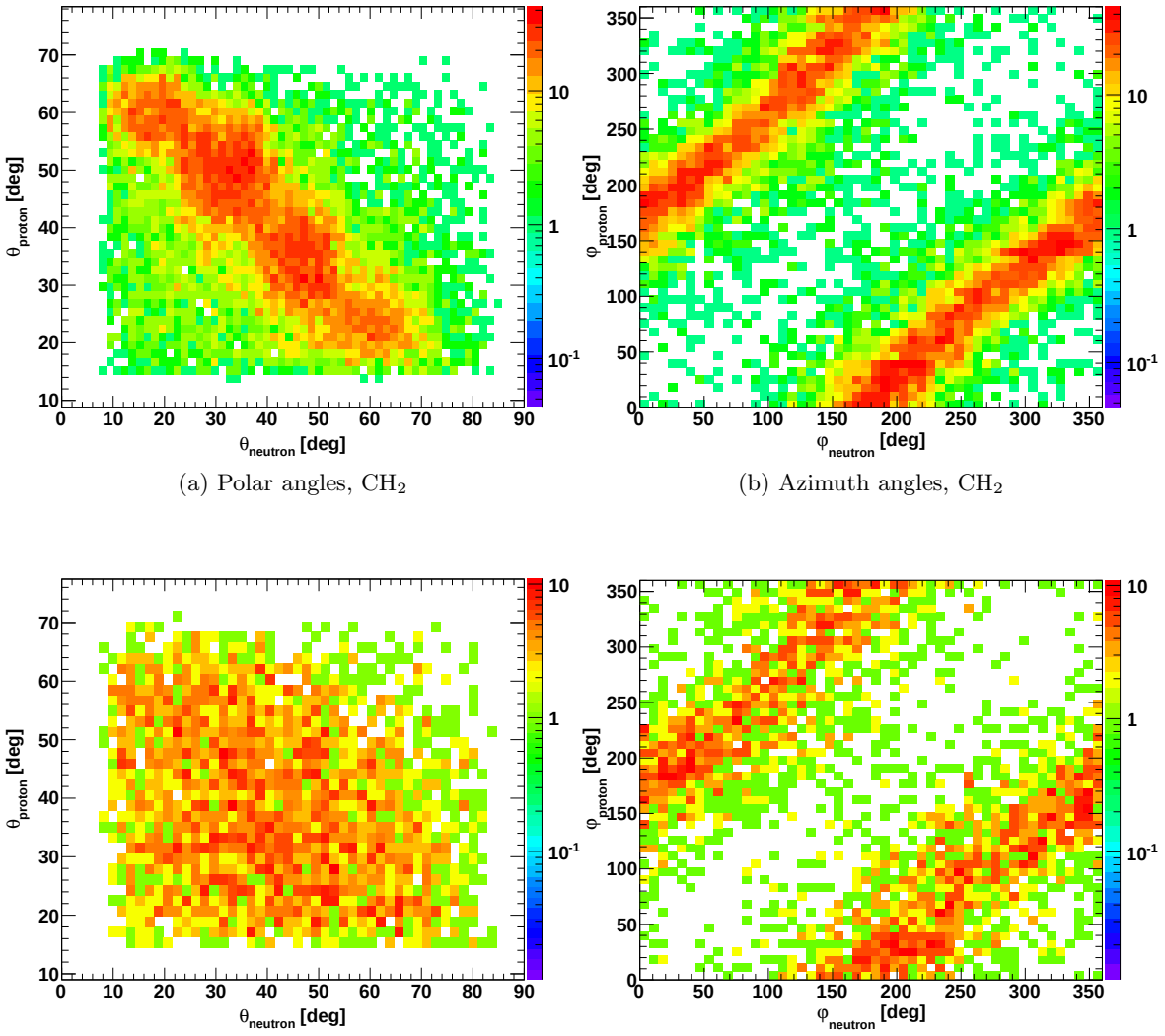

(a) Polar angles, CH_2

(b) Azimuth angles, CH_2

(c) Polar angles, Carbon target

(d) Azimuth angles, Carbon target

Figure 4.39: Angular correlations of proton-neutron pairs from the $^{12}C(p,pn)^{11}C$ reactions. Figures (a) and (b) present correlations of polar and azimuth angles measured with the CH_2 target. This can be compared with the measurements on the carbon target which are shown in figures (c) and (d).

subtracted in order to obtain the true value of 106.5 MeV/c for the recoil momentum width. This value reflects the internal momentum width of valence p-shell neutrons inside the ^{12}C and is very close to the width of 105 MeV/c obtained for the p-shell protons through the $^{12}C(p,2p)^{11}B$ reaction.

The Doppler-corrected energy spectra of γ-rays in coincidence with the $^{12}C(p,pn)^{11}C$ reactions are shown in figure 4.43. The two first excited states of ^{11}C can be observed that is similar to the γ-spectrum measured for ^{11}B from the $^{12}C(p,2p)^{11}B$ reaction (compare with figures 4.29 and 4.26). This is due to the fact that ^{11}B and ^{11}C are mirror isobars and their level schemes are rather similar. Hence, the observed states at 2 MeV$\left(\frac{1}{2}\right)^-$ and 4.8 MeV$\left(\frac{3}{2}\right)^-$ in ^{11}C are the analog states of 2.1 MeV$\left(\frac{1}{2}\right)^-$ and 5 MeV$\left(\frac{3}{2}\right)^-$ states in ^{11}B. In the first case, a hole is created in the neutron p-shell, while in the second case the excitation is due to

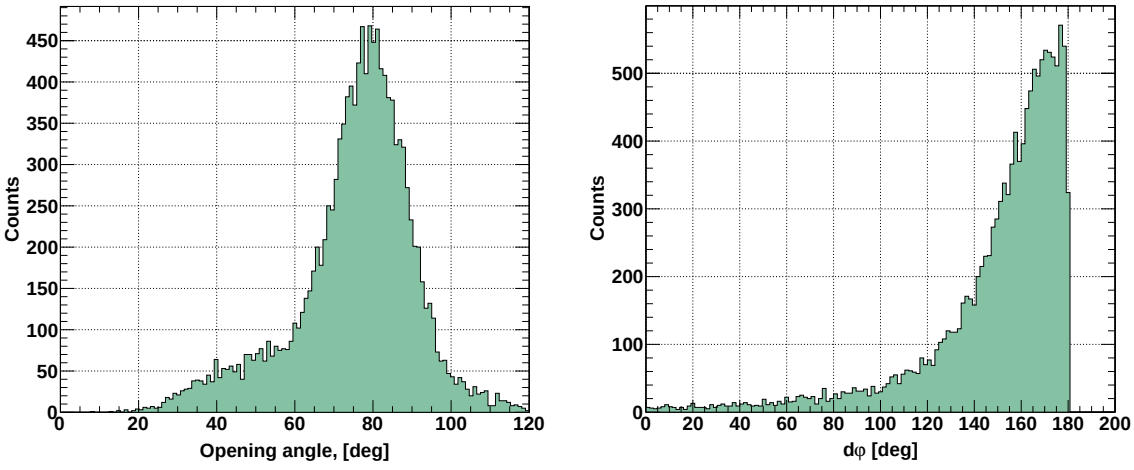

(a) CH_2 (b) CH_2

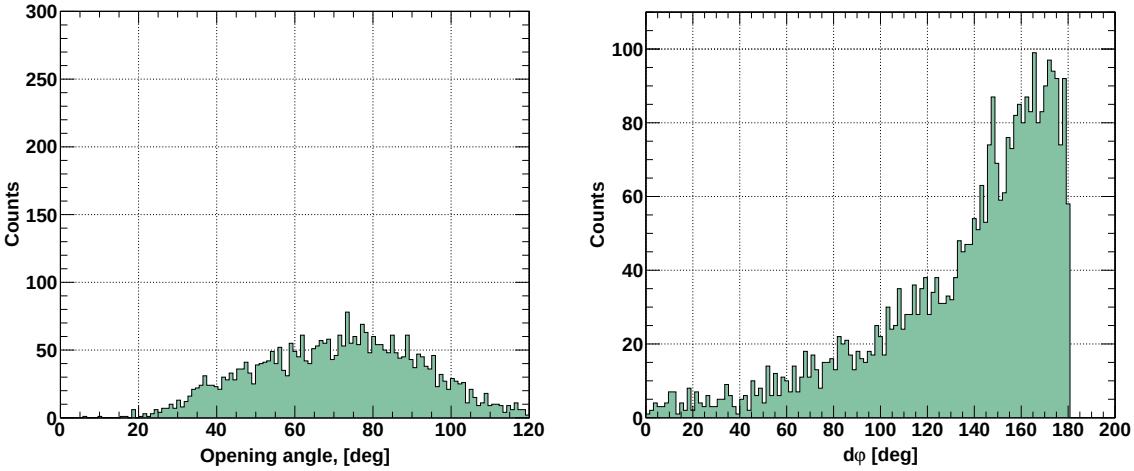

(c) Carbon target (d) Carbon target

Figure 4.40: Angular distributions of proton-neutron pairs from the $^{12}C(p, pn)^{11}C$ reactions. Figures (a) and (b) present measurements with the CH_2 target and figures (c) and (d) show the measurements with the carbon target.

a hole in the proton p-shell. No attempt has been made so far to reconstruct the residual excitation energy corresponding to a neutron knockout from deeply bound s-shell which leads to unbound ^{11}C in the final state. The invariant-mass analysis of the breakup fragments will be required for this purpose.

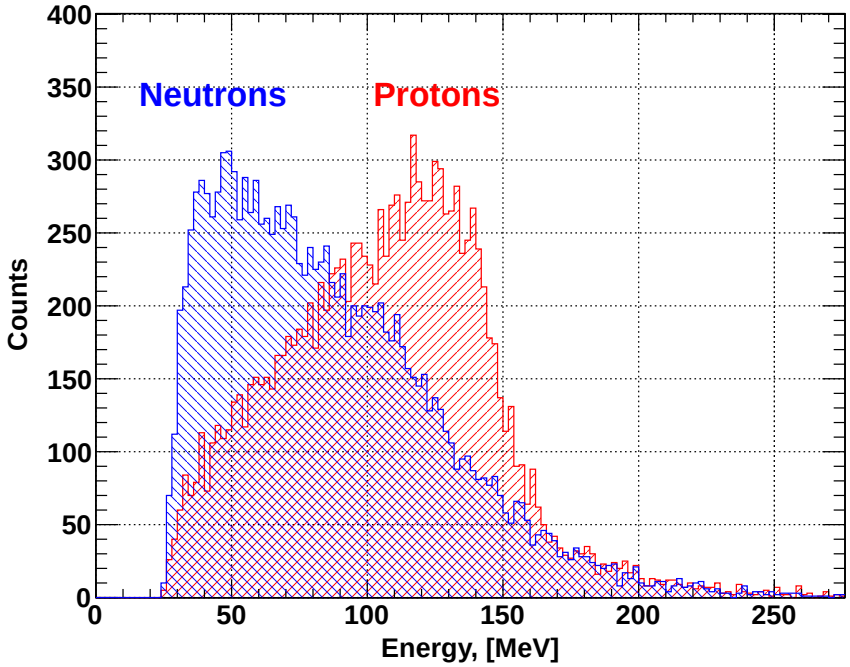

Figure 4.41: Deposited-energy spectra of protons and neutrons in the Crystal Ball from the $^{12}\mathrm{C}(p,pn)^{11}\mathrm{C}$ reactions.

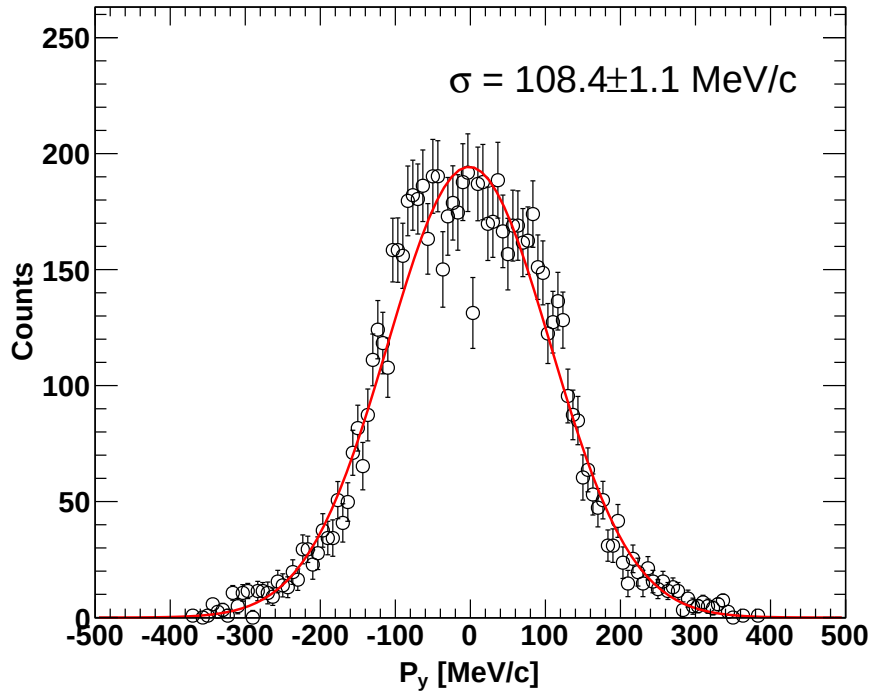

Figure 4.42: Recoil momentum distribution of $^{11}\mathrm{C}$ fragments from the $^{12}\mathrm{C}(p,pn)^{11}\mathrm{C}$ reactions.

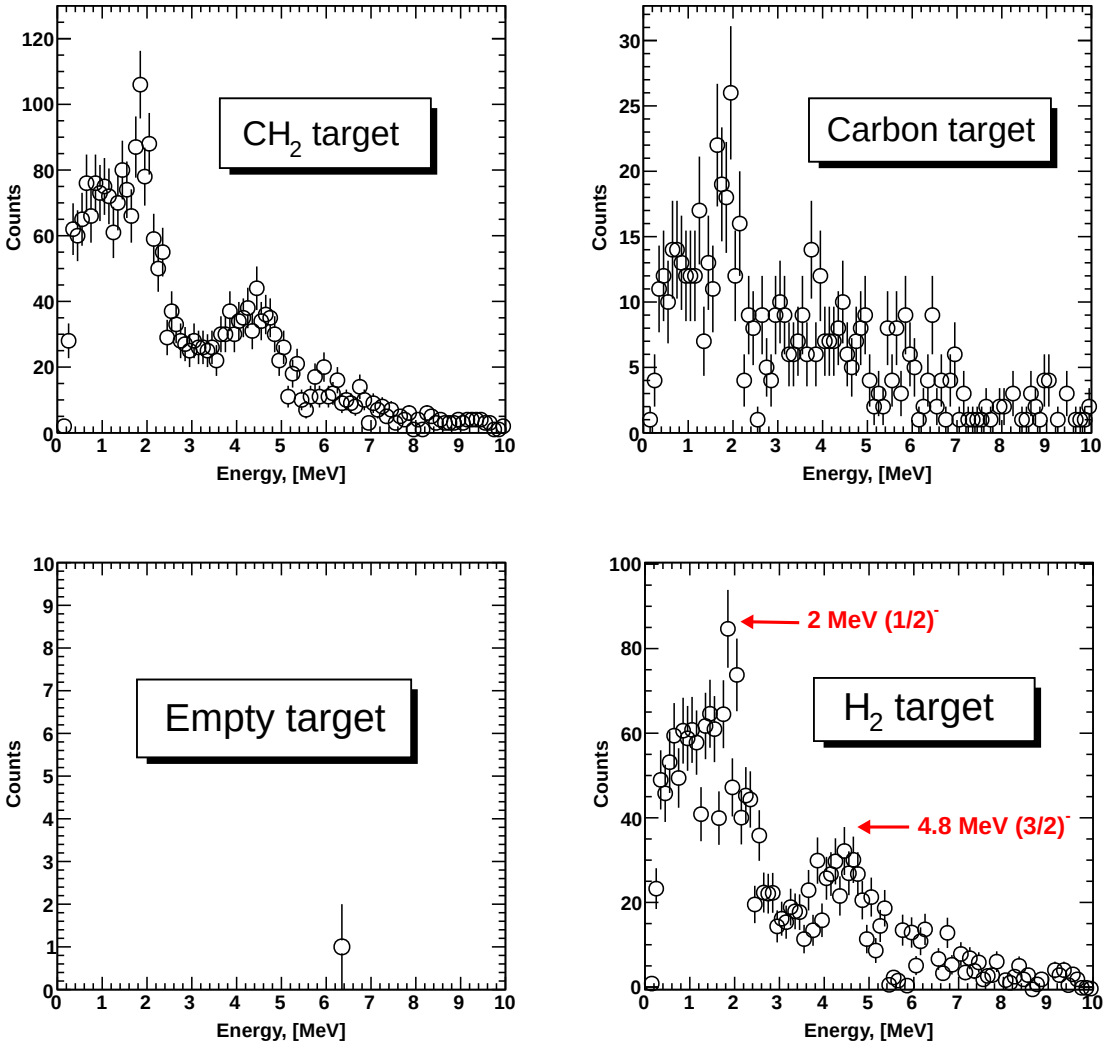

Figure 4.43: Doppler-corrected γ-ray energy spectra in coincidence with outgoing ^{11}C fragment and a proton-neutron pair in the Crystal Ball.

Chapter 5

Discussion of the Results

It has been demonstrated that QFS reactions of a type $(p, 2p)$ and (p, pn) can be studied in inverse kinematics using the CH_2 hydrogen target and an incident ^{12}C beam with an energy of 400 AMeV. It is also the first time when these reactions are measured in complete kinematics with the aid of a large-acceptance detection system. Unfortunately, in the moment of writing this thesis the theoretical calculations are not available, hence the obtained results will be discussed here only qualitatively.

Angular distributions. Despite a rather poor angular resolution of the Crystal Ball, one can observe a correlation between two high-energy hits in the calorimeter (*i.e.* for proton-proton or proton-neutron pairs) even without additional tracking in the box-SSDs. Such kind of measurements can be trusted only if the corresponding final state residue (namely, bound or unbound (A-1) fragment) is properly identified, otherwise the reaction channel is ambiguous due to interference with other QFS processes like (p, pd), $(p, p\alpha)$ etc. The purity of identification can be significantly enhanced if coincident hits are additionally required in the box-SSDs, however, the angular acceptance for the scattered particles is then somewhat reduced. Angular distributions of proton pairs from $^{12}\mathrm{C}(p, 2p)^{11}\mathrm{B}$ reactions are in a very good agreement with the simulated reaction kinematics for a least bound (p-shell) proton in ^{12}C. The width of the measured two-proton opening angle distribution is folded by the contribution from the internal momentum width of a proton and by the experimental angular resolution, which is mainly due to uncertainty of the reaction vertex in the target depth. In the case of proton knockout from the p-shell, these two effects result in nearly equal angular spread. For the $^{12}\mathrm{C}(p, pn)^{11}\mathrm{C}$ reaction, the width of a peak in the proton-neutron opening angle distribution is dominated by the angular resolution for neutrons in the Crystal Ball. It is peculiar that azimuthal distributions of proton-proton and proton-neutron pairs, which are measured with the carbon target, contain also a week correlation pattern indicating coplanar properties of given reactions, although there is no apparent correlation in the corresponding polar angles. Perhaps, one can interpret this as an elastic collision of two nucleons bound nearby the surfaces of the target-nucleus and the projectile-nucleus, that leads to the ejection of both particles from their orbitals.

The interpretation of the angular distributions, corresponding to the knockout from deeply bound states in $^{12}\mathrm{C}(p, 2p)^{11}\mathrm{B}$ reactions, is rather difficult. In principle, the observed peak in the corresponding opening angle distribution is broader and appears at slightly lower value compared to the p-shell knockout, just as expected for strongly bound protons. However, the long tail at smaller angles in this distribution cannot be fully attributed to a pure one-

step QFS process. There must be two major effects that give rise to this tail, namely, the high-momentum component of the internal momentum and the distortion of the outgoing protons' trajectories due to re-scattering on the spectator nucleons. The latter effect can also result in an additional energy transfered to the residual system and, as a consequence, lead to the excitation of the (A-1) residue to continuum (unbound) states. The absorption depends strongly on the location of the reaction vertex in the nuclear volume, so that the largest part of the observed correlations comes most probably from the peripheral area of the nucleus. Secondary processes reduce the number of the reactions in which bound ^{11}B is observed as a final state, and increase the reaction yield for unbound states. Unfortunately, in the present analysis it is impossible to disentangle the secondary processes from pure one-step reactions, especially in the case of knockout from the inner s-shell.

Integrated cross sections. A set of cross sections is measured for different reactions of the ^{12}C beam with the CH_2 and carbon targets. The total cross section for the QFS reaction of a type $(p, 2p)$ is found to be 30.5±2.3 mb. One has to keep in mind that this value characterizes only a probability to observe exactly two outgoing protons. This requirement strongly suppresses the probability of interaction with a high-momentum proton originating, for instance, from short-range nucleon correlations in the nucleus. A correlated nucleon with a high energy can be ejected in such reaction, creating an additional signal in the Crystal Ball. Another aspect to stress is that the total cross section can be partially contaminated by (p, pd) reactions, because deutrons and protons cannot be disentangled by merely measuring their energy losses in the box-SSDs. Thus, no interpretation can be given to the total cross section, unless one ensures that the reaction residue is exactly ^{11}B in either bound or unbound state or that there is a third correlated nucleon ejected in the $(p, 2p)$ reaction.

In contrast to this, the cross section of 18.1±2 mb for the p-shell proton knockout is more reliable, since ^{11}B can be unambiguously identified as a final state, and the assumption of the QFS reaction mechanism is strongly supported by observing the corresponding two-proton angular correlations. This cross section is in a good agreement with the value of 16±4 mb obtained by Gooding & Pugh [3].

One can make a simple estimate, assuming ^{12}C as a pure shell-model nucleus. Since there are twice less protons in l=0 orbital than in the l=1 orbital, the s-shell cross section σ_s is also expected to be twice smaller: $\sigma_s \approx 18.1/2 \approx 9$ mb. Comparing it with the experimental cross section of 12.4 mb for the s-shell, one can find that the measurements give larger value by about 3.4 mb (≈30%), which is presumably due to absorption effects in the nuclear medium.

Momentum distributions. Employing a complete kinematics of the ^{12}C$(p, 2p)^{11}$B reaction, the internal momentum of the p-shell protons in ^{12}C can be redundantly determined either via measuring the recoil momentum of ^{11}B or via the scattered protons. In the latter case, it is sufficient to have only the angular information for one proton if the angles and the energy are known for the second proton. Both methods are proven to be consistent with each other and give the same transverse momentum width of about 105 MeV/c that is in agreement with the results of the $(e, e'p)$ experiment [8]. The internal momentum width of neutrons from the p-shell is measured through the ^{12}C$(p, pn)^{11}$C reaction and has a very similar value of approximately 107 MeV/c. The method with the QFS protons is applied to the $(p, 2p)$ knockout from the s-state and the width of 132 MeV/c is extracted, which also agrees with other experimental measurements [39]. This width is about 25% larger compared

to the one for the p-shell protons. Qualitatively, one can understand it as a consequence of the uncertainty principle, since the inner l=0 orbital is more localized in the nucleus then the outer l=1 orbital, however the absorption effect should be considered here as well.

Population of the hole states. Quasi-free knockout of a nucleon from the valence p-shell in ^{12}C results in populating either the ground state or the low-lying excited states of the reaction residue. Such low-lying states have been observed in the γ-ray spectra in coincidence with $^{12}\mathrm{C}(p,2p)^{11}\mathrm{B}$ and $^{12}\mathrm{C}(p,pn)^{11}\mathrm{C}$ reactions. Only the two first excited states can be observed in both cases in the present measurements, hence the total (proton or neutron) p-shell cross section is fully attributed to these two levels and to the ground state. The measured relative populations of the low-lying p-hole states in ^{11}B from the $^{12}\mathrm{C}(p,2p)^{11}\mathrm{B}$ reaction are compared in figure 5.1 with relative spectroscopic factors (SF) obtained in other experiments (the data are taken from [7]). It must be noted, that the results from the compared $(p,2p)$ experiment [65] were obtained in symmetric experimental geometry using a 100 MeV proton beam. This energy is usually considered to be too low for QFS experiments, since the results can be severely affected by the nuclear absorption. The absolute SF values from the $(d,^3He)$ experiment [66] are also somewhat arguable, because the corresponding absolute values are too large and require certain adjustments in the reaction analysis in order to achieve an agreement with a more precise $(e,e'p)$ experiment (see for example [7]).

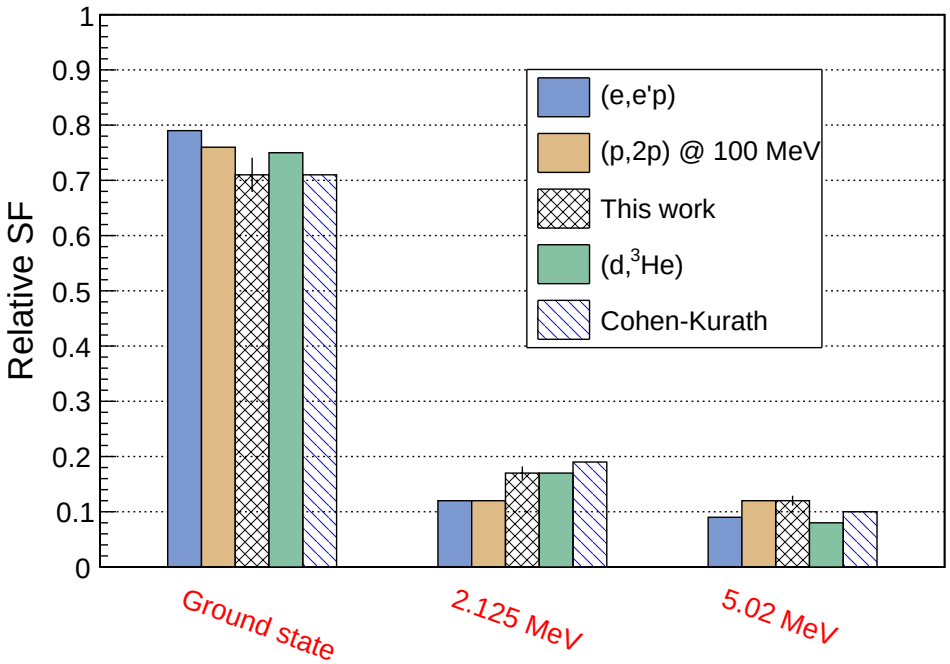

Figure 5.1: Relative populations of three p-hole states in ^{11}B are compared with the relative spectroscopic factors obtained from $(e,e'p)$, $(p,2p)$ and $(d,^3He)$ experiments. A comparison with the theoretical Cohen-Kurath calculations [7] is shown as well. The sum of the relative values for all three states is unity in each case.

There is some discrepancy of the present measurements with the results of the $(e,e'p)$ experiment, which is believed to be the most trustworthy. Namely, somewhat too high relative values are observed for the excited states and too low for the ground state. This can

be partially explained by the absence of the states at higher energies and by the drawbacks in the simulated response of the Crystal Ball, *e.g.* due to the lack of aluminum housing of the crystals. Nevertheless, the obtained relative populations of the p-hole states in ^{11}B show a reasonable agreement (within 10%) with the relative behavior of the spectroscopic factors obtained in other experiments. In order to compare the absolute values, an appropriate reaction theory will be needed. On another hand, there are usually serious difficulties which are faced while trying to deduce the spectroscopic factors involving hadronic reactions due to uncertain reaction mechanism. An alternative approach is to use the relative spectroscopic information because it is usually more reliable as was pointed out by Dickhoff [67].

The excitation energy spectrum, corresponding to the s-hole states in ^{11}B, has a broad peak at around 15 MeV which is about 5 MeV lower than what is usually observed in direct QFS experiments. The main reason for this discrepancy is that the invariant-mass analysis has been performed mostly for two-body breakup channels. Apparently, many-body decays should be observed at higher energies, but the invariant-mass analysis is difficult in this case. Adding together the cross sections from all the measured breakup channels, the value of 6.8$\pm$1 mb is obtained that is about 55% of the total estimated cross section for the unbound final states. The neutron breakup has a largest cross section of 2.08$\pm$0.22 mb, as suggested also by Yosoi *et al.* [37]. It should be noted, that the excited states above a particle separation threshold are not necessarily pure s-hole states as they can be populated also due to the secondary processes in the outgoing channel.

Chapter 6

Conclusions and Future Work

The main objective of this thesis concerns feasibility studies of a new experimental technique for investigating proton-induced quasi-free knockout reactions via fully exclusive measurements in inverse kinematics. A stable beam of ^{12}C has been chosen for this purpose and the obtained data set can serve as a benchmark for the future experiments with radioactive beams at the R^{3}B setup at FAIR (outlined in section 1.5). The usage of the CH_2 reaction target and the incident ^{12}C beam at relativistic energy is proven to be sufficient to initiate nucleon removal from the projectile-like nuclei by the hydrogen component of the CH_2. The measurements involve the use of a 4π-calorimeter (Crystal Ball) and silicon microstrip detectors around the target for measuring the outgoing reaction products, and also detection systems behind a large dipole magnet, which allow for the invariant-mass reconstruction and momentum measurements of the residual fragments. A detailed simulation of the target-recoil detectors has been performed in order to determine their response for protons and γ-rays emerging from the reactions.

A clear evidence of hydrogen-induced QFS reactions of a type $(p, 2p)$ or (p, pn) is indicated in strongly correlated pairs of nucleons emerging from the target. The observed two-proton as well as proton-neutron angular correlations agree very well with kinematical simulations, which predict nearly constant opening angle of about 80° and predominantly coplanar scattering mechanism. Compared to all previous QFS experiments, the present experimental method has an advantage of measuring the scattered nucleons with a large angular acceptance, *i.e.* with minimum restrictions on the kinematics of the QFS process, that is particularly important for the measurements which involve "expensive" radioactive beams with low intensity. Furthermore, the complete kinematics setup allows for redundant reconstruction of the internal nuclear momentum of knocked-out nucleons as has been demonstrated in the case of ^{12}C$(p, 2p)^{11}$B reaction. There are certain disadvantages of using the Crystal Ball calorimeter for the energy measurements of the recoil protons and, especially, neutrons. Such measurements are inappropriate for direct reconstruction of the excitation energy of the residual hole-states, however, these states can be well controlled by measuring coincident γ-rays and invariant-masses of the final state products. The latter technique can be potentially used to study fragmentation mechanism of deep-hole states, which is little known even for stable nuclei. However, this imposes demands on the experimental setup to be capable of precise tracking of several breakup fragments at the same time.

The total cross section of the ^{12}C$(p, 2p)^{11}$B reaction has been measured for the first time and is found to be 30.5±2.3 mb, where the fraction of 18.1±2 mb is associated with a proton knockout from loosely bound $l = 1$ orbital, and 12.4±3 mb is due to knockout

from deeply bound $l = 0$ orbital. Partial cross sections for different final states of ^{11}B have been extracted via γ-ray spectroscopy, in the case of bound states, and via the invariant-mass method for the fragmentation of highly excited deep-hole states. Besides that, the internal momentum distributions of protons removed from the p-shell in ^{12}C are measured redundantly combining two methods: detection of the residual ^{11}B fragment and the angular and energy measurements of the scattered proton pair. The momentum width of 105 MeV/c is extracted for p-state protons using both methods. A similar value of 106 MeV/c is obtained for the internal momentum width of p-state neutrons probed through $^{12}\mathrm{C}(p, pn)^{11}\mathrm{C}$ reaction. The momentum width of 132 MeV/c is obtained for deeply bound s-shell protons, using the information from recoil proton pairs. The obtained experimental results are compared and found to be consistent with previous experiments.

The analysis of the experimental data reported in this thesis is not yet complete, and further developments will be made in future. In particular, the simulated geometry of the Crystal Ball will require an inclusion of aluminum housing around the crystals, which may have a significant influence on the simulated detector response for γ-rays. On the next step, an accurate test of the results of the simulation for γ-rays as well as for QFS protons has to be carried out. The response function has to be also determined for the $^{12}\mathrm{C}(p, pn)^{11}\mathrm{C}$ reaction in order to give quantitative interpretation to the experimental observations of this reaction channel. In addition to this, the analysis of other QFS processes such as (p, pd), $(p, p\alpha)$ will be attempted in the future.

Appendix A

QFS Simulations

The analysis of future experiments at the FAIR facility will rely on physics simulations, which will aim at understanding of the experimental setup response. Due to a large complexity of the future as well as of the present setup, which include numerous types of detectors, it is important not only to know the efficiencies and response functions of each particular detection system, but also to test and to validate the analysis techniques, which are used to extract the physics information from the experimental data. The present simulations are based on the FairRoot simulation and analysis platform [68], which provides a unified package with generic mechanisms to deal with most commonly used tasks in high-energy physics. It is based upon GEANT and ROOT software packages developed in CERN laboratory in Geneva. The R3Broot package is a part of the FairRoot project. It is dedicated to the future R^3B setup at FIAR as well as to the current LAND-R^3B setup at GSI, and it has been used in the analysis of the present experimental data. There were two main goals of the simulations for the analysis: 1) determination of the response and efficiency of the Crystal Ball with respect to two outgoing protons from $^{12}C(p,2p)^{11}B$ reaction; 2) the response of the detector for γ-rays which are emitted in coincidence with the QFS reactions. The event generators which are used to simulate the protons and γ-rays will be described here.

A.1 The QFS Event Generator

The kinematical code for QFS reactions has been developed by Leonid Chulkov at GSI. It has been partially highlighted in section 4.2.2. The Feynman diagram formalism is used to describe the QFS reaction between a projectile-like nucleus with the four-momentum $\mathbf{P} = (\vec{P}, \omega_p)$ and a target proton $\mathbf{p_0} = (\vec{p_0}, \omega_0)$. The four-momenta of the particles in the final state are $\mathbf{Q} = (\vec{Q}, E_Q)$, $\mathbf{q_0} = (\vec{q_0}, E_0)$ and $\mathbf{q_1} = (\vec{q_1}, E_1)$ for the residual nucleus, the scattered proton and the knocked-out nucleon, respectively. The reaction is then governed by the four-momentum conservation:

$$\mathbf{P} + \mathbf{p_0} = \mathbf{Q} + \mathbf{q_0} + \mathbf{q_1}. \tag{A.1}$$

Using the Feynman diagram technique, the reaction can be represented by two vertices as shown in figure A.1. The momentum and energy conservations are required to be fulfilled in both vertices. Thus, the vertex 1 corresponds to the dissociation reaction $\mathbf{P} \rightarrow \mathbf{Q} + \mathbf{p_e}$, in which the quantity $\mathbf{p_e} = \mathbf{P} - \mathbf{Q} = \mathbf{q_0} + \mathbf{q_1} - \mathbf{p_0}$ is the momentum of an intermediate virtual particle (nucleon or fragment). The vertex 2 describes the elastic scattering process

$\mathbf{p_0} + \mathbf{p_e} \rightarrow \mathbf{q_0} + \mathbf{q_1}$, in which $\mathbf{p_0}$, $\mathbf{q_0}$, and $\mathbf{q_1}$ have their physical masses. For the inverse kinematics case, the target-like proton is in rest ($|\mathbf{p_0}| = 0$) in the laboratory coordinate system.

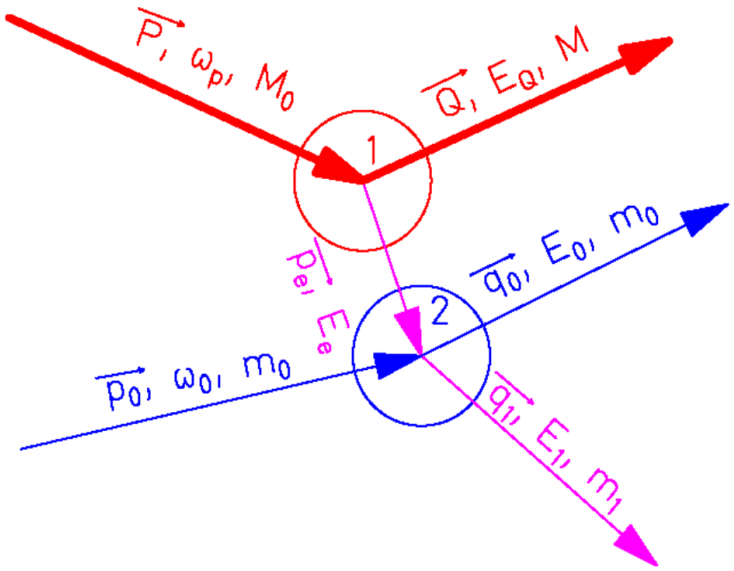

Figure A.1: The Feynman diagram describing a QFS reaction (see notations in text). The figure is taken from [9]

In order to obtain the internal momentum $\vec{p_e}$ of the knocked-out particle, the Goldhaber model can be used [69]. In this model, the internal momentum width σ_g is determined in the following way:

$$\sigma_g^2 = \sigma_0^2 \frac{A_f A_r}{A}, \tag{A.2}$$

where A_f and A_r are the masses of the fragment and residual nucleus, the quantity σ_0 is related to the reaction Q-value: $Q_f = (A_f + A_r - A)$, where A is the mass of the initial system (*i.e.* ^{12}C). In this model one can calculate $\sigma_g \approx 165$ MeV/c for protons bound in ^{12}C assuming $Q_p = 16$ MeV for a least bound proton in the p-shell. This is, however, larger than the experimental value of about 105 MeV/c for the p-shell nucleons, so that the experimental value has been used instead of the calculated σ_g value.

In the vertex 2, the scattering process is chosen to be isotropic, although the real experimental data from the free proton-fragment scattering can be used. Hence, using the experimental beam energy and the intrinsic momentum of the removed nucleon in the projectile, the proton-nucleon scattering kinematics in the laboratory system is calculated. The subscripts of the two outgoing particles are randomized in order to reproduce the experimental measurements, in which the knocked-out and scattered protons cannot be recognized.

The results of the present kinematical simulation for different proton-induced quasi-free scattering reactions (p, pn), (p, pd) and $(p, p\alpha)$ in inverse kinematics with 400 AMeV incident ^{12}C beam are shown in figures A.2, A.3, A.4, A.5, A.6 and A.7.

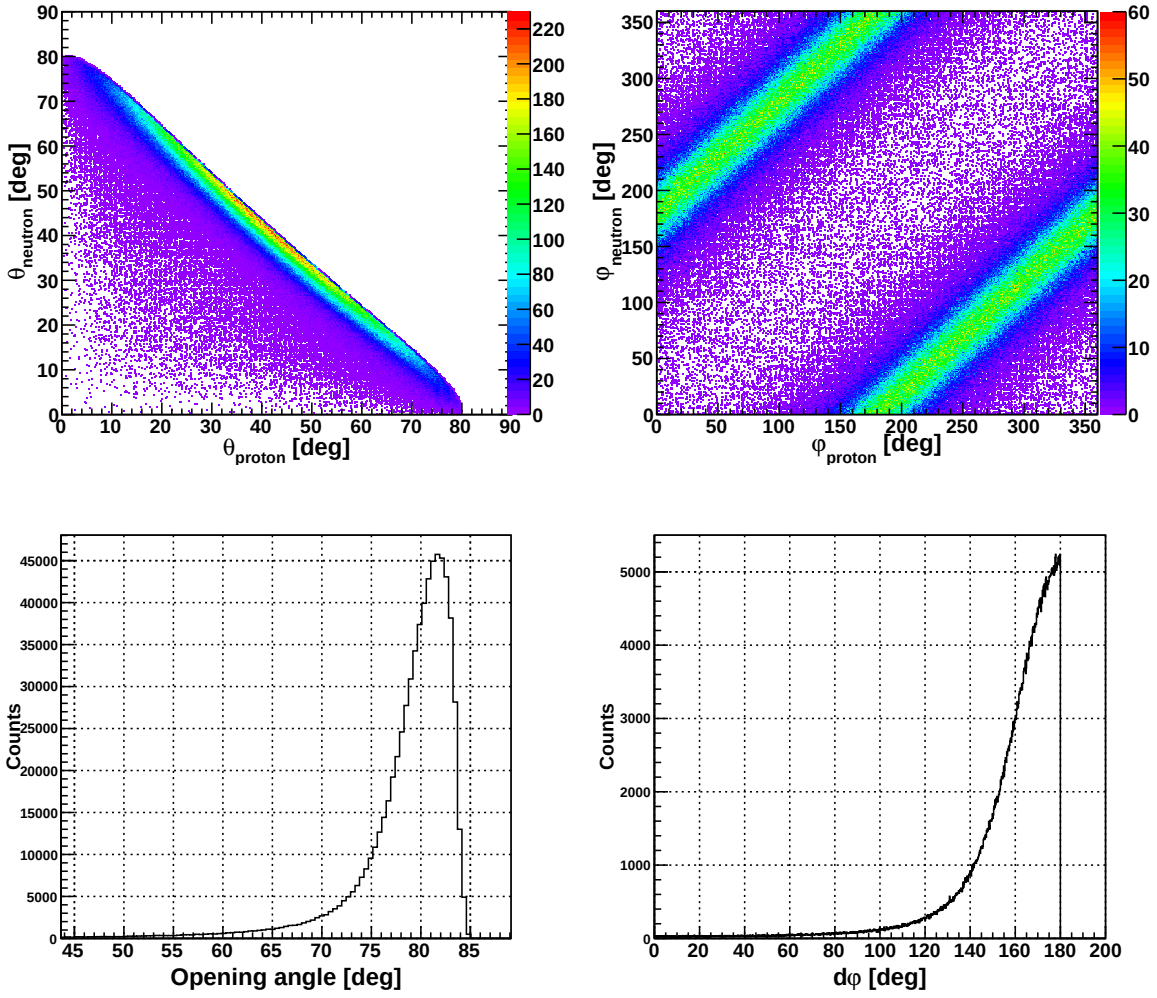

Figure A.2: Kinematical simulation of the ^{12}C$(p,pn)^{11}$C reaction. The Goldhaber sigma of 125 MeV/c is calculated for the internal momentum of neutrons in ^{12}C. The angular distributions are similar to the ones from the ^{12}C$(p,2p)^{11}$B reaction (see figure 4.8).

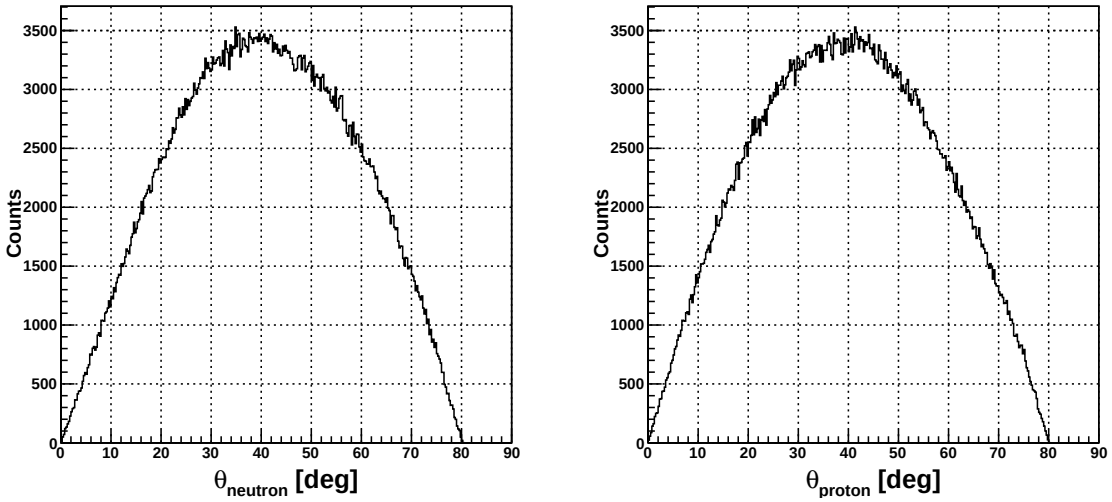

Figure A.3: Distributions of polar angles in ^{12}C$(p,pn)^{11}$ reaction.

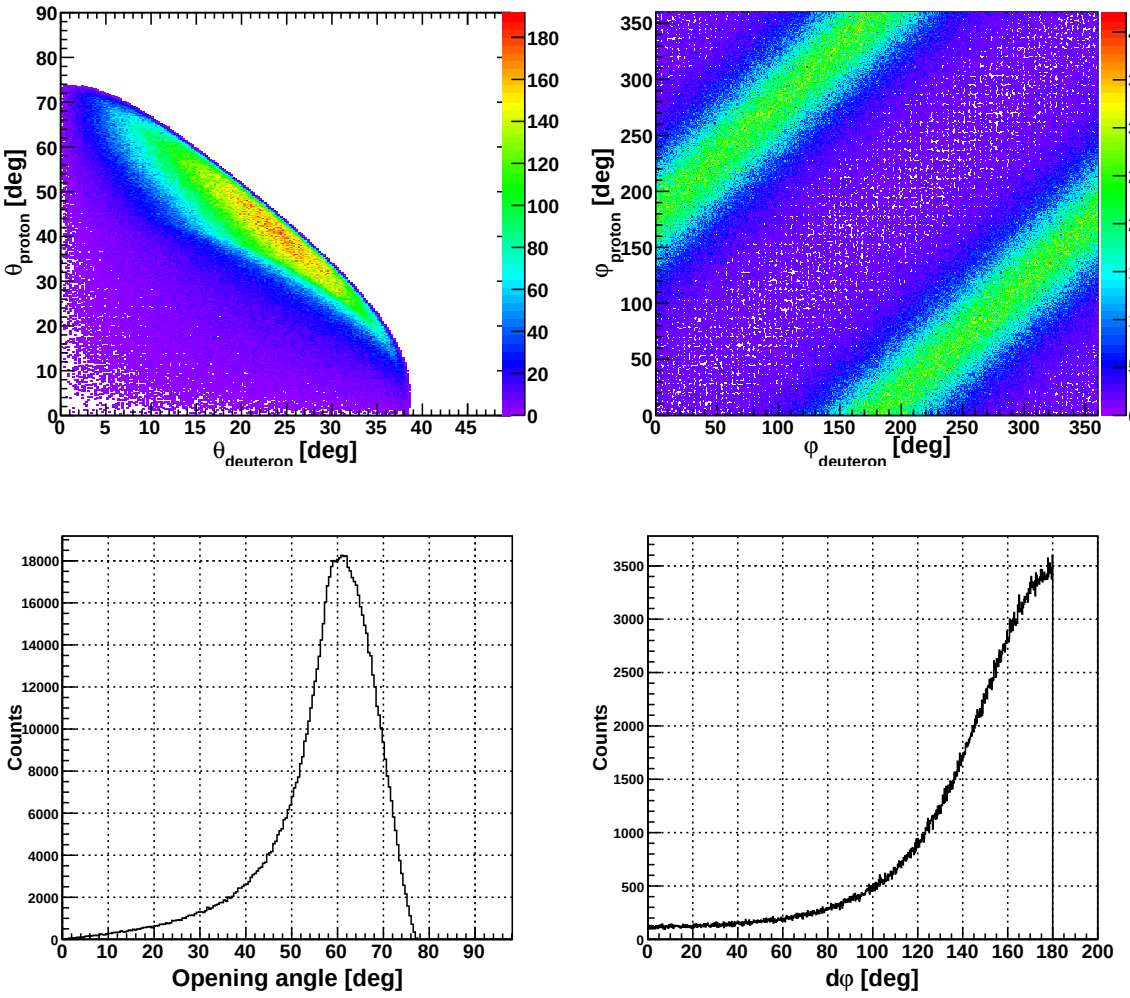

Figure A.4: Kinematical simulation of the ^{12}C$(p,pd)^{10}$B reaction. The Goldhaber sigma of 280 MeV/c is calculated for the internal momentum of deuterons in ^{12}C.

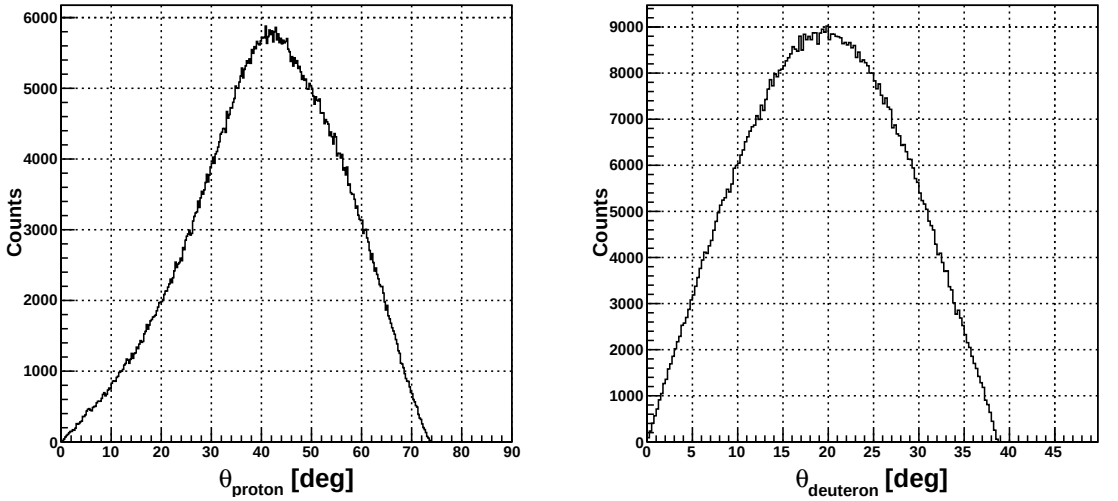

Figure A.5: Distributions of polar angles in ^{12}C$(p,pd)^{10}$B reaction.

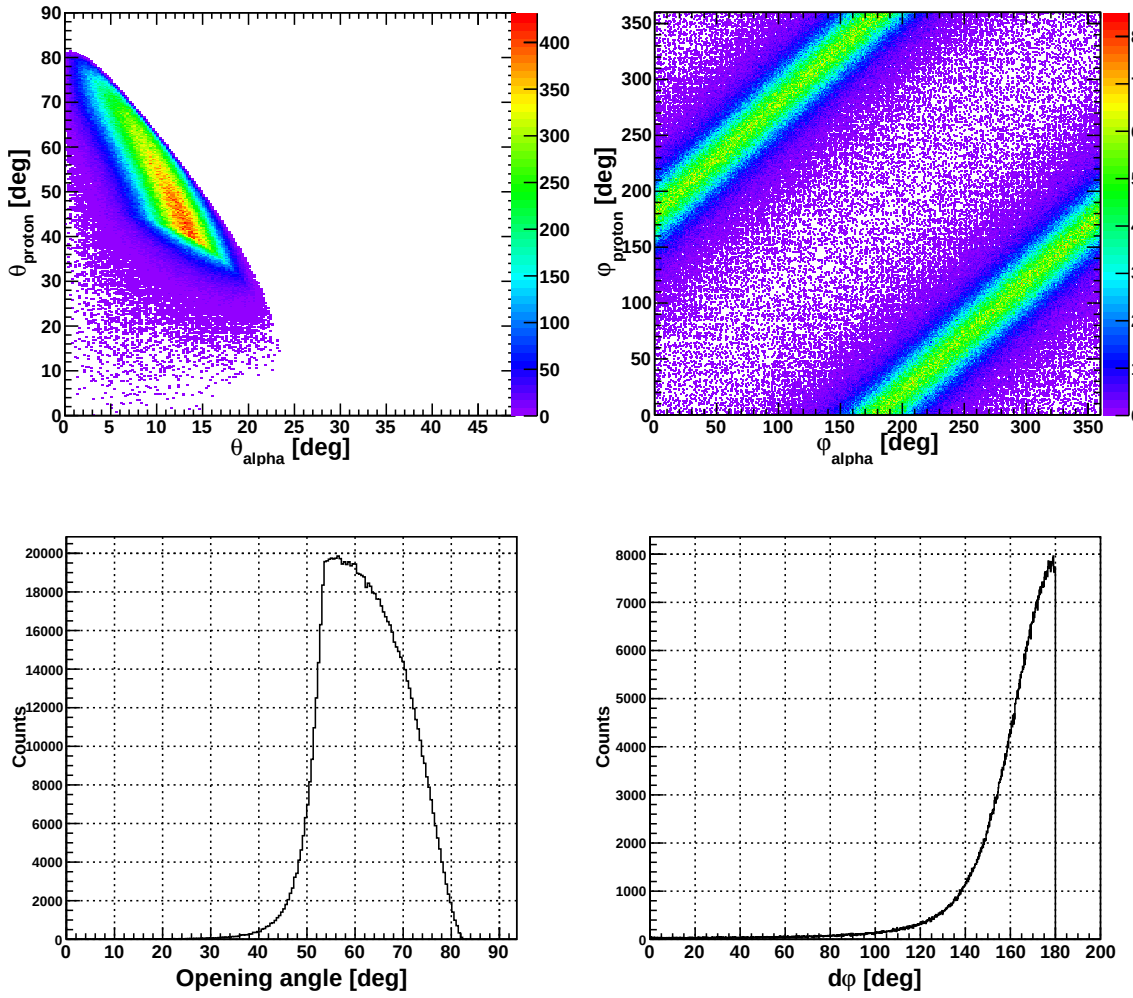

Figure A.6: Kinematical simulation of the ^{12}C$(p, p\alpha)^{8}$Be reaction. The Goldhaber sigma of 191 MeV/c is calculated for the internal momentum of alpha clusters in ^{12}C.

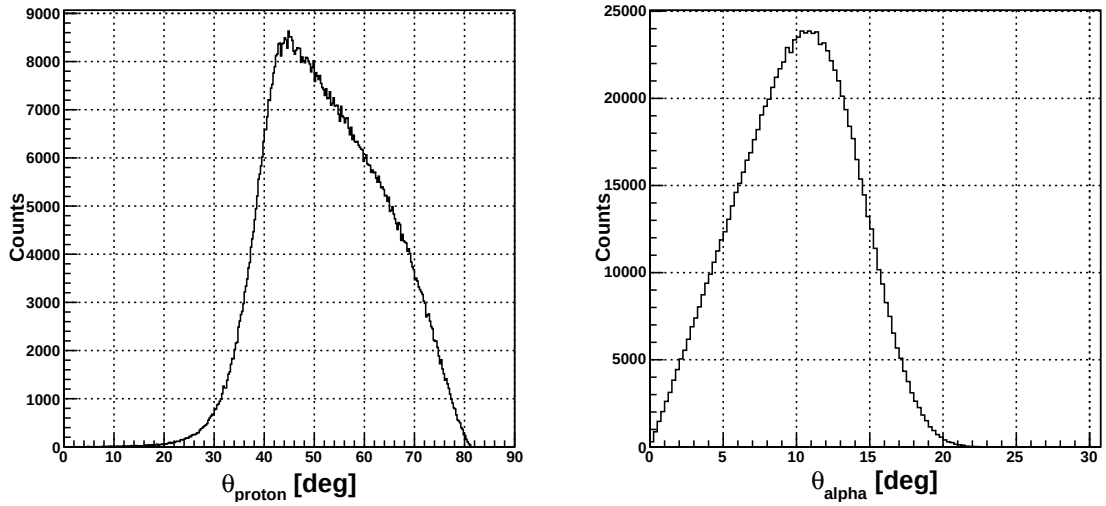

Figure A.7: Distribution of polar angles in ^{12}C$(p, p\alpha)^{8}$Be reaction.

A.2 The event generator for γ-rays

On the next stage, the γ-rays corresponding to decay of excited states of ^{11}B are introduced into simulated ^{12}C$(p, 2p)^{11}$B reactions. It is assumed that the γ-rays are emitted isotropically in the rest frame of the fragment. A uniform angular distribution in a sphere can be achieved using two random numbers F and T which are uniformly distributed in the range from 0 to 1, then the random spherical angles can be calculated as follows:

$$\begin{aligned} \varphi_{rnd} &= 2\pi F, \\ \theta_{rnd} &= acos(2T - 1) \end{aligned} \tag{A.3}$$

The R3Broot event generator requires an input ASCII file, in which Cartesian components of a total momentum of a particle are explicitly given in the lab system. For a single photon with the energy E_0 the individual four-momentum components for a given pair of random angles φ_{rnd} and θ_{rnd} are defined in the rest frame of the emitter as follows:

$$\begin{aligned} P_x &= \tfrac{E_0}{c} sin(\theta_{rnd}) cos(\varphi_{rnd}), \\ P_y &= \tfrac{E_0}{c} sin(\theta_{rnd}) sin(\varphi_{rnd}), \\ P_z &= \tfrac{E_0}{c} cos(\theta_{rnd}), \\ P_t &= \sqrt{P_x^2 + P_y^2 + P_z^2} = \tfrac{E_0}{c}. \end{aligned} \tag{A.4}$$

If γ-rays are emitted by the nucleus which is in rest, the momentum components in the rest frame will directly correspond to the ones in the laboratory system. To account for a Lorentz boost of the γ-rays due to the beam velocity β along Z-axis, the P_z component and the θ_{lab} angle in the laboratory system are transformed as follows:

$$\begin{aligned} P_z &= \tfrac{\gamma E_{cm}}{c} (cos\theta_{rnd} + \beta) \\ \theta_{lab} &= acos\left(\tfrac{P_z}{\sqrt{P_x^2 + P_y^2 + P_z^2}} \right) \end{aligned} \tag{A.5}$$

The energies of γ-rays emitted by a moving projectile with β=0.712 as a function of a polar angle in the laboratory system are shown in figure A.8

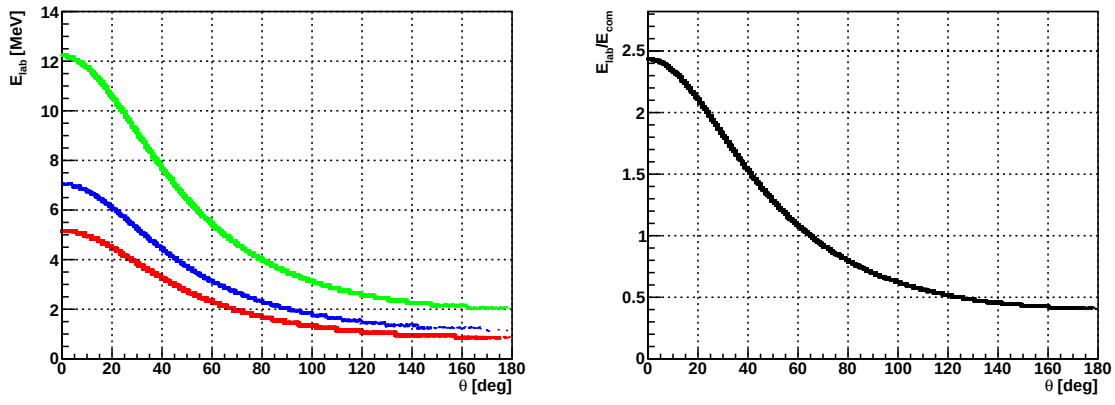

Figure A.8: The energies of γ-rays from the event generator. The left figure shows how the laboratory energy varies for each of the transitions in the cascade from the excited state of ^{11}B at 5.02 MeV. The right figure shows the ratio between the same energies in the laboratory system and in the rest frame of ^{11}B.

Bibliography

[1] O. Chamberlain and E. Segrè, "Proton-Proton Collisions within Lithium Nuclei," *Physical Review*, vol. 87, pp. 81–83, July 1952.

[2] J. B. Cladis, W. N. Hess, and B. J. Moyer, "Nucleon Momentum Distributions in Deuterium and Carbon Inferred from Proton Scattering," *Physical Review*, vol. 87, pp. 425–433, Aug. 1952.

[3] T. Gooding, "Quai-elastic scattering of 153 MeV protons by p-state protons in C12 I. Experimental," *Nuclear Physics*, vol. 18, pp. 46–64, Sept. 1960.

[4] H. Tyrén, "Quasi-free proton-proton scattering in light nuclei at 460 MeV," *Nuclear Physics A*, vol. 79, pp. 321–373, Apr. 1966.

[5] B. Gottschalk and K. Strauch, "Quasi-Elastic Proton-Proton Scattering at 158 Mev," *Physical Review*, vol. 120, pp. 1005–1012, Nov. 1960.

[6] J. C. Roynette, C. Ruhla, M. Arditi, J. C. Jacmart, and M. Riou, "Nouvelle etude des reactions (p, 2p) sur 6 Li et 7 Li a 155 MeV," *Physics Letters*, vol. 19, pp. 497–499, Dec. 1965.

[7] G. van der Steenhoven, H. P. Blok, E. Jans, M. de Jong, L. Lapikás, E. N. M. Quint, and P. K. A. de Witt Huberts, "Knockout of 1p protons from ^{12}C induced by the (e, e'p) reaction," *Nuclear Physics A*, vol. 480, pp. 547–572, Apr. 1988.

[8] J. Mougey, M. Bernheim, A. Bussière, A. Gillebert, X. Phan, Hô, M. Priou, D. Royer, I. Sick, and G. J. Wagner, "Quasi-free (e, e'p) scattering on ^{12}C, ^{28}Si, ^{40}Ca and ^{58}Ni," *Nuclear Physics A*, vol. 262, pp. 461–492, May 1976.

[9] L. V. Chulkov, F. Aksouh, A. Bleile, O. V. Bochkarev, D. Cortina-Gil, A. V. Dobrovolsky, P. Egelhof, H. Geissel, M. Hellström, N. B. Isaev, O. A. Kiselev, B. G. Komkov, M. Matoš, F. N. Moroz, G. Münzenberg, M. Mutterer, V. A. Mylnikov, S. R. Neumaier, V. N. Pribora, D. M. Seliverstov, L. O. Sergeev, A. Shrivastava, K. Sümmerer, S. Y. Torilov, H. Weick, M. Winkler, and V. I. Yatsoura, "Quasi-free scattering with ^{6,8}He beams," *Nuclear Physics A*, vol. 759, pp. 43–63, Sept. 2005.

[10] G. E. Brown and M. Rho, "Scaling effective Lagrangians in a dense medium," *Physical Review Letters*, vol. 66, pp. 2720–2723, May 1991.

[11] R. J. Furnstahl, D. K. Griegel, and T. D. Cohen, "QCD sum rules for nucleons in nuclear matter," *Physical Review C*, vol. 46, pp. 1507–1527, Oct. 1992.

[12] G. Krein, T. A. J. Maris, B. B. Rodrigues, and E. A. Veit, "Medium effects on spin observables of proton knockout reactions," *Physical Review C*, vol. 51, pp. 2646–2655, May 1995.

[13] G. E. Brown, A. Sethi, and N. M. Hintz, "Proton-nucleus scattering and density dependent meson masses in the nucleus," *Physical Review C*, vol. 44, pp. 2653–2662, Dec. 1991.

[14] T. Noro, T. Baba, K. Hatanaka, M. Ito, M. Kawabata, N. Matsuoka, Y. Mizuno, S. Morinobu, M. Nakamura, A. Okihana, K. Sagara, H. Sakaguchi, K. Takahisa, H. Takeda, A. Tamii, K. Tamura, M. Tanaka, S. Toyama, H. Yamazaki, Y. Yuasa, H. Yoshida, and M. Yosoi, "A study of nucleon properties in nuclei through (p,2p) reactions," *Nuclear Physics A*, vol. 629, pp. 324–333, Feb. 1998.

[15] R. Subedi, R. Shneor, P. Monaghan, B. D. Anderson, K. Aniol, J. Annand, J. Arrington, H. Benaoum, F. Benmokhtar, W. Boeglin, J.-P. Chen, S. Choi, E. Cisbani, B. Craver, S. Frullani, F. Garibaldi, S. Gilad, R. Gilman, O. Glamazdin, J.-O. Hansen, D. W. Higinbotham, T. Holmstrom, H. Ibrahim, R. Igarashi, C. W. de Jager, E. Jans, X. Jiang, L. J. Kaufman, A. Kelleher, A. Kolarkar, G. Kumbartzki, J. J. LeRose, R. Lindgren, N. Liyanage, D. J. Margaziotis, P. Markowitz, S. Marrone, M. Mazouz, D. Meekins, R. Michaels, B. Moffit, C. F. Perdrisat, E. Piasetzky, M. Potokar, V. Punjabi, Y. Qiang, J. Reinhold, G. Ron, G. Rosner, A. Saha, B. Sawatzky, A. Shahinyan, S. Širca, K. Slifer, P. Solvignon, V. Sulkosky, G. M. Urciuoli, E. Voutier, J. W. Watson, L. B. Weinstein, B. Wojtsekhowski, S. Wood, X.-C. Zheng, and L. Zhu, "Probing Cold Dense Nuclear Matter," *Science*, vol. 320, pp. 1476–, June 2008.

[16] A. Tang, J. W. Watson, J. Aclander, J. Alster, G. Asryan, Y. Averichev, D. Barton, V. Baturin, N. Bukhtoyarova, A. Carroll, S. Gushue, S. Heppelmann, A. Leksanov, Y. Makdisi, A. Malki, E. Minina, I. Navon, H. Nicholson, A. Ogawa, Y. Panebratsev, E. Piasetzky, A. Schetkovsky, S. Shimanskiy, and D. Zhalov, "n-p Short-Range Correlations from (p,2p+n) Measurements," *Physical Review Letters*, vol. 90, p. 042301, Jan. 2003.

[17] A. Malki, J. Alster, G. Asryan, Y. Averichev, D. Barton, V. Baturin, N. Bukhtoyarova, A. Carroll, S. Heppelmann, T. Kawabata, A. Leksanov, Y. Makdisi, E. Minina, I. Navon, H. Nicholson, A. Ogawa, Y. Panebratsev, E. Piasetzky, A. Schetkovsky, S. Shimanskiy, A. Tang, J. W. Watson, H. Yoshida, and D. Zhalov, "Backward emitted high-energy neutrons in hard reactions of p and π^+ on carbon," *Physical Review C*, vol. 65, p. 015207, Jan. 2002.

[18] J. Aclander, J. Alster, D. Barton, G. Bunce, A. Carroll, N. Christensen, H. Courant, S. Durrant, S. Gushue, S. Heppelmann, E. Kosonovsky, I. Mardor, Y. Mardor, M. Marshak, Y. Makdisi, E. D. Minor, I. Navon, H. Nicholson, E. Piasetzky, T. Roser, J. Russell, M. Sargsian, C. S. Sutton, M. Tanaka, C. White, and J.-Y. Wu, "The large momentum transfer reaction ^{12}C(p,2p+n) as a new method for measuring short range NN correlations in nuclei," *Physics Letters B*, vol. 453, pp. 211–216, May 1999.

[19] C. Ruhla, M. Riou, M. Gusakow, J. C. Jacmart, M. Liu, and L. Valentin, "Etude des reactions Li 6 (p,pd) Et (p, p) Et Be 9 (p,p) A 155 MeV," *Physics Letters*, vol. 6, pp. 282–283, Sept. 1963.

[20] D. W. Devins, B. L. Scott, and H. H. Forster, "A Simple Analysis of the Li^6(p, pd)He^4 Reaction," *Reviews of Modern Physics*, vol. 37, pp. 396–398, July 1965.

[21] T. Yuasa and E. Hourani, "Quasi-Elastic p-α Scattering in C^{12}," *Reviews of Modern Physics*, vol. 37, pp. 399–401, July 1965.

[22] R3B Letter of Intent.

[23] http://www.fair-center.de/index.php.

[24] G. Jacob and T. A. Maris, "Quasi-Free Scattering and Nuclear Structure," *Reviews of Modern Physics*, vol. 38, pp. 121–142, Jan. 1966.

[25] G. Jacob and T. A. Maris, "Quasi-Free Scattering and Nuclear Structure. II.," *Reviews of Modern Physics*, vol. 45, pp. 6–21, Jan. 1973.

[26] T. Berggren and H. Tyren, "Quasi-Free Scattering," *Annual Review of Nuclear and Particle Science*, vol. 16, pp. 153–182, 1966.

[27] A. Bohr, B. R. Mottelson, *Nuclear Structure*, vol. 1. New York: W. A. Benjamin, 1969.

[28] M. G. Mayer, "On Closed Shells in Nuclei," *Physical Review*, vol. 74, pp. 235–239, Aug. 1948.

[29] O. Haxel, J. H. Jensen, and H. E. Suess, "On the "Magic Numbers" in Nuclear Structure," *Physical Review*, vol. 75, pp. 1766–1766, June 1949.

[30] S. Paschalis, *Relativistic One-Nucleon Removal Reactions*. PhD thesis, University of Liverpool, UK, 2008.

[31] I. Tanihata, "TOPICAL REVIEW: Neutron halo nuclei," *Journal of Physics G Nuclear Physics*, vol. 22, pp. 157–198, Feb. 1996.

[32] A. Ozawa, T. Kobayashi, T. Suzuki, K. Yoshida, and I. Tanihata, "New Magic Number, N = 16, near the Neutron Drip Line," *Physical Review Letters*, vol. 84, pp. 5493–5495, June 2000.

[33] P. Adrich, A. Klimkiewicz, M. Fallot, K. Boretzky, T. Aumann, D. Cortina-Gil, U. D. Pramanik, T. W. Elze, H. Emling, H. Geissel, M. Hellström, K. L. Jones, J. V. Kratz, R. Kulessa, Y. Leifels, C. Nociforo, R. Palit, H. Simon, G. Surówka, K. Sümmerer, and W. Waluś, "Evidence for Pygmy and Giant Dipole Resonances in ^{130}Sn and ^{132}Sn," *Physical Review Letters*, vol. 95, p. 132501, Sept. 2005.

[34] P. G. Hansen and J. A. Tostevin, "Direct Reactions with Exotic Nuclei," *Annual Review of Nuclear and Particle Science*, vol. 53, pp. 219–261, Dec. 2003.

[35] A. Gade, P. Adrich, D. Bazin, M. D. Bowen, B. A. Brown, C. M. Campbell, J. M. Cook, T. Glasmacher, P. G. Hansen, K. Hosier, S. McDaniel, D. McGlinchery, A. Obertelli, K. Siwek, L. A. Riley, J. A. Tostevin, and D. Weisshaar, "Reduction of spectroscopic strength: Weakly-bound and strongly-bound single-particle states studied using one-nucleon knockout reactions," *Physical Review C*, vol. 77, p. 044306, Apr. 2008.

[36] A. Gade, D. Bazin, B. A. Brown, C. M. Campbell, J. A. Church, D. C. Dinca, J. Enders, T. Glasmacher, P. G. Hansen, Z. Hu, K. W. Kemper, W. F. Mueller, H. Olliver, B. C. Perry, L. A. Riley, B. T. Roeder, B. M. Sherrill, J. R. Terry, J. A. Tostevin, and K. L. Yurkewicz, "Reduced Occupancy of the Deeply Bound $0d_{5/2}$ Neutron State in ^{32}Ar," *Physical Review Letters*, vol. 93, p. 042501, July 2004.

[37] M. Yosoi, H. Akimune, I. Daito, H. Ejiri, H. Fujimura, M. Fujiwara, T. Ishikawa, M. Itoh, T. Kawabata, M. Nakamura, T. Noro, E. Obayashi, H. Sakaguchi, H. Takeda, T. Taki, A. Tamii, H. Toyokawa, N. Tsukahara, M. Uchida, T. Yamada, and H. P. Yoshida, "Structure and decay of the s-hole state in ^{11}B studied via the ^{12}C(p,2p)^{11}B* reaction," *Physics Letters B*, vol. 551, pp. 255–261, Jan. 2003.

[38] M.Yosoi, *Structures and fragmentations of the deep-hole states in ^{11}B and ^{15}N.* PhD thesis, Kyoto University, Japan, 2003.

[39] T. Kobayashi, K. Ozeki, K. Watanabe, Y. Matsuda, Y. Seki, T. Shinohara, T. Miki, Y. Naoi, H. Otsu, S. Ishimoto, S. Suzuki, Y. Takahashi, and E. Takada, "(p,2p) Reactions on $^{9-16}$C at 250 MeV/A," *Nuclear Physics A*, vol. 805, pp. 431–438, June 2008.

[40] http://gsi.de/beschleuniger/.

[41] J. Alcaraz, B. Alpat, G. Ambrosi, P. Azzarello, R. Battiston, B. Bertucci, J. Bolmont, M. Bourquin, W. J. Burger, M. Capell, F. Cardano, Y. H. Chang, V. Choutko, E. Cortina, N. Dinu, G. Esposito, E. Fiandrini, D. Haas, S. Haino, H. Hakobyan, M. Ionica, R. Ionica, A. Jacholkowska, A. Kounine, V. Koutsenko, G. Lamanna, A. Lebedev, C. Lechanoine-Leluc, C. H. Lin, M. Menichelli, S. Natale, A. Oliva, M. Paniccia, M. Pauluzzi, E. Perrin, M. Pohl, D. Rapin, M. Sapinski, I. Sevilla, W. Wallraff, P. Zuccon, and C. Zurbach, "The alpha magnetic spectrometer silicon tracker: Performance results with protons and helium nuclei," *Nuclear Instruments and Methods in Physics Research A*, vol. 593, pp. 376–398, Aug. 2008.

[42] http://ams-02project.jsc.nasa.gov/.

[43] K. Suemerer *et al.*, "Integrated infrastructure initiative for european nuclear structure research (eurons), joint research activity jra09: Reactions with high-intensity beams of exotic nuclei, task t-j09-2: High-resolution tracking silicon detectors." http://www-win.gsi.de/r3b/RHIB_documents.htm.

[44] F. Wamers, *Quasi-Free-Scattering and One-Proton-Removal Reactions with the Proton-Dripline Nucleus ^{17}Ne at Relativistic Beam Energies.* PhD thesis, Technischen Universität in Darmstadt, Germany, 2011.

[45] K. Mahata, H. Johansson, S. Paschalis, H. Simon, and T. Aumann, "Position reconstruction in large-area scintillating fibre detectors," *Nuclear Instruments and Methods in Physics Research Section A: Accelerators, Spectrometers, Detectors and Associated Equipment*, vol. 608, no. 2, pp. 331 – 335, 2009.

[46] J. Cub, G. Stengel, A. Grünschlo, K. Boretzky, T. Aumann, W. Dostal, B. Eberlein, T. W. Elze, H. Emling, G. Ickert, J. Holeczek, R. Holzmann, J. V. Kratz, R. Kulessa, Y. Leifels, H. Simon, K. Stelzer, J. Stroth, A. Surowiec, and E. Wajda, "A large-area

scintillating fibre detector for relativistic heavy ions," *Nuclear Instruments and Methods in Physics Research Section A: Accelerators, Spectrometers, Detectors and Associated Equipment*, vol. 402, no. 1, pp. 67 – 74, 1998.

[47] T. Blaich, T. W. Elze, H. Emling, H. Freiesleben, K. Grimm, W. Henning, R. Holzmann, G. Ickert, J. G. Keller, H. Klingler, W. Kneissl, R. König, R. Kulessa, J. V. Kratz, D. Lambrecht, J. S. Lange, Y. Leifels, E. Lubkiewicz, M. Proft, W. Prokopowicz, C. Schütter, R. Schmidt, H. Spies, K. Stelzer, J. Stroth, W. Walus, E. Wajda, H. J. Wollersheim, M. Zinser, and E. Zude, "A large area detector for high-energy neutrons," *Nuclear Instruments and Methods in Physics Research Section A: Accelerators, Spectrometers, Detectors and Associated Equipment*, vol. 314, no. 1, pp. 136 – 154, 1992.

[48] J. Taylor, *Proton Induced Quasi-free Scattering with Inverse Kinematics.* PhD thesis, University of Liverpool, United, 2011.

[49] D. Rossi, *Investigation of the Dipole Response of Nickel Isotopes in the Presence of a High-Frequency Electromagnetic Field.* PhD thesis, Johannes Guttenberg-Universität in Mainz, Germany, 2010.

[50] C. Langer, *Coulomb Dissociation of ^{31}Cl and ^{32}Ar - constraining the rp process.* PhD thesis, Johann Wolfgang Goethe-Universität in Frankfurt am Main, Germany, 2012.

[51] H. T. Johansson, "The daq always runs," Master's thesis, Chalmers University of Technology, Göteborg, Sweden, 2006.

[52] http://www-linux.gsi.de/∼rplag/land02/index.php.

[53] J. Hubele, P. Kreutz, J. C. Adloff, M. Begemann-Blaich, P. Bouissou, G. Imme, I. Iori, G. J. Kunde, S. Leray, V. Lindenstruth, Z. Liu, U. Lynen, R. J. Meijer, U. Milkau, A. Moroni, W. F. J. Müller, C. Ngô, C. A. Ogilvie, J. Pochodzalla, G. Raciti, G. Rudolf, H. Sann, A. Schüttauf, W. Seidel, L. Stuttge, W. Trautmann, and A. Tucholski, "Fragmentation of gold projectiles: From evaporation to total disassembly," *Zeitschrift fur Physik A Hadrons and Nuclei*, vol. 340, pp. 263–270, Sept. 1991.

[54] L. Chulkov. Private communication, 2011.

[55] B. A. Brown, P. G. Hansen, B. M. Sherrill, and J. A. Tostevin, "Absolute spectroscopic factors from nuclear knockout reactions," *Physical Review C*, vol. 65, p. 061601, June 2002.

[56] T. Aumann and A. Kelic-Heil. Private Communication, 2011.

[57] K. Hencken, G. Bertsch, and H. Esbensen, "Breakup reactions of the halo nuclei ^{11}Be and ^{8}B," *Physical Review C*, vol. 54, pp. 3043–3050, Dec. 1996.

[58] "Atima." http://www-linux.gsi.de/∼weick/atima/.

[59] R. B. F. et al, *Table of Isotopes, CD ROM Edition, version 1.0.* Wiley-Interscience, 1996.

[60] G. van der Steenhoven, H. P. Blok, E. Jans, L. Lapikás, E. N. M. Quint, and P. K. A. de Witt Huberts, "Weak transitions in the quasi-elastic reaction ^{12}C(e, e'p)^{11}B," *Nuclear Physics A*, vol. 484, pp. 445–475, July 1988.

[61] H. T. Johansson, Y. Aksyutina, T. Aumann, K. Boretzky, M. J. G. Borge, A. Chatillon, L. V. Chulkov, D. Cortina-Gil, U. Datta Pramanik, H. Emling, C. Forssén, H. O. U. Fynbo, H. Geissel, G. Ickert, B. Jonson, R. Kulessa, C. Langer, M. Lantz, T. Lebleis, K. Mahata, M. Meister, G. Münzenberg, T. Nilsson, G. Nyman, R. Palit, S. Paschalis, W. Prokopowicz, R. Reifarth, A. Richter, K. Riisager, G. Schrieder, N. B. Shulgina, H. Simon, K. Sümmerer, O. Tengblad, H. Weick, and M. V. Zhukov, "Three-body correlations in the decay of ^{10}He and ^{13}Li," *Nuclear Physics A*, vol. 847, pp. 66–88, Dec. 2010.

[62] T. Aumann, "Reactions with fast radioactive beams of neutron-rich nuclei," *European Physical Journal A*, vol. 26, pp. 441–478, Dec. 2005.

[63] T. Baumann, A. Spyrou, and M. Thoennessen, "Nuclear structure experiments along the neutron drip line," *Reports on Progress in Physics*, vol. 75, p. 036301, Mar. 2012.

[64] D. Rossi. Private communication, 2011.

[65] D. W. Devins, D. L. Friesel, W. P. Jones, A. C. Attard, I. D. Svalbe, V. C. Officer, R. S. Henderson, B. M. Spicer, and G. G. Shute, "The ^{12}C(p, 2p)^{11}B reaction at 100 MeV," *Australian Journal of Physics*, vol. 32, p. 323, Sept. 1979.

[66] G. Mairle and G. J. Wagner, "The decrease of ground-state correlations from ^{12}C to ^{14}C," *Nuclear Physics A*, vol. 253, pp. 253–262, Nov. 1975.

[67] W. H. Dickhoff, "Determining and calculating spectroscopic factors from stable nuclei to the drip lines," *Journal of Physics G Nuclear Physics*, vol. 37, p. 064007, June 2010.

[68] "Fairroot." http://fairroot.gsi.de/.

[69] A. S. Goldhaber, "Statistical models of fragmentation processes," *Physics Letters B*, vol. 53, pp. 306–308, Dec. 1974.

Acknowledgements

In the following few paragraphs I would like to express my deepest gratitude to the people who guided and helped me throughout the time of writing.

Above all, I want to thank my principal supervisor Prof. Dr. Thomas Aumann who gave me the opportunity to make this research and to participate in the exciting experimental program of the LAND-R^{3}B group. I'm thankful for his guidance and invaluable help in all aspects, and also for encouraging by his brilliant ideas when it was really needed. I wish to thank very much Prof. Dr. Frank Maas and Prof. Dr. Joachim Enders who undertook to act as my supervisors despite their many other professional commitments. A special thank of mine goes to the organizers of the HGS-HIRe program for providing the scholarship and support in many bureaucratic issues and also for very interesting soft-skill courses and power weeks.

This dissertation would not have been possible without contribution of Dr. Jonathan Taylor from Liverpool University, who has spent a good deal of time on the calibrations, analysis, simulations etc. His constructive thoughts and enthusiasm were a constant source of motivation for me throughout almost four years we spent together on this project.

I owe my greatest gratitude to various people who contributed into this work: Dr. Felix Wamers, who developed the add-back algorithm and calibrations for the Crystal Ball and from whom I have learnt many things about the analysis; Dr. Haakan Johansson for making a tremendous work on DAQ and LAND02 software, Dr. Ralf Plag for his help in all kinds of calibrations and tracking; Dr. Dominic Rossi for the calibration scripts and simulations for the LAND detector; Dr. Leonid Chulkov for his QFS kinematical code; Dr. Klaus Suemerer, Dr. Oleg Kiselev, Dr. Branislav Streicher, Dr. Ivan Mukha, and Kristian Larsson for their help with silicon trackers; Dr. Tudi Le Bleis for his exceptional help in programming issues. I'm sincerely thankful to my colleagues and friends: Christoph Caesar, Dr. Stefanos Paschalis, Matthias Holl, Philipp Schrock, Dr. Marina Petri, Dr. Haik Simon, Dr. Heiko Scheit, Dr. Marc Labiche, Dr. Hector Alvarez, Dr. Konstanze Boretzky, Dr. Michael Heil, Dr. Roy Lemmon, Dr. Marielle Chartier, Dr. Rene Reifarth, Dr. Mahata Kripamay, Dr. Aleksandra Kelic-Heil, Dr. Olga Ershova, Dr. Christoph Langer, Dr. Yuliya Aksyutina, Dr. Justyna Marganiec, Alina Movsesyan, Vasily Volkov, Marcel Heine, Ganna Rastrepina, Leyla Atar, and to all people whom I may have forgotten to mention here.

Curriculum Vitae

Name:	Valerii Panin
Date of birth:	30. Juli 1985
Place of birth:	Alchevsk, Ukraine
Citizenship:	Ukrainian
Marital status:	single

Education

1991-2000:	Comprehensive school N.23, Alchevsk.
2000-2002:	Comprehensive school N.15, Alchevsk.

Study of Physics

2002-2006:	Bachelor studies in V.N. Karazin Kharkiv National University, Ukraine.
07/2006	Diploma thesis in Applied Physics: *"Diagnostics of Dermatoses via Kinetic Characteristics of the Induced Chemiluminescence of Blood Serum"* (Grade: very good).
2006-2008	Master studies in V.N. Karazin Kharkiv National University, Ukraine.
03/2008	Diploma thesis in Nuclear Physics: *"Full Strength of the Magnetic Dipole Resonance in* ^{27}*Al"* (Grade: very good).
10/2008-present	PhD student in the Institute for Nuclear Physics, Technical University Darmstadt.

Working experience

03/2008-10/2008	Research engineer in National Science Center Kharkov Institute of Physics and Technology, Ukraine.

Lebenslauf

Name:	Valerii Panin
Geburtsdatum:	30. Juli 1985
Geburtsort:	Alchevsk, Ukraine
Staatsangeh.:	ukrainisch
Familienstand:	ledig

Schulbildung

1991-2000:	Allgemeinbildende Schule N.23, Alchevsk.
2000-2002:	Allgemeinbildende Schule N.15, Alchevsk.

Studium der Physik

2002-2006:	Grundstudium der Angewandten Physik in V.N. Karazin Nationale Universität Charkiw, Ukraine.
07/2006	Bachelor, Titel: *"Diagnose von Hauterkrankungen mittels Kinetischer Eingeschaften von induzierter Chemoluminiszenz in Blutserum"* (Note: sehr gut).
2006-2008	Hauptstudium der Kernphysik in V.N. Karazin Nationale Universität Charkiw, Ukraine.
03/2008	Master, Titel: *"Gesamtstärke der magnetischen Dipolresonanz in* ^{27}Al*"* (Note: sehr gut).
Seit 10/2008	Promotion im Institut für Kernphysik, Technische Universität Darmstadt, Deutschland.

Arbeitserfahrung

03/2008-10/2008	Forschungsingenieur in Nationale Wissenschaftlichzentrum Institut für Physik and Technology, Ukraine.

Eidesstattliche Erklärung

Hiermit erkläre ich, dass ich die vorliegende Dissertation selbständig verfasst, keine anderen als die angegebenen Hilfsmittel verwendet und bisher noch keinen Promotionsversuch unternommen habe.

Darmstadt, im Mai 2012